THE UNIVERSITY OF CHICAGO

DYNAMIC MECHANISMS OF ELECTRONIC-VIBRATIONAL COUPLING IN PHOTOSYNTHETIC PIGMENT-PROTEIN COMPLEXES

A DISSERTATION SUBMITTED TO
THE FACULTY OF THE DIVISION OF THE PHYSICAL SCIENCES
IN CANDIDACY FOR THE DEGREE OF
DOCTOR OF PHILOSOPHY

DEPARTMENT OF CHEMISTRY

BY
JACOB S. HIGGINS

CHICAGO, ILLINOIS
JUNE 2022

to my family, both chosen and biological

There's no such thing as neutral education. Education either functions as an instrument to bring about conformity or freedom.

–Paulo Freire

Thinking is an action. For all aspiring intellectuals, thoughts are the laboratory where one goes to pose questions and find answers, and the place where visions of theory and praxis come together. The heartbeat of critical thinking is the longing to know—to understand how life works. Children are organically predisposed to be critical thinkers. Across the boundaries of race, class, gender, and circumstance, children come into the world of wonder and language consumed with a desire for knowledge. Sometimes they are so eager for knowledge that they become relentless interrogators—demanding to know the who, what, when, where, and why of life. Searching for answers, they learn almost instinctively how to think.

–bell hooks

TABLE OF CONTENTS

LIST OF FIGURES

LIST OF TABLES

ACKNOWLEDGMENTS

My work at the University of Chicago was supported by the National Science Foundation Graduate Research Fellowship. The research presented in this thesis was funded in part by the Department of Energy Office of Science, The Department of Defense under the Vannevar Bush Fellowship, and the Air Force Office of Scientific Research.

There are so many people and communities I've interfaced with during my time in Chicago who I need to give thanks. First, I would like to acknowledge my advisor, Professor Greg Engel, for his support throughout my Ph.D. I appreciate Greg for giving me the freedom and space to pursue my weird, abstract ideas, for stepping up for me when I applied for postdocs and fellowships, and for sharing an obsession for nonadiabatic dynamics. Much of the way Greg structures his group helped me develop into an independent scientist and thinker. I'm grateful to my committee members, Professors Andrei Tokmakoff and Norbert Scherer. I have looked up to both of them as scientists in our department for a long time. I'm thankful for Andrei's teaching, his clear notes on time-dependent quantum mechanics and nonlinear spectroscopy, and for the opportunity to work with him when he chaired the department. He was extremely supportive of graduate students and EDI issues. I'm thankful for the opportunity to teach with and learn from Norbert in multiple classroom settings, both graduate and undergraduate.

I'd also like to acknowledge our collaborators in the Blankenship group at Washington University in St. Louis. Professor Bob Blankenship and Dr. Rafael Saer really shaped our ideas in studying redox dependence and mutants and produced all the samples studied in this thesis. Additional thanks to Professors Bozhi Tian and Jon Simon for supporting me in finding postgraduate positions. And to Neli Fanning, who was a previous director of Equity, Diversity, and Inclusion in the PSD. We worked together a lot over my third and fourth years when I was active in GRIT. I'm thankful to Neli for amplifying our organization, her professional mentorship, our follow up to-do lists, and our shared spirit for student advocacy.

Thank you to all my colleagues in the Engel group who I've worked with over the last six years. To Drs. Sara Sohail, Po-Chieh Ting, John Otto, and Sara Massey for training me in the lab and teaching me what I know about aligning lasers. To Drs. Marco Allodi, Lili Wang, Ryan Wood, and Moira Flanagan for being great resources and for their availability to me as a young graduate student. To Drs. Lawson Lloyd and Elizabeth Bain for being great cohort mates. It's been amazing to see how each of us has developed into grown-up scientists in such different ways. To Dr. Karen Watters, for editing my manuscripts and fellowship applications and for drastically improving my science writing. I would be so vague without Karen. I've had the pleasure of working with a number of undergrad and post-bacc students in my time here: Carlos Olivares, Nick Cleland, Danika Nimlos, James Hayman, Anna Dardia, Chidera Ndife, and Malachi Elue. I'm super proud of these students and have learned from all of them. And thank you to everyone else in the Engel group – Sami Abdulhadi, Caitlin Bellora, Dr. Pete Dahlberg, Indranil Ghosh, Dr. William R. Hollingsworth IV, Coco Li, Dr. Richard Mazuski, Dr. Polina Navotnaya, Dr. Brian Rolczysnki, Qijie Shen, Siddhartha Sohoni, Olivia Wedig, Dr. Nick Williams, Eric Wu, and Dr. Sarah Zinn – for their friendship and for making the group a dynamic place. Thanks to Brenda Thomas, Melinda Moore, and Dr. Vera Dragisich for their constant support and warmth as I navigated through this program. And thank you to folks in other labs who I've looked up to and learned from over the years: Drs. Memo Carpenter, Becca Thompson, Luigi De Marco, Nicole James, Prakriti Joshi, Laura Watkins, and Clara del Junco.

I would not have made it to this point without the student activist organizations at UChicago. I really struggled as a younger graduate student, but in these organizations I found people with overlapping struggles who were motivated to be drivers of change. In Graduate Students United (GSU), I met amazing, politically activated people who dedicated a lot of time toward unionization, mutual aid, political education and awareness, and general organizing. Through my work in the Graduate Recruitment Initiative Team (GRIT), I con-

nected with many scientists from underrepresented backgrounds across the BSD, PSD, and PME. My work in GRIT activated and energized me in a way that I had never experienced before. It is no coincidence that my confidence and creativity as a scientist grew directly alongside my involvement in GRIT. It has been a pivotal source of community and place to center the experiences of marginalized students in STEM.

Finally, I want to thank my friends and family who have been sources of joy and connection in graduate school. First, to my mother, for getting me interested in learning and sparking my curiosity at a young age. As an adult, I am so much like her. To my father, for the unwavering support, and for his home being a place of rest and peace over the years. To my younger brother, Max, for our strong, funny, odd sibling bond, even when we fight about politics. To my dear friend Jess Pontis (Jessica!), for being my workout buddy, for flying kites, and for introducing me to the wild raccoons in Lakeview. To Katie Aracena and Elaine Kouame, my fellow co-directors. I'm thankful that the trauma bonds we made while running GRIT developed into such a wonderful friendship and for our consistent, intentional advocacy for one another. To Marissa Tranquilli, Jeff Dewey, and Saara Azizi, for TV nights, for never getting tired of eating hot pot, and for helping me remember that other people exist from March through May of 2020. To Reed Wagner, for our reconnection in the last year and for being another southern gay with whom to gallivant around Chicago. To Julia Murphy, for our dates where we ate potatoes and commiserated about grad school. To Margo MacDonald and Aria Coraor, for our wholesome lunches. To Meike Lobb-Rabe, for our pandemic walks and discussions about being queer in academia. To Bethany Cartwright and Brandon Cox, for being college friendships that stayed strong over all this time. And to Hyde Park Cats, for connecting me with the wild spirit of Tate Higgins. Our relationship has solidified into a strong one, and she finally stopped attacking me in the night. I could not be more thankful for these connections and the impact they've had on my life in Chicago. I don't know where or who I'd be without them.

ABSTRACT

Photosynthetic pigment-protein complexes can capture and transport solar energy with high efficiency and possess photoprotective mechanisms to prevent excitations from damaging the cell. Over the last decade, mounting evidence has shown mixed electronic-vibrational, or vibronic, states play an important role in photosynthetic energy transfer dynamics. The principles by which photosynthetic complexes engineer the excitonic Hamiltonian can inform how to design energy transport capabilities in modern light harvesting devices. In this thesis, I study how evolution has leveraged vibronic coupling to tune the energy transfer capabilities of the Fenna-Matthews-Olson (FMO) protein complex from green sulfur bacteria. It has been shown that FMO can quench excess excitations in oxidizing redox environments to prevent generation of reactive oxygen species. To understand the influence of the redox environment on the sub-picosecond ($<10^{-12}$ s) energy transfer dynamics, two-dimensional electronic spectroscopy (2DES) is used to study the excited state evolution of wild-type and cysteine deficient FMO complexes in oxidizing and reducing conditions. I develop an analysis method that leverages dynamical symmetries between diagonal and below diagonal cross peaks to deterministically fit to time constants for energy transfer. Two-dimensional spectra are simulated to confirm that the method is accurate for chlorophyll-based excitonic systems. The energy transfer rates between FMO samples show that that the cysteines steer excitations through different pathways in the complex depending on whether the redox conditions are oxidizing or reducing. In oxidizing conditions, excitations are funneled through a pathway to increase the probability of being quenched. Redfield theory modeling shows that the pigment site energies are tuned in oxidizing conditions such that an exciton energy gap falls out of resonant coupling with a pigment vibration. In other words, vibronic coupling is switched on in reducing conditions and off in oxidizing conditions. I further show that many long-lived excited state coherences are only present in reducing conditions when vibronic coupling is present. The coherences correlate with downhill energy transfer, as their magni-

tude is strongest at below diagonal cross peaks. Our spectral analysis reveals that they are mostly vibrational in character and evolve via coherence transfer. The vibrational coherences are maintained through the energy transfer process, which indicates that the vibronically-enhanced energy transfer in reducing conditions is a coherent process. These results are the first to show that a biological system has evolved the ability to modulate an exclusively quantum mechanical effect, vibronic coupling, in response to damaging environmental redox conditions.

CHAPTER 1

INTRODUCTION: TUNING ENERGY DISSIPATION IN PHOTOSYNTHESIS

1.1 Introduction to Light Harvesting

Controlling energy dissipation in excited quantum systems underlies the performance of many chemical and materials technologies today [1, 2, 3]. For example, solar cells and photocatalysts both rely on efficiently funneling excited electronic energy in a well-defined spatial direction. Solar cells must move excitations across large distances with minimal loss where energy can be stored. In molecular photocatalysis, a longstanding challenge has been directing reactive nuclei to desired product wells following photoexcitation. Engineering couplings in these classes of systems is in development [4, 5, 6] but remains difficult in part due to the sheer number of states involved in excited state dynamics. In a typical condensed phase system, there are hundreds, if not thousands, of electronic, vibrational, and rotational states that can couple to the initial electronic excitation where the energy can be deposited. A major goal of this research is to develop tools to understand this complexity and to isolate the degrees of freedom we can tune to control excited state energy dissipation.

In addition to the immense complexity of these system, a further complicating factor is nonadiabatic mixing between electronic and nuclear states. Much of our chemical intuition rests on the Born-Oppenheimer (BO) approximation, first formulated in 1927, one year after Schrödinger's equation [7]. In the BO approximation, we assume that electronic and nuclear motion are separable due to their relative velocities. This assumption simplifies the math in the Schrödinger equation and allows for accurate descriptions of molecular behavior in many circumstances. However, the BO approximation often breaks down in excited electronic dynamics, particularly when resonances between electronic states approach vibrational frequencies. It often breaks down dynamically and transiently, such as when

molecular geometries approach a conical intersection [8]. In these cases of strong nonadiabatic coupling, electronic and nuclear wavefunctions are no longer separable, and they are often represented by mixing the adiabatic states[9]. Nonadiabatic dynamics defy much of our chemical intuition and are difficult to predict and control. They are increasingly believed to dictate a variety of light harvesting systems, including photosynthetic energy transport, rhodopsin proteins, and organic photovoltaics[10, 11, 12]. While mixed electronic-nuclear dynamics complicate the goal of controlling energy dissipation in light harvesting devices, they offer new experimental handles for tuning excited state dynamics.

Despite the challenge of deterministically moving excited state energy through molecular systems, photosynthetic organisms can do so with near unity efficiency across large distances of molecular space[13]. In photosynthesis, pigments absorb solar photons and are promoted to the electronic excited state. Excitons are transported from satellite complexes to the photosynthetic reaction center, where the excited energy is used to drive charge separation across a membrane and initiate biochemical pathways for photosynthesis. Photosynthetic proteins operate in wet, highly disordered environments and use only a few constituent pigments as building blocks of their apparatus. And yet, they can transport excitations robustly and can quench excess excitations when necessary[14]. In this thesis, I describe a novel mechanism by which a photosynthetic complex controls energy flow by tuning nonadiabatic couplings in its constituent pigments. The energy steering mechanism is relatively simple, which begs the question for its commonality across biology. We hope to use the capabilities found here to motivate new designs in technologies such as solar light harvesting devices.

1.2 Concepts and Theories for Photosynthetic Light Harvesting

1.2.1 Pigment-Protein Complexes

As mentioned above, pigment-protein complexes (PPCs) are the basic building blocks for photosynthetic antenna complexes[13]. PPCs are stitched together to form the entire photosynthetic apparatus so that energy can be transported across tens to hundreds of nanometers of space. They are typically comprised of a few pigment molecules such as bacteriochlorophyll-a whose energies are shifted by the local electrostatic environment of the protein scaffold. These are referred to as the site energies. The pigment dipoles are oriented relative to one other to couple the sites and produce a basis of partially delocalized excitonic states. These are referred to as the excitonic energies, and they constitute the eigenbasis of the molecular Hamiltonian. The excitonic landscape is often structured so that downhill energy transfer moves the excitation across the complex. Shown in Figure 1.1 are four excitons in the Fenna-Matthews-Olson (FMO) complex from green sulfur bacteria[15, 16]. Exciton 7, the second highest energy exciton, is partially delocalized over one end of the complex, while the lowest energy exciton 1 is mostly localized onto the pigment nearest to the reaction center. For FMO, excitonic relaxation through this pathway moves the excitation from the 'top' to the 'bottom' of the complex.

1.2.2 Theories for Exciton Energy Transfer

Exciton energy transfer (EET) is the primary mechanism for photosynthetic energy transfer. In EET, an excitation is lost in one state and simultaneously gained in another. This process is mediated by the dipolar interaction between the excitons. Rates for EET are derived from the Liouville-von Neumann equation [17]:

$$\frac{\partial \rho}{\partial t} = -\frac{i}{\hbar}[H, \rho] \tag{1.1}$$

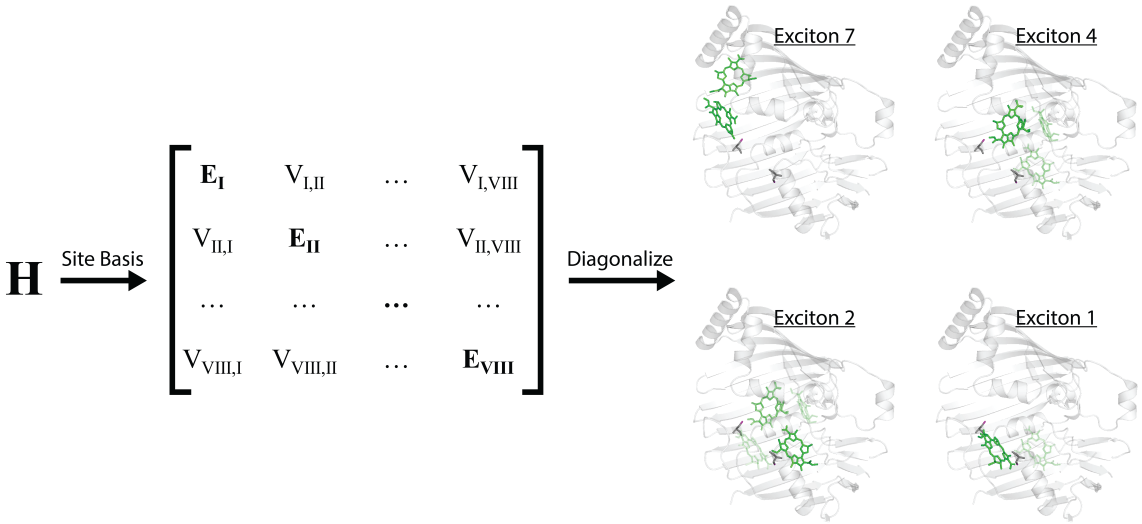

Figure 1.1: Pigment-protein complexes such as the Fenna-Matthews-Olson (FMO) complex from green sulfur bacteria engineer the Hamiltonian such that downhill energy relaxation transports excitonic energy across space. In the site basis of the FMO Hamiltonian, diagonal elements (site energies) are tuned by electrodynamic interactions between the pigments and the protein scaffold, and the off-diagonal dipolar coupling elements are tuned by relative pigment orientations. The Hamiltonian can be diagonalized into the eigenbasis (excitonic energies) to show excitons that are partially localized over different regions of the complex. Here, the excitonic energies are numbered by their relative energies in ascending order. The crystal structure of FMO was first reported in Ref. [15].

where

$$\rho(t) = \sum_k P_k |\psi_k(t)\rangle\langle\psi_k(t)| \tag{1.2}$$

is the density matrix represented in the eigenbasis. Here, the ψ_k terms are the wavefunctions across the ensemble given by probability P_k. These equations are used to derive the quantum master equation, which describes the time evolution of the system components of the density matrix following external perturbation. This approach is shown in detail in Refs. [18, 19].

Photosynthetic energy transfer typically operates within two perturbative limits of the quantum master equation. In the first limit, the coupling between sites is treated perturbatively [18, 20]. The energy transfer rate is derived starting from the dipolar coupling term:

$$V_{ij} = \frac{3(\vec{\mu_i} \cdot \hat{r})(\vec{\mu_j} \cdot \hat{r}) - \vec{\mu_i} \cdot \vec{\mu_j}}{r^3}. \tag{1.3}$$

Here, r is the distance between the dipoles, μ_i is the transition dipole moment of one of the states, and the dot product encodes the angular dependence between the two dipoles. This term is incorporated into Fermi's Golden Rule, which treats the coupling perturbatively to first order:

$$k_{ij} = \frac{2\pi}{\hbar}|V_{ij}|^2 \delta(E_i - E_j). \tag{1.4}$$

Here, k_{ij} is the energy transfer rate between states i and j and the delta function δ enforces a resonance condition between the two states. This treatment yields the following rate constant for EET[20]:

$$k_{ij,FRET} = \frac{4\pi}{3\hbar}\frac{\mu_i^2 \mu_j^2}{r_{ij}^6} J_{ij}(\omega), \tag{1.5}$$

This is the so-called Förster Resonance Energy Transfer (FRET) rate. The efficiency of FRET relies on the distance between the molecules r_{ij}, their relative orientations given by θ, and the overlap integral J_{ij} between the emission of the donor site and the absorption of the acceptor site. FRET is known for its characteristic r^6 character and orientational dependence of transition dipoles.

In the second perturbative limit, we assume that the sites are strongly coupled and that system-bath interactions are treated perturbatively. To second order, we yield the following Redfield rate equation [18, 21]:

$$k_{MN,Redfield} = \pi\omega^2\gamma_{MN}(J(\omega_{MN})(1+n(\omega_{MN})) + J(-\omega_{MN})n(-\omega_{MN})). \tag{1.6}$$

Here, γ_{MN} is the overlap between excitons summed over all sites. In this formulation, we have assumed uncorrelated sites (for more detail, see Ref [21]). The spectral density function $J(\omega)$ describes how strongly bath fluctuations at a particular frequency can couple the excitons. The spectral density is multiplied by the Bose-Einstein distribution

$$n(\omega) = \frac{1}{e^{\hbar\omega/k_BT} - 1} \tag{1.7}$$

to account for the bosonic statistics of bath vibrations, which are temperature and frequency dependent. Depending on the model being used, the spectral density can be represented phenomenologically with a simple function or microscopically with a sum of delta functions or Gaussian curves. The former approach models continuous, low energy bath fluctuations, and the latter models discreet high energy vibrational modes that couple to the system. Some energy transfer models use a hybrid of the two types [22]. My approach uses a log normal spectral density

$$J(\omega) = \frac{S}{\sigma\omega\sqrt{2\pi}} \exp(-\ln(\omega/\omega_c)^2/2\sigma^2) \tag{1.8}$$

with an added vibration. The bath cutoff frequency ω_c and standard deviation σ have been solved for the particular system we studied. The values were taken from Ref. [23]. The Huang-Rhys factor S

$$S = \int_0^\infty J(\omega)\, d\omega \tag{1.9}$$

is a pre-factor for the spectral density. In our modeling, we tune the Huang-Rhys factor to serve as a proxy for the strength of system-bath coupling at a particular frequency. In the Redfield regime, the rate of energy transfer increases when the excitons have a larger wavefunction overlap and when there are more bath vibrations available to resonantly couple the two excitonic states, as modeled by the spectral density.

There are a number of intermediate regimes between the perturbative limits of FRET and Redfield theory. For example, in the modified Redfield theory, the system-bath coupling is split into diagonal and off-diagonal terms, and only the latter is treated perturbatively [18, 24]. In our modeling of energy transfer rates in the Fenna-Matthews-Olson complex, we use the Redfield approach because the sites are strongly coupled and because of the extensive use of Redfield theory to model population transfer in this complex [25, 23, 26]. Furthermore, the system is treated exactly in Redfield theory, so changes to the site energies or couplings can be read out immediately into the energy transfer rate.

1.2.3 Vibronic Coupling

Under an adiabatic view, excitonic states arise by mixing electronic degrees of freedom, and vibrational excitations are appended to the excited state. However, there is increasing evidence that electronic and vibrational states often mix in photosynthetic complexes to

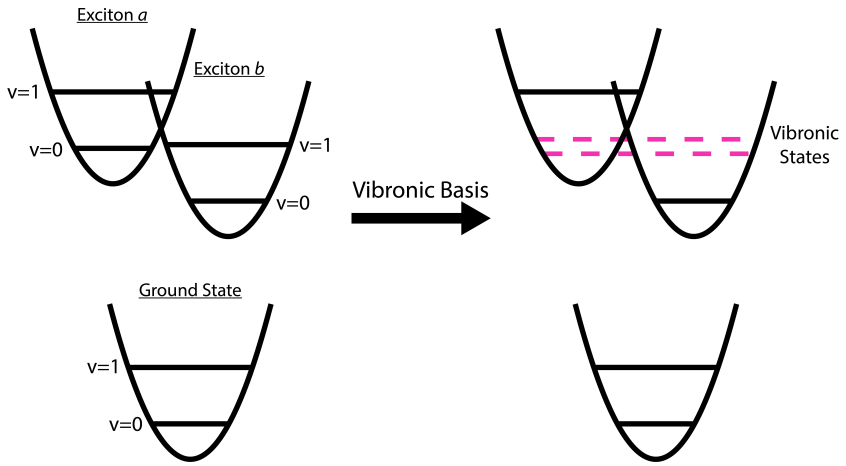

Figure 1.2: Vibronic states arise when states on different excitons with different degrees of vibrational excitation couple. In this case, the v=0 state on the higher energy exciton a couples with the v=1 state on exciton b. This forms a basis containing vibronic states that are weakly delocalized over the two original surfaces [10].

form vibronic states [10, 27, 28]. Vibronic states arise when a state on one excitonic surface couples to a state with a different level of vibrational excitation on another excitonic surface. See, for example, Figure 1.2 where the v=1 state on a lower exciton is resonantly coupled to the v=0 state on a higher exciton.

Vibronic states are straightforward to understand in a linear algebra formalism, as done in Ref. [29]. Here, the vibrations are added to the system Hamiltonian and allowed to couple with resonant excitons, resulting in a vibronic basis with known contribution values from the original sites. Dynamically, vibronic states are more difficult to describe. Vibronic states are inherently nonadiabatic due to the coupling between electronic and nuclear motions [30], so the molecular wavefunctions are no longer separable into electronic and nuclear components. When projected onto the adiabatic basis, the nuclear wavefunctions are delocalized due to coupling between excitonic surfaces with different displacements [31]. Vibronic states can 'borrow' properties from both electronic and nuclear motion. They can have strong transition dipole coupling with the ground state due to intensity borrowing from excitonic states, but can experience slower bath fluctuations from the motion of nuclei [29]. Vibronic coupling

can enhance the energy transfer rate through excitonic systems [32]. In this work, I show how vibronic states can be used as a control parameter in photosynthetic proteins (Chapter 4) and their impact on the microscopic, coherent dynamics of energy transfer (Chapter 5).

1.2.4 Quantum Coherence

Quantum coherence is responsible for the signals generated in nonlinear spectroscopy experiments, including two-dimensional electronic spectroscopy (2DES), covered in the next chapter [10]. In molecular systems, coherences are created by laser excitations that synchronize the phase relationship between superpositions across the ensemble. The fixed-phase relationship of many molecular superpositions creates a macroscopic polarization, whose oscillation generates an electromagnetic field[33]. In our formalism, covered in detail in the next chapter, we treat the electromagnetic radiation classically and the system quantum mechanically. A coherence persists in the system as long as the fixed-phase relationship is maintained across the ensemble. Coherences will decay via decoherence as excited states relax or via dephasing as the fixed-phase relationship is lost across the ensemble due to local environmental fluctuations. Electronic coherences typically decay in less than a hundred femtoseconds, while localized vibrational coherences can decay on the order of a picosecond. I should note that quantum coherence is a different phenomenon than what we call a coherent process. Quantum coherence is related to the fact that the excitation across the ensemble is synchronized. A coherent process is intrinsic to the system. That is, it describes a process that maintains a well-defined phase evolution regardless of the nature of the excitation source. This subtle distinction will be important in Chapter 5, where the preservation of a quantum coherence is indicative of a coherent process.

Quantum coherence is an inherently non-equilibrium effect that arises due to the high degree of coherence in laser sources [10]. While the biological systems we study are not exposed to coherent light sources and may exhibit different behavior in nature[34], we can

still learn much about a system from the dynamics of its coherences. Coherences decay with a characteristic timescale in a given system. The decay is governed by system-bath interactions that drive fluctuations, which are often important components in energy transfer dynamics. For example, the bath fluctuations that cause dephasing can also drive a donor molecule into resonance with an acceptor in a FRET-like energy transfer system [35]. Bath fluctuations can perturb the electronic structure of a donor exciton to increase transient overlap with an acceptor [35, 36]. Some have theorized that non-Markovian bath fluctuations that might prolong dephasing could also enhance energy transfer efficiency in photosynthetic complexes [37]. These studies indicate that coherences can be highly sensitive probes to the complex dynamics underlying energy transfer that would be difficult to observe otherwise. One challenge lies in theoretically linking a coherence signal to a function in the system being probed. Another major challenge is assigning an observed coherence to the correct pair of states in a molecular complex – because all coherences will produce a signal with the same form to a macroscopic observer. The latter difficulty has been the source of intense debate within the photosynthetic light harvesting community and is still largely in question.

1.3 Long-Lived Quantum Coherences and Vibronic Coupling in Photosynthesis

The topics covered in this thesis hopefully add to two strains of research in the field of photosynthetic light harvesting. The first is the assignment of long-lived coherences in pigment-protein complexes and the functional role, if any, they play in energy transfer. The second is to provide further evidence for the role of vibronic states in aiding photosynthetic energy transport. I will briefly review the literature on both of these topics. I and others have reviewed this topic more extensively elsewhere[10, 38].

The assignment and functional role of long-lived coherences in photosynthesis has been a contentious and often confusing debate over the last fifteen years. In 2007, oscillatory wait-

ing time signals lasting for hundreds of femtoseconds were observed in a two-dimensional electronic spectrum of the Fenna-Matthews-Olson complex at 77 K[39]. The beating signals were assigned to interexcitonic coherences (that is, between purely electronic states), which had been generally thought to decay within a hundred femtoseconds. It was proposed that the long-lived electronic coherences were indicative of a 'wavelike' energy transport mechanism, where energy moves through the complex through a series of interexcitonic coherence transfers. In this mechanism, photosynthetic complexes could maximize their energy transfer efficiency because the delocalization averaged out site fluctuations and increased overlap with lower excitons [31]. This picture challenged the 'hopping' mechanism for photosynthetic energy transport that was considered canonical at the time.

Long-lived coherences were soon observed in a number of photosynthetic pigment-protein complexes [40, 41, 42, 43, 44, 45, 46, 47, 48]. One FMO study showed that the coherences persisted at room temperature, with a dephasing time of 300 fs at 277 K[43]. Many began to argue that the long-lived beating signals reported on ground or excited state vibrational coherences because several beating frequencies matched those of known pigment vibrations[49, 30, 50]. The persistence of coherence would be trivial in a ground state vibrational picture, and they would have little implications for the microscopic dynamics of energy transport. Several studies refuted this claim, noting that the Huang-Rhys factors of many photosynthetic pigments such as bacteriochlorophyll-a were small [29], which would reduce the strength of ground state vibrational coherence signals. Experiments using pulse sequences that suppressed vibrational coherence pathways still observed long-lived beats[45, 46], and a study using isotopically modified FMO complexes saw negligible shifts in the observed beating frequencies[44]. These studies supported the electronic assignment of quantum coherence.

Theoretical investigations showed that spatially correlated site fluctuations could explain how coherence lifetimes were prolonged[51, 52, 53, 54]. Typically, bath fluctuations of indi-

vidual sites are assumed to be independent of one another. To preserve electronic coherence, though, the fluctuations must be linked to preserve the phase evolution across the ensemble. Other theoretical studies suggested non-Markovian bath environments[37, 55] and spontaneous recoherence by resonant vibrations [56] to explain the long coherence lifetimes. In each picture, these bath dynamics were thought to enhance energy transfer efficiency and, as a side effect, prolong interexcitonic coherence in spectroscopic experiments. Other studies showed how resonant vibrations generate more usable energy transfer pathways by allowing energy transfer events to occur via larger energy steps[32]. Funneling excess excitonic energy into discrete vibrational modes could promote this non-sequential energy transfer. The authors speculated that one function of prolonged coherence would be to increase the resonant overlap time between excitonic and vibrational states.

About ten years ago, the field began to explore the role of vibronic states in both promoting energy transfer efficiency and in prolonging coherence. Dimer simulations were often used to show how long-lived coherences could arise between vibronic states[57]. One study showed that vibronic coherences could be prolonged if the two states in question were predominantly localized onto the same site[29], that is, if they had a large intrapigment vibrational character. The vibronic state(s) could also 'borrow' transition dipole intensity from the electronic states to amplify their signal strength. Other studies showed that long-lived coherences could be due to ground state vibrations during the waiting time, but whose third-order signal amplitude is increased due to intensity borrowing in vibronic states[30, 50]. In this case, the *dynamics* of coherences are trivial, but their presence is indicative of a complex vibronic structure on the excited state. One study showed that both excited state vibronic and ground state vibrational coherences were stronger because of vibronic mixing between dimers[58]. The role of the three types of coherences (electronic, vibronic, and vibrational) and the fundamental properties that drive them is summarized in Figure 1.3.

Many of these theoretical claims were soon rooted by spectroscopic experiments[59, 60,

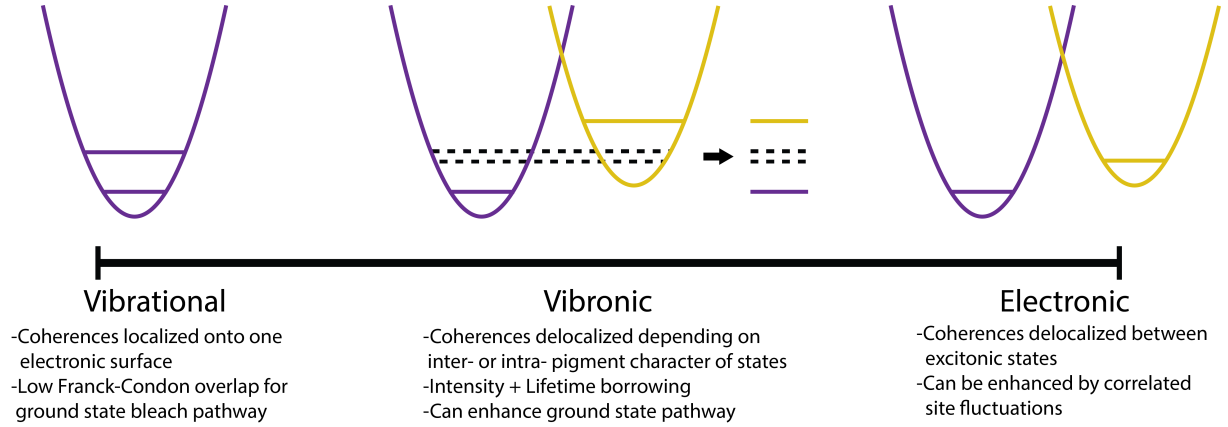

Figure 1.3: Vibronic states span the region between vibrational and electronic states. Coherences can be 'purely' vibrational (between vibrational levels within a single electronic energy state on the excited or ground state) or 'purely' electronic (between electronic levels with the same vibrational excitation on the excited state) as two limiting cases. Coherences can also exist between any set of vibronic states, where electronic and nuclear degrees of eedom nonadiabatically couple to produce a new basis of states, shown to the right of the vibronic diagram. Yellow and purple lines depict states localized onto one electronic surface, and black lines depict vibronic states which can be delocalized between surfaces. Below the diagrams are descriptions of long-lived coherences for each type of state. Figure adapted with permission from Higgins *et al.*, "Quantum Coherence in Chemical and Photobiological Systems," Emerging Trends in Chemical Applications of Lasers (American Chemical Society, 2021), Vol. 1398, Chap. 18 pp. 411-436[10]. Copyright 2021 American Chemical Society.

61, 5]. In recent years, we have seen more direct evidence that vibronic states are involved in photosynthetic energy transport. A study from the Ogilvie group showed that multiple quasi-resonant beats in the two-dimensional electronic spectrum of the purple bacteria reaction center were evidence for non-secular vibronic coherence transfer[28]. The Fleming group used two-dimensional electronic-vibrational spectroscopy to correlate downhill energy transfer in light-harvesting complex II with the growth of excited state vibrational energies, demonstrating that discrete vibrations could be receptacles for excess energy [27]. The work in this thesis shows that vibronic coupling is modulated in the FMO complex to activate an oxidative photoprotective mechanism. At this point, many questions still remain concerning the role of coherence in biology, but further investigations on the dynamical role of vibronic states will hopefully bring clarity to the field.

1.4 Thesis Outline

The data presented in this thesis adds to the growing list of experimental evidence for vibronic states in photosynthesis and shows that long-lived coherences are intimately intertwined with vibronically-enhanced energy transport. In Chapter 2, I will introduce the theory and experimental implementation of two-dimensional electronic spectroscopy. I will describe our GRadient Assisted Photon Echo Spectroscopy setup and discuss improvements made to the spectrometer over the course of my graduate work. In Chapter 3, I will show how we can map the waiting time dynamics in a two-dimensional spectrum using Feynman pathways and use symmetries in the signals to isolate particular energy transfer pathways. In Chapter 4, I use this method to show that FMO can steer populations through different energy transfer pathways depending on the environmental redox condition. I use a Redfield energy transfer model to show that this is accomplished by modulating vibronic coupling in the excitonic states. In Chapter 5, I show that this redox-dependent vibronic coupling has a significant effect on the long-lived quantum coherences in FMO. By correlating the beats with the energy

transfer, we assign the signals to excited state vibrations that undergo downhill coherence transfer without dephasing. I discuss a few future directions regarding redox conditions, the Feynman analysis model, and electronic-vibrational coupling in Chapter 6 before concluding in Chapter 7.

REFERENCES

[1] Andrew H. Proppe, Yuguang C. Li, Alán Aspuru-Guzik, Curtis P. Berlinguette, Christopher J. Chang, Richard Cogdell, Abigail G. Doyle, Johannes Flick, Nathaniel M. Gabor, Rienk van Grondelle, Sharon Hammes-Schiffer, Shaffiq A. Jaffer, Shana O. Kelley, Mario Leclerc, Karl Leo, Thomas E. Mallouk, Prineha Narang, Gabriela S. Schlau-Cohen, Gregory D. Scholes, Aleksandra Vojvodic, Vivian Wing-Wah Yam, Jenny Y. Yang, and Edward H. Sargent. Bioinspiration in light harvesting and catalysis. *Nature Reviews Materials*, 5(11):828–846, 2020.

[2] Hannah J. Sayre, Lei Tian, Minjung Son, Stephanie M. Hart, Xiao Liu, Daniela M. Arias-Rotondo, Barry P. Rand, Gabriela S. Schlau-Cohen, and Gregory D. Scholes. Solar fuels and feedstocks: the quest for renewable black gold. *Energy Environmental Science*, 14(3):1402–1419, 2021.

[3] Michael R. Wasielewski, Malcolm D. E. Forbes, Natia L. Frank, Karol Kowalski, Gregory D. Scholes, Joel Yuen-Zhou, Marc A. Baldo, Danna E. Freedman, Randall H. Goldsmith, Theodore Goodson, Martin L. Kirk, James K. McCusker, Jennifer P. Ogilvie, David A. Shultz, Stefan Stoll, and K. Birgitta Whaley. Exploiting chemistry and molecular systems for quantum information science. *Nature Reviews Chemistry*, 4(9):490–504, 2020.

[4] Stephanie M. Hart, Wei Jia Chen, James L. Banal, William P. Bricker, Amro Dodin, Larysa Markova, Yuliia Vyborna, Adam P. Willard, Robert Häner, Mark Bathe, and Gabriela S. Schlau-Cohen. Engineering couplings for exciton transport using synthetic dna scaffolds. *Chem*, 7(3):752–773, 2021.

[5] Sara H. Sohail, John P. Otto, Paul D. Cunningham, Young C. Kim, Ryan E. Wood, Marco A. Allodi, Jacob S. Higgins, Joseph S. Melinger, and Gregory S. Engel. Dna

scaffold supports long-lived vibronic coherence in an indodicarbocyanine (cy5) dimer. *Chemical Science*, 11(32):8546–8557, 2020.

[6] Richard J. Mazuski, Sebastián A. Díaz, Ryan E. Wood, Lawson T. Lloyd, William P. Klein, Divita Mathur, Joseph S. Melinger, Gregory S. Engel, and Igor L. Medintz. Ultrafast excitation transfer in cy5 dna photonic wires displays dye conjugation and excitation energy dependency. *The Journal of Physical Chemistry Letters*, 11(10):4163–4172, 2020. PMID: 32391695.

[7] M. Born and R. Oppenheimer. Zur quantentheorie der molekeln. *Annalen der Physik*, 389(20):457–484, 1927.

[8] Benjamin G. Levine and Todd J. Martínez. Isomerization through conical intersections. *Annual Review of Physical Chemistry*, 58(1):613–634, 2007.

[9] João Pedro Malhado, Michael J. Bearpark, and James T. Hynes. Non-adiabatic dynamics close to conical intersections and the surface hopping perspective. *Frontiers in Chemistry*, 2(97), 2014.

[10] Jacob S. Higgins, William R. Hollingsworth, Lawson T. Lloyd, and Gregory S. Engel. *Quantum Coherence in Chemical and Photobiological Systems*, volume 1398 of *ACS Symposium Series*, book section 18, pages 411–436. American Chemical Society, 2021.

[11] Oliver P. Ernst, David T. Lodowski, Marcus Elstner, Peter Hegemann, Leonid S. Brown, and Hideki Kandori. Microbial and animal rhodopsins: Structures, functions, and molecular mechanisms. *Chemical Reviews*, 114(1):126–163, 2014. PMID: 24364740.

[12] Markus Kowalewski, Benjamin P. Fingerhut, Konstantin E. Dorfman, Kochise Bennett, and Shaul Mukamel. Simulating coherent multidimensional spectroscopy of nonadiabatic molecular processes: From the infrared to the x-ray regime. *Chemical Reviews*, 117(19):12165–12226, 2017. PMID: 28949133.

[13] Robert E. Blankenship. *Molecular Mechanisms of Photosynthesis*. Wiley/Blackwell, Chichester, West Sussex, 2nd edition, 2014.

[14] Minjung Son, Alberta Pinnola, Samuel C. Gordon, Roberto Bassi, and Gabriela S. Schlau-Cohen. Observation of dissipative chlorophyll-to-carotenoid energy transfer in light-harvesting complex ii in membrane nanodiscs. *Nature Communications*, 11(1):1295, 2020.

[15] Jianzhong Wen, Hao Zhang, Michael L. Gross, and Robert E. Blankenship. Membrane orientation of the fmo antenna protein from lt;emgt;chlorobaculum tepidumlt;/emgt; as determined by mass spectrometry-based footprinting. *Proceedings of the National Academy of Sciences*, 106(15):6134, 2009.

[16] Anton Khmelnitskiy, Adam Kell, Tonu Reinot, Rafael G. Saer, Robert E. Blankenship, and Ryszard Jankowiak. Energy landscape of the intact and destabilized fmo antennas from c. tepidum and the l122q mutant: Low temperature spectroscopy and modeling study. *Biochimica et Biophysica Acta (BBA) - Bioenergetics*, 1859(3):165–173, 2018.

[17] M. Schatz, G.; Ratner. *Quantum Mechanics in Chemistry*, volume 2. Dover, Englewood Cliffs, NJ, 2002.

[18] Mino Yang and Graham Fleming. Influence of phonons on exciton transfer dynamics: comparison of the redfield, förster, and modified redfield equations. *Chemical Physics*, 275:355–372, 2002.

[19] Abraham Nitzan. *Chemical Dynamics in Condensed Phases: Relaxation, Transfer, And Reactions In Condensed Molecular Systems*, volume 1 of *Oxford Graduate Texts*. Oxford University Press, 1st edition, 2014.

[20] Andrei Tokmakoff. *Time-dependent Quantum Mechanics and Spectroscopy, tdqms.uchicago.edu*. 2014.

[21] Thomas Renger and R. A. Marcus. On the relation of protein dynamics and exciton relaxation in pigment–protein complexes: An estimation of the spectral density and a theory for the calculation of optical spectra. *The Journal of Chemical Physics*, 116(22):9997–10019, 2002.

[22] J. M. Womick and A. M. Moran. Vibronic enhancement of exciton sizes and energy transport in photosynthetic complexes. *J Phys Chem B*, 115(6):1347–56, 2011.

[23] Adam Kell, Robert E. Blankenship, and Ryszard Jankowiak. Effect of spectral density shapes on the excitonic structure and dynamics of the fenna–matthews–olson trimer from chlorobaculum tepidum. *The Journal of Physical Chemistry A*, 120(31):6146–6154, 2016.

[24] Wei Min Zhang, Torsten Meier, Vladimir Chernyak, and Shaul Mukamel. Exciton-migration and three-pulse femtosecond optical spectroscopies of photosynthetic antenna complexes. *The Journal of Chemical Physics*, 108(18):7763–7774, 1998.

[25] Adam Kell, Ximao Feng, Mike Reppert, and Ryszard Jankowiak. On the shape of the phonon spectral density in photosynthetic complexes. *The Journal of Physical Chemistry B*, 117(24):7317–7323, 2013.

[26] Adam Kell, Anton Yu. Khmelnitskiy, Tonu Reinot, and Ryszard Jankowiak. On uncorrelated inter-monomer förster energy transfer in fenna–matthews–olson complexes. *Journal of The Royal Society Interface*, 16(151):20180882, 2019.

[27] E. A. Arsenault, Y. Yoneda, M. Iwai, K. K. Niyogi, and G. R. Fleming. Vibronic mixing enables ultrafast energy flow in light-harvesting complex ii. *Nat Commun*, 11(1):1460, 2020.

[28] A.; Willow R.; Laible P.; Bocian D.; Kirmaier C; Holten D.; Mančal T.; Ogilvie J.

Policht, V.; Niedringhaus. Hidden vibronic and excitonic structure and vibronic coherence transfer in the bacterial reaction center. *arXiv*, 2021.

[29] Niklas Christensson, Harald F. Kauffmann, Tõnu Pullerits, and Tomáš Mančal. Origin of long-lived coherences in light-harvesting complexes. *Journal of Physical Chemistry B*, 116(25):7449–7454, 2012.

[30] Vivek Tiwari, William K. Peters, and David M. Jonas. Electronic resonance with anticorrelated pigment vibrations drives photosynthetic energy transfer outside the adiabatic framework. *Proceedings of the National Academy of Sciences*, 110(4):1203, 2013.

[31] Gregory D. Scholes, Graham R. Fleming, Lin X. Chen, Alán Aspuru-Guzik, Andreas Buchleitner, David F. Coker, Gregory S. Engel, Rienk van Grondelle, Akihito Ishizaki, David M. Jonas, Jeff S. Lundeen, James K. McCusker, Shaul Mukamel, Jennifer P. Ogilvie, Alexandra Olaya-Castro, Mark A. Ratner, Frank C. Spano, K. Birgitta Whaley, and Xiaoyang Zhu. Using coherence to enhance function in chemical and biophysical systems. *Nature*, 543(7647):647–656, 2017.

[32] A. Kolli, E. J. O'Reilly, G. D. Scholes, and A. Olaya-Castro. The fundamental role of quantized vibrations in coherent light harvesting by cryptophyte algae. *J Chem Phys*, 137(17):174109, 2012.

[33] Shaul Mukamel. *Principles of Nonlinear Optical Spectroscopy*. Oxford University Press, New York, 1995.

[34] Paul Brumer and Moshe Shapiro. Molecular response in one-photon absorption via natural thermal light vs. pulsed laser excitation. *Proceedings of the National Academy of Sciences*, 109(48):19575–19578, 2012.

[35] M. B. Plenio and S. F. Huelga. Dephasing-assisted transport: quantum networks and biomolecules. *New Journal of Physics*, 10(11), 2008.

[36] F. Caruso, A. W. Chin, A. Datta, S. F. Huelga, and M. B. Plenio. Highly efficient energy excitation transfer in light-harvesting complexes: The fundamental role of noise-assisted transport. *The Journal of Chemical Physics*, 131(10):105106, 2009.

[37] P. Rebentrost and A. Aspuru-Guzik. Communication: Exciton-phonon information flow in the energy transfer process of photosynthetic complexes. *J Chem Phys*, 134(10):101103, 2011.

[38] Lili Wang, Marco A. Allodi, and Gregory S. Engel. Quantum coherences reveal excited-state dynamics in biophysical systems. *Nature Reviews Chemistry*, 3(8):477–490, 2019.

[39] G. S. Engel, T. R. Calhoun, E. L. Read, T. K. Ahn, T. Mancal, Y. C. Cheng, R. E. Blankenship, and G. R. Fleming. Evidence for wavelike energy transfer through quantum coherence in photosynthetic systems. *Nature*, 446(7137):782–6, 2007.

[40] G. Panitchayangkoon, D. V. Voronine, D. Abramavicius, J. R. Caram, N. H. Lewis, S. Mukamel, and G. S. Engel. Direct evidence of quantum transport in photosynthetic light-harvesting complexes. *Proc Natl Acad Sci U S A*, 108(52):20908–12, 2011.

[41] Hohjai Lee, Yuan-Chung Cheng, and Graham R. Fleming. Coherence dynamics in photosynthesis: Protein protection of excitonic coherence. *Science*, 316(5830):1462, 2007.

[42] E. Collini, C. Y. Wong, K. E. Wilk, P. M. Curmi, P. Brumer, and G. D. Scholes. Coherently wired light-harvesting in photosynthetic marine algae at ambient temperature. *Nature*, 463(7281):644–7, 2010.

[43] Gitt Panitchayangkoon, Dugan Hayes, Kelly A. Fransted, Justin R. Caram, Elad Harel, Jianzhong Wen, Robert E. Blankenship, and Gregory S. Engel. Long-lived quantum coherence in photosynthetic complexes at physiological temperature. *Proceedings of the National Academy of Sciences*, 107(29):12766–12770, 2010.

[44] D. Hayes, J. Wen, G. Panitchayangkoon, R. E. Blankenship, and G. S. Engel. Robustness of electronic coherence in the fenna-matthews-olson complex to vibronic and structural modifications. *Faraday Discuss*, 150:459–69; discussion 505–32, 2011.

[45] G. S. Schlau-Cohen, A. Ishizaki, T. R. Calhoun, N. S. Ginsberg, M. Ballottari, R. Bassi, and G. R. Fleming. Elucidation of the timescales and origins of quantum electronic coherence in lhcii. *Nat Chem*, 4(5):389–95, 2012.

[46] S. Westenhoff, D. Palecek, P. Edlund, P. Smith, and D. Zigmantas. Coherent picosecond exciton dynamics in a photosynthetic reaction center. *J Am Chem Soc*, 134(40):16484–7, 2012.

[47] Andrew F. Fidler, Ved P. Singh, Phillip D. Long, Peter D. Dahlberg, and Gregory S. Engel. Dynamic localization of electronic excitation in photosynthetic complexes revealed with chiral two-dimensional spectroscopy. *Nature Communications*, 5(1):3286, 2014.

[48] Richard Hildner, Daan Brinks, Jana B. Nieder, Richard J. Cogdell, and Niek F. van Hulst. Quantum coherent energy transfer over varying pathways in single light-harvesting complexes. *Science*, 340(6139):1448, 2013.

[49] Daniel B. Turner, Krystyna E. Wilk, Paul M. G. Curmi, and Gregory D. Scholes. Comparison of electronic and vibrational coherence measured by two-dimensional electronic spectroscopy. *The Journal of Physical Chemistry Letters*, 2(15):1904–1911, 2011.

[50] M. B. Plenio, J. Almeida, and S. F. Huelga. Origin of long-lived oscillations in 2d-spectra of a quantum vibronic model: electronic versus vibrational coherence. *J Chem Phys*, 139(23):235102, 2013.

[51] Alexandra Olaya-Castro, Chiu Fan Lee, Francesca Fassioli Olsen, and Neil F. Johnson.

Efficiency of energy transfer in a light-harvesting system under quantum coherence. *Phys. Rev. B*, 78:085115, Aug 2008.

[52] Patrick Rebentrost, Masoud Mohseni, and Alán Aspuru-Guzik. Role of quantum coherence and environmental fluctuations in chromophoric energy transport. *The Journal of Physical Chemistry B*, 113(29):9942–9947, 2009. PMID: 19603843.

[53] Francesca Fassioli, Ahsan Nazir, and Alexandra Olaya-Castro. Quantum state tuning of energy transfer in a correlated environment. *The Journal of Physical Chemistry Letters*, 1(14):2139–2143, 2010.

[54] Alexandra Olaya-Castro and Gregory D. Scholes. Energy transfer from förster–dexter theory to quantum coherent light-harvesting. *International Reviews in Physical Chemistry*, 30(1):49–77, 2011.

[55] A. Rivas, S. F. Huelga, and M. B. Plenio. Quantum non-markovianity: characterization, quantification and detection. *Rep Prog Phys*, 77(9):094001, 2014.

[56] A. W. Chin, J. Prior, R. Rosenbach, F. Caycedo-Soler, S. F. Huelga, and M. B. Plenio. The role of non-equilibrium vibrational structures in electronic coherence and recoherence in pigment–protein complexes. *Nature Physics*, 9(2):113–118, 2013.

[57] Felipe Caycedo-Soler, James Lim, Santiago Oviedo-Casado, Niek F. van Hulst, Susana F. Huelga, and Martin B. Plenio. Theory of excitonic delocalization for robust vibronic dynamics in lh2. *The Journal of Physical Chemistry Letters*, 9(12):3446–3453, 2018.

[58] A. Chenu, N. Christensson, H. F. Kauffmann, and T. Mancal. Enhancement of vibronic and ground-state vibrational coherences in 2d spectra of photosynthetic complexes. *Sci Rep*, 3:2029, 2013.

[59] I. S. Ryu, H. Dong, and G. R. Fleming. Role of electronic-vibrational mixing in enhancing vibrational coherences in the ground electronic states of photosynthetic bacterial reaction center. *J Phys Chem B*, 118(5):1381–8, 2014.

[60] David Paleček, Petra Edlund, Sebastian Westenhoff, and Donatas Zigmantas. Quantum coherence as a witness of vibronically hot energy transfer in bacterial reaction center. *Science Advances*, 3(9):e1603141, 2017.

[61] Franklin D. Fuller, Jie Pan, Andrius Gelzinis, Vytautas Butkus, S. Seckin Senlik, Daniel E. Wilcox, Charles F. Yocum, Leonas Valkunas, Darius Abramavicius, and Jennifer P. Ogilvie. Vibronic coherence in oxygenic photosynthesis. *Nature Chemistry*, 6(8):706–711, 2014.

CHAPTER 2

THEORY AND METHODS FOR TWO-DIMENSIONAL ELECTRONIC SPECTROSCOPY

2.1 Overview of 2DES

Two-dimensional electronic spectroscopy (2DES) is a four-wave mixing technique that allows one to track the excited state dynamics of condensed phase systems with femtosecond (10^{-15} s) precision [1, 2, 3, 4, 5, 6]. In 2DES, the sample is illuminated with four temporally compressed laser pulses (Figure 2.1). Three of the pulses interact with the sample, and the fourth pulse pulse (the Local Oscillator, L.O.) is used as a reference to amplify the signal and extract its phase information. We precisely control the time delays and relative geometries of the pulses as they enter the sample stage. The sample in turn generates a signal in the phase matched direction that depends on the time delays, Sig(t_1,t_2,t_3). We process the signal to generate two-dimensional spectra, which contains the dynamical information about the sample such as exciton energy transfer and quantum coherence. The signal is Fourier transformed in the first and third time domains to cast it into the frequency domain: Sig(ω_1,t_2,ω_3). As such, 2DES is a correlation spectroscopy, where a system's excitation frequency ω_1 is correlated with its detection frequency ω_3 as a function of waiting time, t_2 [7]. We study the waiting time evolution to gain information about the system's ultrafast dynamics following transition to the electronic excited state.

The time domain signal emerges from the collective polarization of many molecules in the sample [2]. As such, it is treated as a classical electromagnetic wave. Although the signal is considered classical, its time-dependent modulations and amplitude changes encode the complex quantum dynamics we wish to study. In the next section, I will describe the underlying theory of the four-wave mixing process and interpretation of two-dimensional spectra. Folliwing this description, I will describe the experimental setup, including our

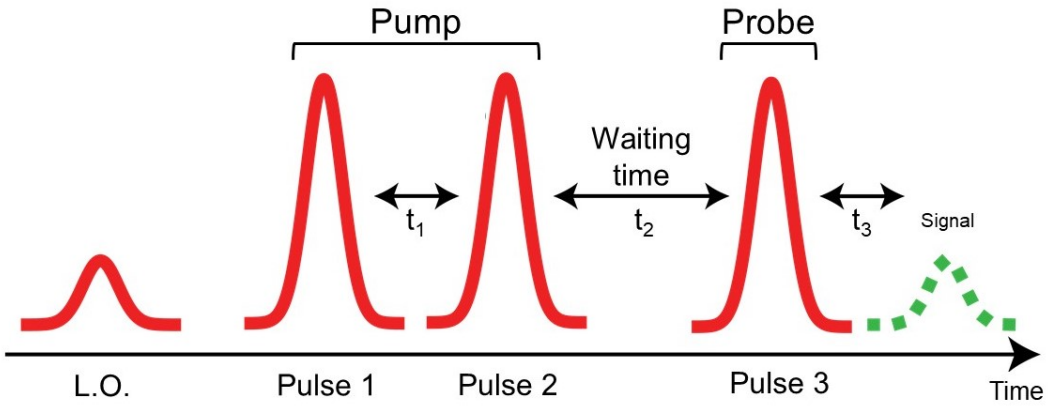

Figure 2.1: Two-Dimensional Electronic Spectroscopy interrogates the sample with four compressed laser pulses. The delay between the first two pulses encodes the coherence time, t_1. These pulses can be considered 'pump' pulses, which excite the system. The delay between pulses 2 and 3 encode the waiting time, t_2. The third pulse 'probes' the system, and a signal is emitted over the detection time, t_3. The fourth pulse is used as a local oscillator (L.O.) reference for heterodyne detection.

specific 2DES apparatus designed in the Engel group. I will describe how data is generated and the necessary data processing steps to extract the signal. I will conclude with changes made to the setup to improve the instrument.

2.2 Theory of 2DES

2.2.1 Polarization and the Density Matrix

In our measurements, the phenomenon that produces the signal is the polarization [2, 3, 8, 9, 10, 11, 12]. The polarization is a macroscopic quantity that describes the sample's nonequilibrium charge distribution after it interacts with the laser pulses. It reflects the fixed-phase behavior of many systems within the ensemble. To describe the polarization in terms of its microscopic constituents, we use the density matrix, ρ.

$$\rho(t) = \sum_k P_k |\psi_k(t)\rangle\langle\psi_k(t)| \tag{2.1}$$

The density matrix describes the statistical ensembles of wavefunctions in the system. The diagonal terms are the populations of each quantum state (and as such, Tr(ρ)=1), and the off-diagonal terms are the coherence terms. The equilibrium density matrix in the eigenbasis will have no coherences because there are no fixed-phase relationships between superposition states in a thermalized ensemble. The populations of the equilibrium density matrix will reflect a Boltzmann-weighted distribution of states.

It is our principle objective to study the time evolution of the density matrix following perturbation by the laser pulses. The equation of motion for the density matrix is given by the Liouville Von Neumann equation[2, 13]

$$\frac{\partial \rho}{\partial t} = -\frac{i}{\hbar}[H, \rho], \tag{2.2}$$

described in the previous chapter. The perturbation falls under the dipole approximation:

$$V = -\mu \cdot E(t). \tag{2.3}$$

Here, $E(t)$ is the external electromagnetic field given by E=E'cos(ωt) with amplitude E' and frequency ω, and μ is the dipole moment operator

$$\mu = \sum_{\alpha} q_{m\alpha}(r_{m\alpha} - R_m), \tag{2.4}$$

which runs over all particles α. The macroscopic polarization is then given by

$$\langle P(t) \rangle = Tr(\mu\rho(t)). \tag{2.5}$$

From time-dependent perturbation theory, the time evolution of the n^{th} order component of the density matrix in the interaction picture is[2]

$$\rho^{(n)}(t) = \left(\frac{i}{\hbar}\right)^n \int_0^\infty dt_n \int_0^\infty dt_{n-1} \ldots \int_0^\infty dt_1 G(t_n) V G(t_{n-1}) V \ldots G(t_1) V \rho(-\infty) \\ \times E(t-t_n) E(t-t_n-t_{n-1}) \ldots E(t-t_n-t_{n-1}-\ldots t_1) \tag{2.6}$$

Here, ρ(-∞) is the equilibrium density matrix, $G(t)$ are the Green's function operators which drive time evolution, and the variables t_n are the time intervals between consecutive pulses. Plugging this term into Equation 2.5, we obtain the third order polarization:

$$P^3(r,t) = \int_0^\infty dt_3 \int_0^\infty dt_2 \int_0^\infty dt_1 \\ \times E(r,t-t_3) E(r,t-t_3-t_2) E(r,t-t_3-t_2-t_1) R^3(t_3,t_2,t_1). \tag{2.7}$$

This equation is a convolution between the classical incident pulses E and the third order response function R^3. The response function is given by[10, 11]

$$R^3(t_3,t_2,t_1) = \left(\frac{i}{\hbar}\right)^3 \langle \mu(t)[\mu(t_3),[\mu(t_2),[\mu(t_1),\rho(-\infty)]]]\rangle, \tag{2.8}$$

where $\langle\ \rangle$ denotes a thermal average over the ensemble. The response function contains several nested commutators composed of the equilibrium density matrix being acted on by dipole operators.

2.2.2 Feynman Pathways to Visualize the Perturbative Response

The third order response function contains many terms who may each evolve differently in any of the time intervals. To visualize these terms in the response function, we employ double-sided Feynman pathways[7, 6, 11, 14]. Several representative Feynman pathways are shown in Figure 2.2. In these pathways, time moves upward, and the diagonal lines represent pulses acting on either side of the density matrix. The first and third time intervals (t_1 and t_3)

evolve as one-quantum coherences. That is, the two states have different degrees of electronic excitation. The second time interval (the waiting time, t_2) can evolve as a population or a coherence depending on the transition induced by the second pulse. The coherences evolve as a zero-quantum coherence - either between excited electronic states, excited or ground state vibrations, or excited vibronic states. The populations evolve based on energy transfer kinetics, which I will expand on in the following chapter.

Overall, there are three classes of Feynman pathways: stimulated emission (SE), excited state absorption (ESA), and ground state bleach (GSB) pathways [11, 14]. These can each be further subdivided into rephasing and nonrephasing pathways. In stimulated emission pathways (Fig. 2.2A,B), the system begins in the excited state during the waiting time, and the third pulse drives the system to a coherence with the ground state. In our notation, these signals are positive because the stimulated emission process generates more photons for the camera. In excited state absorption pathways (Fig. 2.2C,D), the system is in the excited state during t_2, but the third pulse drives absorption to a higher excited state, often a biexciton state depicted in the figure. ESA signals are negative because the higher-lying absorption causes loss of photons. In ground state bleach pathways (Fig. 2.2E,F), the system evolves on the ground state during t_2. The signal is positive because there are fewer molecules in the ground state during t_2 to absorb to the excited state, resulting in more output photons.

In nonrephasing pathways (Fig. 2.2A,C,E), the coherences evolve phase in the same direction over the first and third time domains (both $\exp(-i\ \omega t)$). The signal decays exponentially over t_3 as a free induction decay. In rephasing pathways (Fig. 2.2B,D,F), the states evolve phase in opposite directions over t_1 and t_3 ($\exp(i\ \omega t_1)$ versus $\exp(-i\ \omega t_3)$). Therefore, rather than decaying monotonically over t_3, the signal increases as the oscillators evolve back into relative phase with one other and then decays. This phenomenon is called a photon echo and is the physical reason why rephasing pathways produce stronger signals

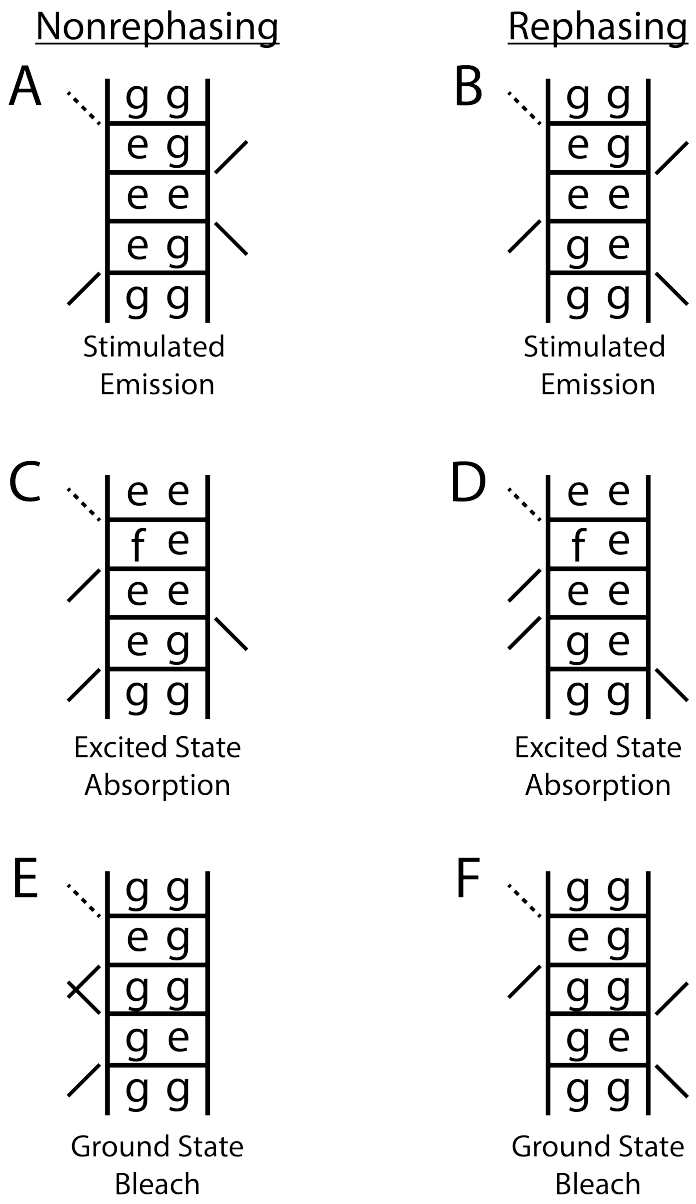

Figure 2.2: Double-sided Feynman pathways map the response of a system following laser excitation. For a given Feynman pathway, time moves upward, and each component of the ladder represents the evolution of a density matrix element in over a time delay. The arrows represent transitions driven by the laser pulses. As such, the bottom rung represents the equilibrium density matrix (all shown as $|\mathrm{g}\rangle\langle\mathrm{g}|$ here), the second rung represents time evolution during t_1, and so on. The signal emitted is shown as a dotted line. Three classes of Feynman pathways, stimulated emission (A,B), excited state absorption (C,D), and ground state bleach (E,F), are shown. These can be further subdivided into nonrephasing (A,C,E) and rephasing (B,D,F) pathways. These pathways are described physically in the text.

than nonrephasing pathways. The Feynman pathways that evolve as populations during t_2 have a symmetrical structure between rephasing and nonrephasing pathways because the order of interactions to generate a population does not matter. This fact is further discussed and exploited in Chapter 3 to isolate population transfer dynamics. By contrast, waiting time coherence pathways have an asymmetrical structure between rephasing and nonrephasing pathways. In the Future Directions, I will discuss how we can use this asymmetry to solve the vibronic structure of spectrally convoluted photosynthetic proteins.

In addition to time ordering and time delays between pulses, the signal is dependent on the spatial orientation of the incident pulses. This reflects the fact that the wavevector component $\exp(i(kr\text{-}\omega t))$ of the pulses is imparted into the third order signal. The signal obeys the phase matching condition

$$k_{sig} = \sum_i k_i, \tag{2.9}$$

which means that signals are produced in directions depending on the geometry of the three pulses. In our setup, we use an inverted boxcar geometry [7]. The signal is generated in a fourth direction with respect to the three pulses (see Ref. [15]), and we overlay the fourth pulse to heterodyne the signal. The inverted boxcar geometry is designed so that the signal is background free and minimizes scatter due to overlap with other pulses. Rephasing and nonrephasing pathways have different phase matching conditions. To image both pathways in the same signal alignment, we simply scan positive and negative time delays between pulses 1 and 2.

2.3 Experimental Implementation of 2DES

The data in this thesis was taken using the GRadient Assisted Photon Echo Spectroscopy (GRAPES) setup developed in the group [15, 16] and based on other two-dimensional spec-

trometer designs [17, 18, 19, 20]. Point-by-point 2DES setups must scan over both coherence (t_1) and waiting time (t_2) delays[4]. GRAPES, however, uses tilted pulses focused to a vertical line rather than a point and encodes the first time delay over a spatial dimension (Figure 2.3). Using a two-dimensional camera, we image all usable t_1 delays over the vertical dimension. The third time delay (t_3) is optically cast into the wavelength domain by a diffraction grating in the camera and does not need to be scanned. We can therefore take an entire two-dimensional spectrum in a single laser shot and only need to scan over the t_2 domain to acquire the full data cube. This process significantly reduces the time necessary to acquire data (to the order of single minutes) and allows one to average multiple iterations of data for better statistics. Tilting the local oscillator to have the same slope as the signal puts the signal into a rotating frame and enables new apodization capabilities to increase the signal to noise ratio, as described in detail previously[21].

In our laser setup, a mode-locked oscillator cavity is used to generate laser light which seeds a regenerative amplifier, generating 800 *nm* pulses with approximately 30 fs width averaging around 2-2.5 W of power. The beam is focused into an argon tube with a pressure of 15-20 psi. Here, the light undergoes filamentation to broaden the bandwidth so that it covers the spectrum of the sample studied. For our experiments of the Fenna-Matthews-Olson complex, the generated light ranged from 780 to 840 *nm*. Following the argon tube, the pulse has significant positive dispersion. We correct for this by first bouncing the beam between pairs of chirped mirrors and then sending the it through our MIIPS pulse shaper (Multiphoton Intrapulse Interference Phase Scan, (Biophotonics))[22]. Here, the pulse is compressed temporally and shaped spectrally to match the needs of the experiment. The pulse is then split, where one arm (composing beams 1 and 2) passes through a delay stage (Aerotech) and chopper where it is chopped every other camera frame. The stage position changes the path length between the arms and generates the waiting time, t_2.

After the delay stage, the pulses enter the GRAPES apparatus, shown in Figure 2.4.

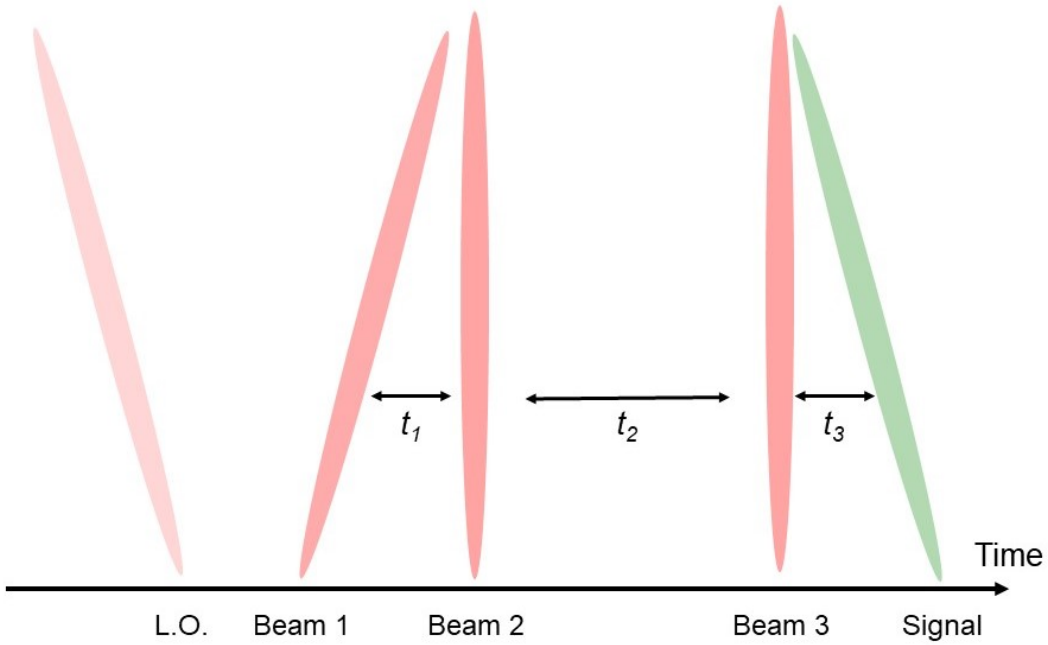

Figure 2.3: The GRadient Assisted Photon Echo Spectroscopy (GRAPES) apparatus uses the same pulse sequence as point-by-point experiments. GRAPES, however, uses tilted pulses to encode the coherence time delay t_1 across the vertical axis of the pulse. Shown here for clarity is the rephasing component of the pulse sequence. The signal is emitted as a photon echo and, as such, peaks when t_1=t_3. The local oscillator (L.O.) is tilted to match the slope of the signal.

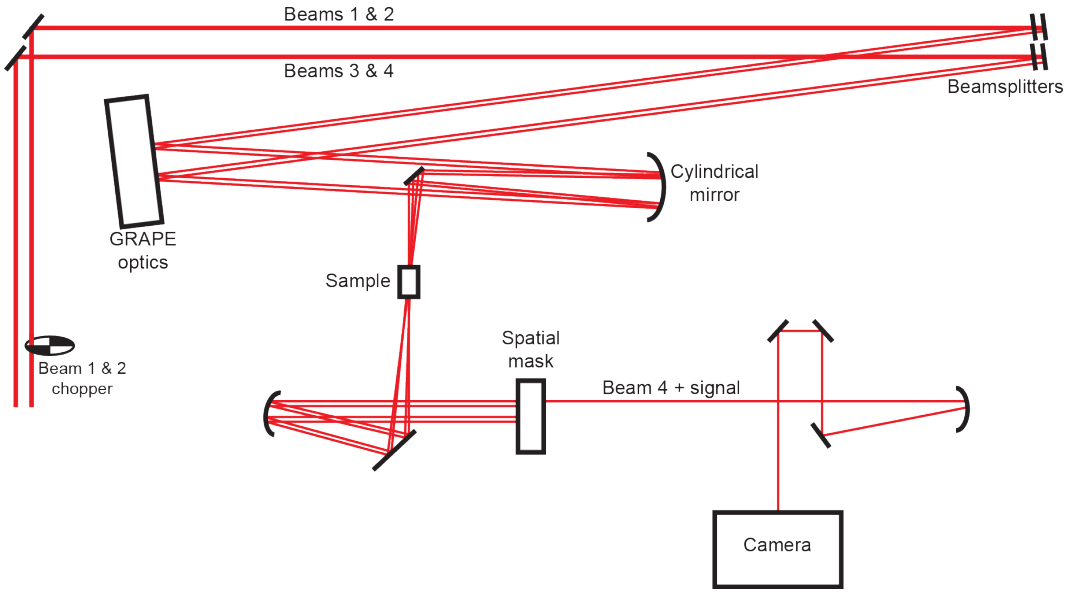

Figure 2.4: Schematic for the GRAPES apparatus, described in the text.

Here, the beams are each split to produce a total of four beams. The beams reflect off of the GRAPES optics, which imparts an upward vertical tilt in the wavevector of beam 1 and a downward vertical tilt of beam 4 (see Ref. [16]). The beams are focused in the horizontal dimension using a cylindrical mirror prior to passing through the sample. All beams except for beam 4 and the signal are then filtered using a spatial mask. The heterodyned signal is then focused onto the camera. The crossing point between beams 1 and 2 are centered on the vertical camera pixels so that above the crossing point, the rephasing signals are imaged, and below the crossing point, the nonrephasing signals are imaged. The coherence time axis is measured interferometrically by measuring the scatter between beams 4 and 1 and between beams 4 and 2. The horizontal camera dimension (λ_3) is interpolated to the frequency domain and Fourier transformed to obtain the time delay between each pulse pair for each row of pixels along the vertical camera axis. The relative slopes between beams 1-4 and beams 2-4 constitute the coherence time delay. In our setup, a typical value for the delay hovers around 0.5 femtoseconds per camera pixel.

The raw data are processed by first subtracting the chopped camera frames from the signal

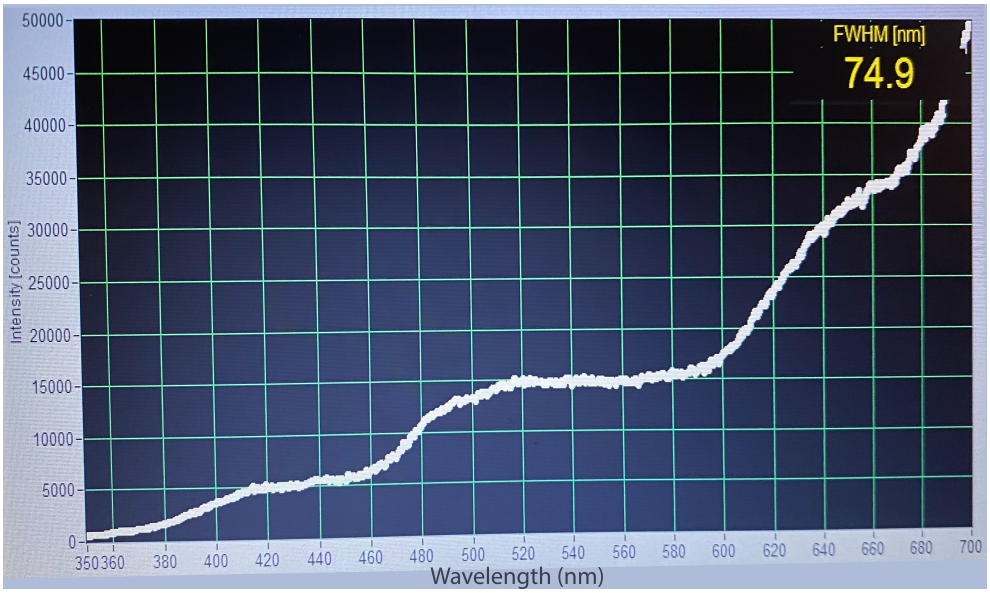

Figure 2.5: White light generated from filamentation through a pressurized tube of argon. The spectrum spans from the fundamental (centered at 800 nm) to approximately 370 nm. The spectrum was measured in June of 2021 with an integration time of 50 ms.

frames to remove scatter. The horizontal camera axis is then interpolated to frequency ω_3 for every coherence time t_1 and waiting time t_2 value. The data cube is Fourier transformed over ω_3 to put the signal fully into the time domain. The nonrephasing half of the data must then be restructured because the waiting time delay changes across the vertical axis of the camera[23]. This procedure is described in detail in Ref. [24]. The signal is then apodized via a low pass filter in the ω_2 domain and a high pass filter in the t_3 domain. This removes the majority of the remaining scatter contributions from the three pulses[21]. The data are then Fourier transformed to the ω_1 and ω_3 frequency domains and the t_2 time domain and phased by applying absolute, linear, and quadratic phase functions to the frequency domains. The values are selected according to the best fit to the pump-probe spectrum via the projection-slice theorem.

2.4 Instrument Improvements

In recent years, two major changes have been made to improve the performance of the instrument. First, the filamentation process was improved for white light generation. Efficient filamentation depends on the pulse power, pulse compression, and the argon pressure. The old compressor grating was replaced to improve the compression of the pulse following amplification. The Pockels cells in the amplifier cavity were replaced because the previous cells were burned and oxidized. The white light generation is extremely sensitive to the Pockels cell alignment and timings. The cavity was realigned from scratch to maximize power and minimize internal reflection from the Pockels cells. The seed input and output timings were scanned over several nanoseconds for optimal white light generation. Finally, the argon pressure was tuned to 22 psi, which is the maximum value that could be obtain without diminishing power stability. The white light generation previously decayed around 500 nm. With these improvements, the setup can regularly generate light down to 400-425 nm and sometimes lower (see Figure 2.5 for a sample spectrum) with pulse power sufficient for 2DES (25-35 mW, cutting off at 700 nm). This performance allows one to study samples that absorb at bluer wavelengths, such as bacteriorhodopsin, which has a large spectral linewidth and peaks at 560 nm [25, 26].

The second major change made to the instrument was rebuilding the pulse compression setup. The optical configuration was adapted from Ref. [27] and a similar setup in the group. It is shown in Figure 2.6. After the white light generation, the pulses are collimated and sent through multiple pairs of chirped mirrors (DCM-9, (Laser Quantum, Novanta)) to compensate for the positive dispersion induced by filamentation. Roof mirrors are used to retroreflect the pulse in the vertical dimension and sent back through the chirped mirrors (see Figure 2.7). Overall, we could fit up to 28 pairs of bounces onto two pairs of chirped mirrors. The number of bounces can be adjusted for optimal pulse compression at the sample. We measured the pulse width by the time-dependent intensity of the transient gradient signal

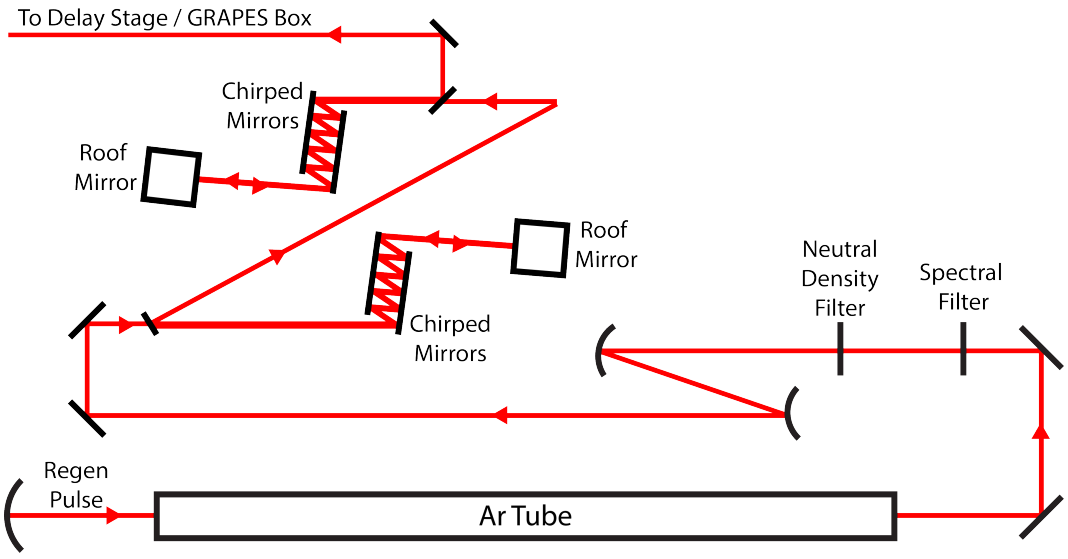

Figure 2.6: Newly built compression setup. After filamentaion in the argon tube, the pulse is spectrally filtered and attenuated prior to collimation with a pair of focusing mirrors. Then, the pulses pass through many pairs of chirped mirror bounces for compression. Roof mirrors displace the beam vertically, where they can pass through the chirped mirrors a second time prior to being picked off by a flat mirror.

measured in a methanol sample. Our new compression setup generated a pulse on the order of 10 fs. To further improve the setup for fine tuning of the compression, we will install a glass wedge to input dispersion into the beam path that can be continuously varied.

The new configuration offers comparable temporal compression capabilities as the MIIPS, but the power efficiency is improved by an order of magnitude. The MIIPS efficiency was approximately 5%, and the new system falls between 40-50% depending on the number of bounces needed. GRAPES has historically suffered from low fluences at the sample because the pulses are focused to lines rather than points. Now, we can achieve up to 500-1000 μW per pulse at the sample position. These values give us access to samples such as bacteriorhodopsin, which hugely scatters light and has previously required high pulse fluences to resolve the signal [26]. The increase in power also provides a higher upper value for power-dependent studies to test effects such as exciton-exciton annihilation.

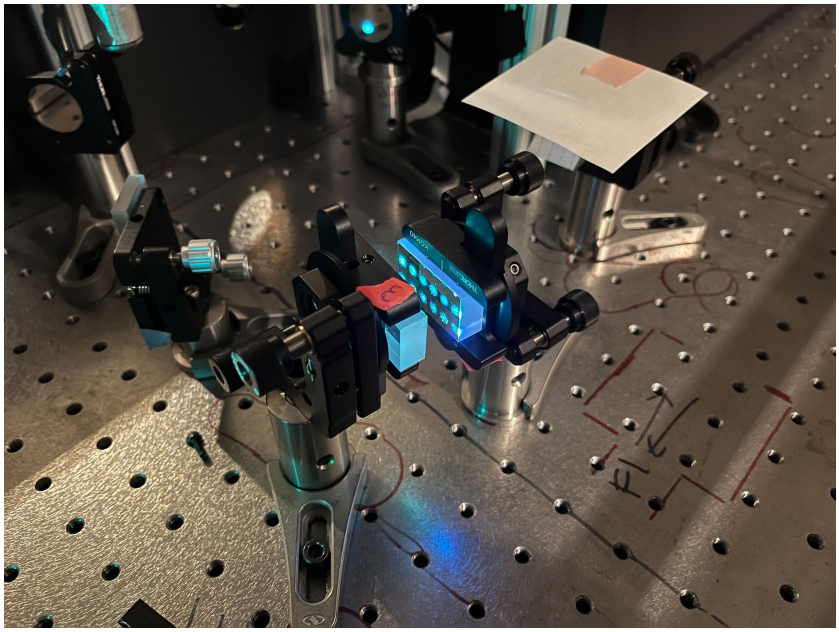

Figure 2.7: Stacked alignment of the pulses onto pairs of chirped mirrors. The light was spectrally filtered at 650 *nm* (shortpass) to demonstrate the blue light generated via the argon tube. Photo credit: Qijie Shen.

REFERENCES

[1] Ralph Jimenez, Graham R. Fleming, P. V. Kumar, and M. Maroncelli. Femtosecond solvation dynamics of water. *Nature*, 369(6480):471–473, 1994.

[2] Shaul Mukamel. *Principles of Nonlinear Optical Spectroscopy*. Oxford University Press, New York, 1995.

[3] John D. Hybl, Allison Albrecht Ferro, and David M. Jonas. Two-dimensional fourier transform electronic spectroscopy. *The Journal of Chemical Physics*, 115(14):6606–6622, 2001.

[4] M.L. Cowan, J.P. Ogilvie, and R.J.D. Miller. Two-dimensional spectroscopy using diffractive optics based phased-locked photon echoes. *Chemical Physics Letters*, 386(1):184–189, 2004.

[5] Tobias Brixner, Jens Stenger, Harsha M. Vaswani, Minhaeng Cho, Robert E. Blankenship, and Graham R. Fleming. Two-dimensional spectroscopy of electronic couplings in photosynthesis. *Nature*, 434(7033):625–628, 2005.

[6] P. Hamm and M. T. Zanni. *Concepts and methods of 2D Infrared Spectroscopy*. Cambridge UP, 2011.

[7] Andrei Tokmakoff. *Time-dependent Quantum Mechanics and Spectroscopy, tdqms.uchicago.edu*. 2014.

[8] T. Brixner, I. V. Stiopkin, and G. R. Fleming. Tunable two-dimensional femtosecond spectroscopy. *Opt. Lett.*, 29(8):884–886, Apr 2004.

[9] Tobias Brixner, Tomáš Mančal, Igor V. Stiopkin, and Graham R. Fleming. Phase-stabilized two-dimensional electronic spectroscopy. *The Journal of Chemical Physics*, 121(9):4221–4236, 2004.

[10] Minhaeng Cho. Coherent two-dimensional optical spectroscopy. *Chemical Reviews*, 108(4):1331–1418, 2008. PMID: 18363410.

[11] David M. Jonas. Two-dimensional femtosecond spectroscopy. *Annual Review of Physical Chemistry*, 54(1):425–463, 2003. PMID: 12626736.

[12] Elucidation of population and coherence dynamics using cross-peaks in two-dimensional electronic spectroscopy. *Chemical Physics*, 341(1):285–295, 2007. Ultrafast Dynamics of Molecules in the Condensed Phase: Photon Echoes and Coupled Excitations.

[13] M. Schatz, G.; Ratner. *Quantum Mechanics in Chemistry*, volume 2. Dover, Englewood Cliffs, NJ, 2002.

[14] Minhaeng Cho, Harsha M. Vaswani, Tobias Brixner, Jens Stenger, and Graham R. Fleming. Exciton analysis in 2d electronic spectroscopy. *The Journal of Physical Chemistry B*, 109(21):10542–10556, 2005.

[15] Elad Harel, Andrew F. Fidler, and Gregory S. Engel. Single-shot gradient-assisted photon echo electronic spectroscopy. *The Journal of Physical Chemistry A*, 115(16):3787–3796, 2011.

[16] Elad Harel, Andrew F. Fidler, and Gregory S. Engel. Real-time mapping of electronic structure with single-shot two-dimensional electronic spectroscopy. *Proceedings of the National Academy of Sciences*, 107(38):16444–16447, 2010.

[17] Kelly A. Fransted, Justin R. Caram, Dugan Hayes, and Gregory S. Engel. Two-dimensional electronic spectroscopy of bacteriochlorophyll a in solution: Elucidating the coherence dynamics of the fenna-matthews-olson complex using its chromophore as a control. *The Journal of Chemical Physics*, 137(12):125101, 2012.

[18] Haibin Zheng, Justin R. Caram, Peter D. Dahlberg, Brian S. Rolczynski, Subha Viswanathan, Dmitriy S. Dolzhnikov, Amir Khadivi, Dmitri V. Talapin, and Gregory S.

Engel. Dispersion-free continuum two-dimensional electronic spectrometer. *Appl. Opt.*, 53(9):1909–1917, Mar 2014.

[19] P. D. Dahlberg, G. J. Norris, C. Wang, S. Viswanathan, V. P. Singh, and G. S. Engel. Communication: Coherences observed in vivo in photosynthetic bacteria using two-dimensional electronic spectroscopy. *J Chem Phys*, 143(10):101101, 2015.

[20] Peter D. Dahlberg, Po-Chieh Ting, Sara C. Massey, Marco A. Allodi, Elizabeth C. Martin, C. Neil Hunter, and Gregory S. Engel. Mapping the ultrafast flow of harvested solar energy in living photosynthetic cells. *Nature Communications*, 8(1):988, 2017.

[21] P. D. Dahlberg, A. F. Fidler, J. R. Caram, P. D. Long, and G. S. Engel. Energy transfer observed in live cells using two-dimensional electronic spectroscopy. *Journal of Physical Chemistry Letters*, 4(21):3636–3640, 2013.

[22] Vadim V. Lozovoy, Igor Pastirk, and Marcos Dantus. Multiphoton intrapulse interference.iv.ultrashort laser pulse spectral phase characterization and compensation. *Optics Letters*, 29(7):775–777, 2004.

[23] V. P. Singh, A. F. Fidler, B. S. Rolczynski, and G. S. Engel. Independent phasing of rephasing and non-rephasing 2d electronic spectra. *The Journal of Chemical Physics*, 139(8):084201, 2013.

[24] Sara H. Sohail, Peter D. Dahlberg, Marco A. Allodi, Sara C. Massey, Po-Chieh Ting, Elizabeth C. Martin, C. Neil Hunter, and Gregory S. Engel. Communication: Broad manifold of excitonic states in light-harvesting complex 1 promotes efficient unidirectional energy transfer in vivo. *The Journal of Chemical Physics*, 147(13):131101, 2017.

[25] Philip J. M. Johnson, Alexei Halpin, Takefumi Morizumi, Leonid S. Brown, Valentyn I. Prokhorenko, Oliver P. Ernst, and R. J. Dwayne Miller. The photocycle and ultrafast

vibrational dynamics of bacteriorhodopsin in lipid nanodiscs. *Phys. Chem. Chem. Phys.*, 16:21310–21320, 2014.

[26] M. Liebel, C. Schnedermann, G. Bassolino, G. Taylor, A. Watts, and P. Kukura. Direct observation of the coherent nuclear response after the absorption of a photon. *Physical Review Letters*, 112(23):238301, 2014.

[27] Minjung Son, Sandra Mosquera-Vázquez, and Gabriela S. Schlau-Cohen. Ultrabroadband 2d electronic spectroscopy with high-speed, shot-to-shot detection. *Optics Express*, 25(16):18950–18962, Aug 2017.

CHAPTER 3

LEVERAGING DYNAMICAL SYMMETRIES IN TWO-DIMENSIONAL ELECTRONIC SPECTRA TO EXTRACT POPULATION TRANSFER PATHWAYS

The work presented in this Chapter adapted and reprinted with permission from: J.S. Higgins, A.R. Dardia, C.J. Ndife, L.T. Lloyd, E.M. Bain, and G.S. Engel, "Leveraging Dynamical Symmetries in Two-Dimensional Electronic Spectra to Extract Population Transfer Pathways," Under Revision at *Journal of Physical Chemistry A*.

We present a method to deterministically isolate population transfer kinetics from two-dimensional electronic spectroscopic signals. Central to this analysis is the characterization of how all possible subensembles of excited state systems evolve through the population time. When these dynamics are diagrammatically mapped using double-sided Feynman pathways where population time dynamics are included, a useful symmetry emerges between excited state absorption and ground state bleach recovery dynamics of diagonal and below diagonal cross peak signals. This symmetry allows removal of pathways from the spectra to isolate signals that evolve according to energy transfer kinetics. We describe a regression procedure to fit to energy transfer time constants and characterize the accuracy of the method in a variety of complex excited state systems using simulated two-dimensional spectra. Our results show that the method is robust for extracting ultrafast energy transfer in multistate excitonic systems, systems containing dark states that affect the signal kinetics, and systems with interfering vibrational relaxation pathways. This procedure can be used to accurately extract energy transfer kinetics from a wide variety of condensed phase systems.

3.1 Introduction to Population Analysis in Two-Dimensional Electronic Spectroscopy

Two-dimensional electronic spectroscopy (2DES) is a technique used extensively over the last two decades to study the excited state behavior of condensed phase systems[1, 2, 3, 4]. It has been used to interrogate excited state dynamics in photosynthetic light harvesting complexes[5, 6, 7, 8, 9, 10, 11], photobiological systems such as rhodopsin proteins[12, 13], synthetic molecular systems[14, 15, 16, 17], and materials systems[18, 19]. In 2DES, the electronic excitation energies of a system are correlated with the detection energies, revealing how the excited states are coupled[20, 21]. This coupling can be tracked through the population time with femtosecond precision to monitor the dynamics of processes such as exciton energy transfer (EET). 2DES is a versatile tool to unpack many aspects of excited state system and bath interactions in molecular systems, as one can study spectral lineshapes[22, 23, 24], coherence dynamics[3, 4], and population kinetics[25, 26] in the signal analysis.

Due to the overlap of multiple peaks and dynamic contributions to 2DES signals, it remains difficult to extract the exact kinetic rates that govern energy transfer[26, 27]. The illumination of a sample with an ultrafast laser source excites many different dynamical subensembles within the system[20, 28]. These dynamics can converge onto a single lineshape when the excitation and detection energies of the subensembles are similar, and many of these lineshapes overlap at finite temperatures. The population time evolution at any given point on a 2D spectrum is thus generated from many types of electronic or nuclear motion, such as EET, ground state recovery, coherence, spectral diffusion, and vibrational relaxation[29]. It has been shown that 2D spectroscopy is capable of resolving the entire energy transfer matrix of spectrally resolved complexes[27], and previous reports have extracted population transfer tables in 2D spectra with global fitting analyses[6] and by using a combination of decay associated and coherence associated spectra[30]. Another method uses a global fitting procedure based on the variable projection album to fit all spectral components to a

series of complex decaying exponentials to generate decay-associated spectra and coherence-associated spectra[31].

In this paper, we extend an analysis method to fit to the kinetic parameters for population transfer in two-dimensional spectra. This method has been used to differentiate the kinetics of excitonic pathways in photosynthetic light harvesting systems[32], but it can in principle be exported to others. The method differs from other methods in that it accounts for all possible microscopic dynamics of the system and their relative signal contribution and removes signals that interfere with energy transfer kinetics. The paper is outlined as follows. We first describe the theory of nonlinear spectroscopy and how Feynman pathways allow one to calculate the relative probability that dynamical subensembles contribute to the signal. We then enumerate the types of Feynman pathways in excitonic systems and their relative signal strengths, spectral location, and time evolution. We describe signal processing steps to extract time constant information and methods to improve the accuracy. We then test the method's accuracy using simulated two-dimensional electronic spectra in a diverse set of systems with increasing complexity, to find that the method is robust to molecular complexes with dark states and interfering resonant vibrations.

3.2 Molecular Response Functions and Their Time Evolution

In 2DES, a nonlinear signal is generated in response to three pulses acting on the system[20, 28]. The pulses coherently couple the molecular dipoles and generate the third order polarization:

$$\begin{aligned} P^3(t_1,t_2,t_3) = &\int_0^\infty dt_3 \int_0^\infty dt_2 \int_0^\infty dt_1 \\ &\times E_3(t-t_3)E_2(t-t_3-t_2)E_1(t-t_3-t_2-t_1)R^3(t_3,t_2,t_1). \end{aligned} \tag{3.1}$$

This polarization is dependent on three distinct time variables representing the time delay

between each pulse, referred to as the coherence time t_1, the population time (or waiting time) t_2, and the detection time t_3. In a semiclassical formalism, the three pulses are treated classically, and the quantum mechanical information of the molecular system is encapsulated in the third order response function R^3:

$$R^3(t_3, t_2, t_1) = \left(\frac{i}{\hbar}\right)^3 \langle \mu(t_3 + t_2 + t_1)[\mu(t_2 + t_1), [\mu(t_1), [\mu(0), \rho(-\infty)]]]\rangle, \qquad (3.2)$$

Response functions describe how the ensemble of states reacts to the dipole perturbation induced by the laser pulses[33]. The molecular density matrix ρ is acted on by the dipole operator μ[21]. The nested commutators allow all possible combinations of dipole operators to act on either side of the density matrix, and the brackets $\langle\ \rangle$ depict an average over the entire thermal ensemble. The magnitude of the transition dipole moment terms μ_{ij}=$\langle\psi_i|\mu|\psi_j\rangle$ determine the relative probability of transitioning between states i and j[34]. With multiple dipole interactions acting on the density matrix, permutations from the nested commutators, and averaging over the thermal ensemble, there is a large number of terms in the total third order response function. These terms scale rapidly with the number of dipole-accessible electronic, vibrational, and vibronic states in the system. Each term in the response function describes a particular subensemble, each of which has a probability of contributing to the signal depending on intrinsic properties of the system, such as the transition dipole moments or the transfer rate between the states coupled to the subensemble population.

In this analysis, we use double-sided Feynman pathways to visualize and track the components of the third order response function (Equation 3.2)[21, 28, 35]. Feynman pathways have been used in many physical systems to visualize the behavior of many-body dynamics[36]. An example Feynman pathway that undergoes population time dynamics is shown in Figure 3.1. The diagonal lines represent pulses driving transitions on either the bra or ket side of the density matrix. Over each time interval, the signal evolves as either a coherence or a population. For coherences, the signal oscillates with a frequency given by the energy

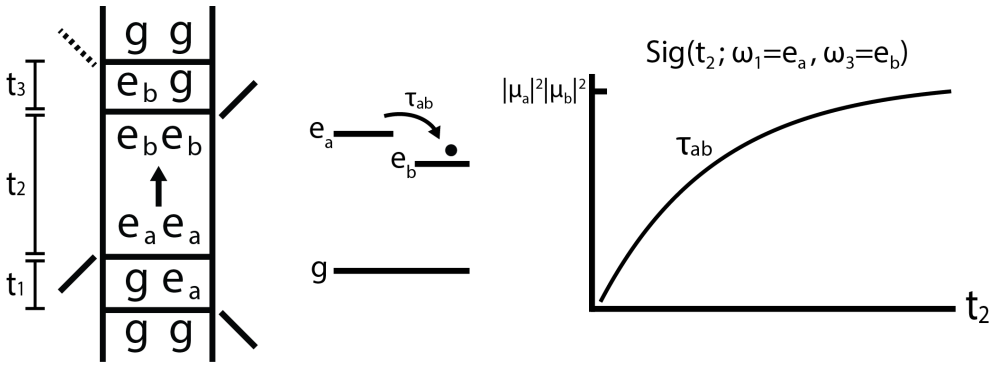

Figure 3.1: Double-sided Feynman pathway representing a dynamical subensemble that undergoes population transfer from state e_a to e_b during the population time, t_2. The excitation and detection axes ω_1 and ω_3 are respectively given by the bra-ket energy difference during t_1 and t_3. The signal evolution through t_2 is proportional to the population of excitation probed from e_b that began in e_a at t_2=0. As such, the pathway will evolve with the kinetics of energy transfer such that its rise time will be given by τ_{ab} and its decay will be given by the loss of e_b population, τ_{bL}. The signal strength is weighted by the transition dipole magnitudes of the four laser interactions, in this case $|\mu_a|^2|\mu_b|^2$.

difference between the two states and decays with a dephasing time τ_{deph}:

$$G(t)\alpha \exp(i\omega_{ij}t - t/\tau_{deph}) \tag{3.3}$$

Here, G(t) is the Green function operator that drives time evolution to time t, and ω_{ij}=(E_i - E_j)/$\hbar$[20, 21]. The coherence generated in the third time interval produces the signal, which we represent with the dashed line. For populations, the signal strength is proportional to the population of the subensemble at time t[35]. As such, the signal will increase or decrease with the microscopic population dynamics in the system. For example, the pathway shown in Figure 3.1 undergoes population dynamics during the population time t_2, where excitation energy transfers from the excitonic state a to state b with a phenomenological time constant τ_{ab} (shown in the adjacent two excited state system). The signal during t_2 that evolves from this pathway, shown to the right, is directly proportional to the population of exciton b that accumulates due to energy transfer from exciton a. The signal strength is weighted by the transition dipole moments for each laser interaction (in this case $|\mu_a|^2|\mu_b|^2$, shown as the

signal peak).

The population kinetics during the population time t_2 and how the dynamics of all Feynman pathways contribute to the signal are the principle concern of this analysis. We consider each Feynman pathway to represent a particular dynamical subensemble of the system, carrying its own population time kinetics due to the system's microscopic behavior. Its relative contribution to the total signal is determined by the dephasing times of the coherences, the kinetics of the populations (typically during t_2), and the transition dipole amplitude from the four light-matter interactions. The 24 possible pathways for a two excited state system with a shared ground state are shown in Figure 3.2. These 24 Feynman pathways constitute a basis set that can be used to describe the total response of a larger set of states, including vibrational energy levels.

3.3 Time Constant Extraction Method

There are symmetries in the dynamical evolution of diagonal and below diagonal cross peaks of 2D spectra that we can exploit to isolate the time constants for energy transfer. The strongest signals in the diagonal and below diagonal peaks are the ground state bleach (GSB), stimulated emission (SE), and excited state absorption (ESA) signals. For any given diagonal peak a and cross peak a-b, the goal of this analysis is to remove all GSB recovery signals and extraneous ESA signals, thus isolating the dynamics that evolve during the population time due to a-b energy transfer. These signals can be fit exactly to kinetic equations to isolate the phenomenological time constants for energy transfer. The following section describes the Feynman pathways (Figure 3.3), approximations, and steps that this method entails.

Figure 3.3A-B shows the SE, ESA, GSB, and GSB recovery population and their subsequent population time evolution for a mock exciton e_a diagonal peak and exciton e_a-e_b below diagonal cross peak. For the stimulated emission pathways, the population time dy-

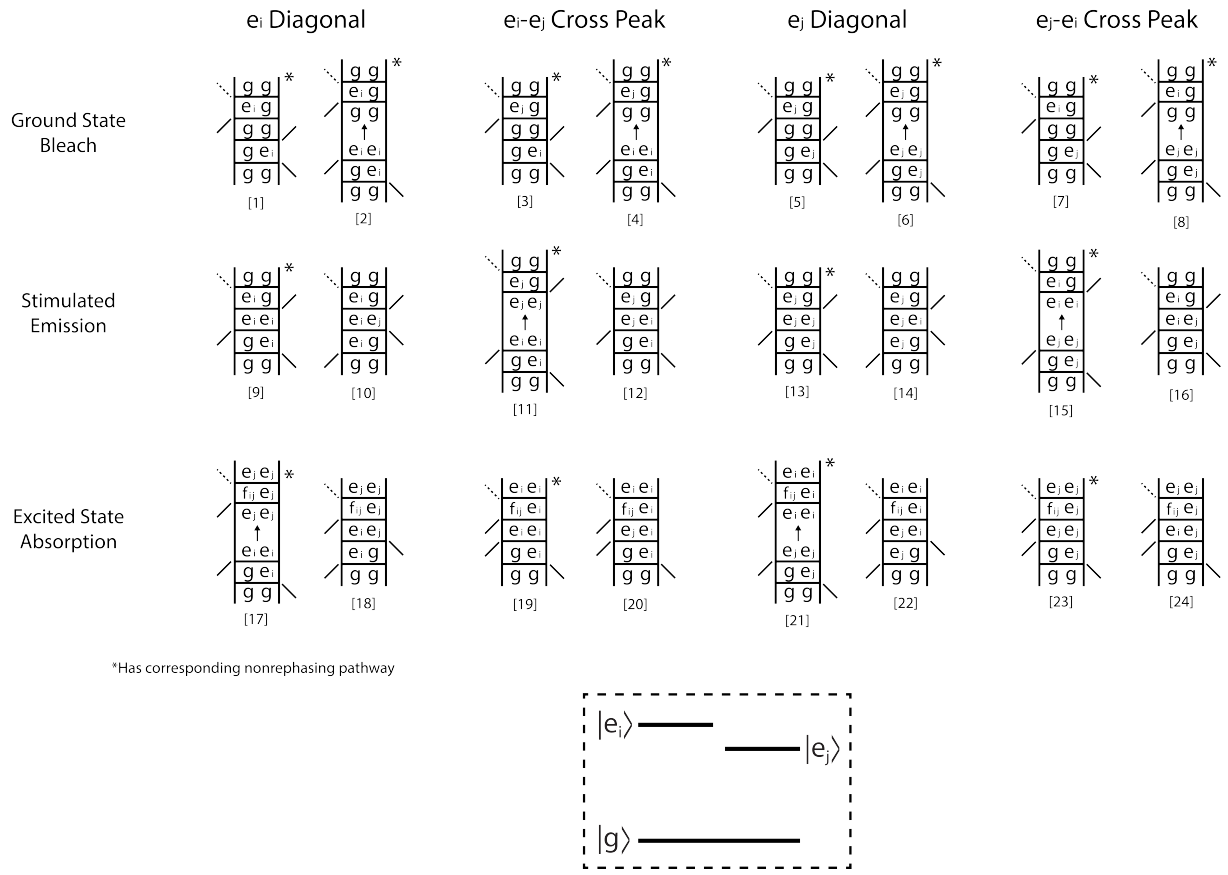

Figure 3.2: Possible electronic Feynman pathways for a system with two excited states, e_i and e_j, that share a common ground state. The two states comprise two diagonal peaks and two cross peaks. Each peak contains two ground state bleach pathways, two stimulated emission pathways, and two excited state absorption pathways that have distinct time evolution in the population time, t_2. The symbol (*) denotes that there is a corresponding nonrephasing pathway. These 24 pathways form a basis set to simulate multi-state two-dimensional spectra.

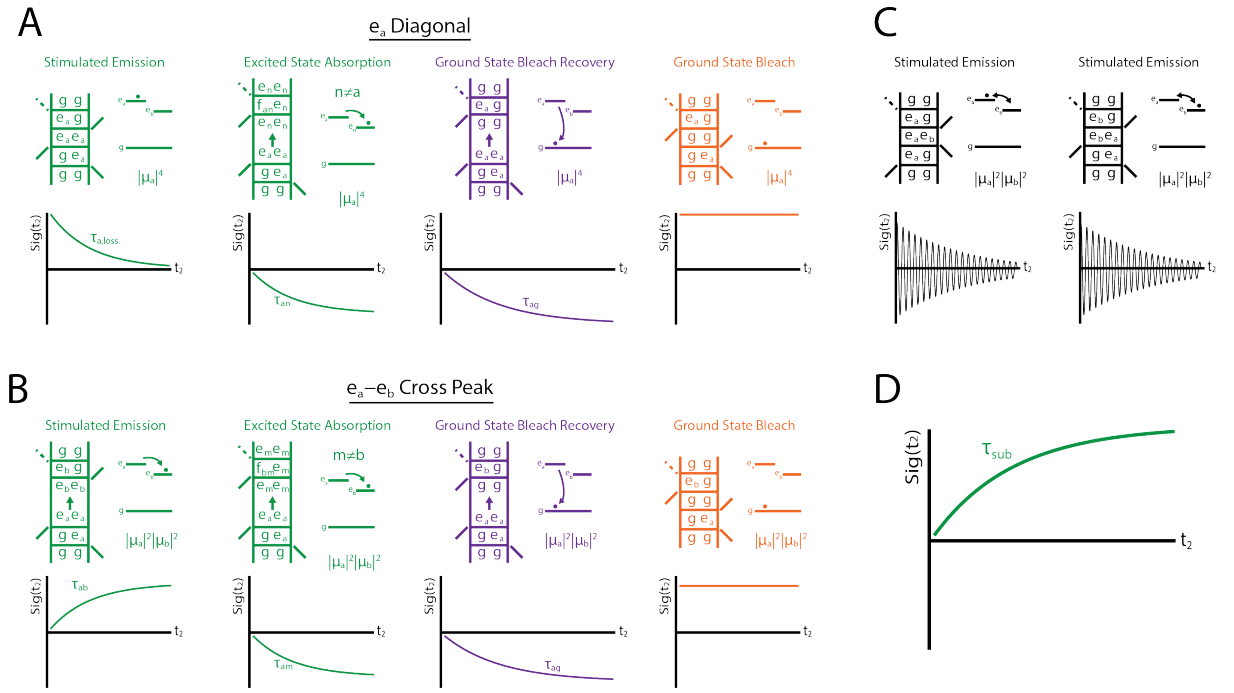

Figure 3.3: Excitonic Feynman pathways between diagonal peaks and corresponding below diagonal cross peaks possess dynamical symmetries that allow for isolation of population transfer signals. The major contributing pathways to these peaks (A, B) are stimulated emission, excited state absorption, ground state bleach recovery, and ground state bleach signals. The ground state bleach recovery signals evolve with the same kinetics given by τ_{ag} on both peaks, but the stimulated emission pathways evolve according to their respective population transfer kinetics. The τ_{ag} time is typically much larger than energy transfer time constants, though they are plotted here on a similar scale for clarity. One pair of excited state absorption pathways evolve with identical t_2 kinetics as the stimulated emission signals, while the others are subtracted out (see Figure 3.4). The four pathways on the diagonal and cross peak have the transition dipole strength $|\mu_a|^4$ for the diagonal and $|\mu_a|^2|\mu_b|^2$ for the cross peak. C) Coherence pathways do not contribute to the monotonic evolution of the total signal. D) The normalized diagonal and cross peak signals can be subtracted to remove the bleach recovery pathways and symmetrical excited state absorption pathways. What remains is a signal whose kinetics evolve according to population transfer. The subtracted signal can be used as a parameter to fit to energy transfer time constants. Note: for each rephasing pathway that undergoes population evolution during t_2, there is a corresponding nonrephasing pathway that undergoes the same population time dynamics, not shown here for brevity.

namics evolve differently between diagonal and below diagonal peaks. The diagonal pathway decays with population time due to loss of exciton e_a population as it transfers to exciton e_b, the ground state, or to other states in the system. The cross peak pathway increases with population time as e_a-e_b energy transfer occurs but then will decrease as the population subsequently leaves exciton e_b. At both the e_a diagonal and e_a-e_b cross peak, the ground state bleach and bleach recovery pathways undergo the same time evolution in the population time with a time constant given by the relaxation from exciton a to the ground state. The only difference between the bleach signals of each region is the interaction of the third pulse. The diagonal pathway produces a $|e_a\rangle\langle g|$ coherence while the cross peak pathway produces a $|e_b\rangle\langle g|$ coherence. For clarity, the bleach recovery traces are plotted in Figure 3.3 with a similar time scale as the energy transfer dynamics. However, recovery to the ground state typically occurs on much slower timescales in most molecular systems (on the order of nanoseconds), meaning they will contribute minimally to short time signals. The presence of features such as conical intersections can speed up the bleach recovery and bring the time constant into the energy transfer regime[12, 37], so we include bleach recovery dynamics here to preserve the generalizability of the method. For coherence pathways (Figure 3.3C), signals associated with coherences will be nearly symmetric about zero (depending on the speed of dephasing and oscillatory frequency) and therefore should not contribute significantly to the retrieved dynamics of the signals. Therefore, the signals should be primarily due to population dynamics.

We consider excited state absorption (ESA) pathways from physical systems in two common limiting cases: weak biexciton coupling and infinite biexciton coupling. In ESA pathways, the first two pulses put the system into a singly excited state, and the third pulse drives a transition to a higher excited state. In the case of infinite biexciton coupling, there will be no transition to the higher excited state, so the ESA pathways have no signal strength. In the limiting case of weak biexciton coupling, we assume that the two exciton manifold states

are spanned by direct products of the single exciton states. That is, the biexciton energies are approximately the sum of the single exciton energies.

For a standard ESA pathway on the e_a-e_b cross peak, the first two pulses put the system into an e_a population during t_2, and the third pulse generates the biexciton state f_{ab}. This pathway will evolve over the population time in proportion to the loss of population from exciton a (see Figure 3.4). Other ESA pathways on the cross peak include exciton energy transfer (Figure 3.3B). Here, energy will transfer from state a to any state m over the population time, and the third pulse will generate the biexciton state f_{bm}. ESA pathways for all m states are possible except for $m{=}b$ (because the biexciton state f_{bb} is not viable). For generalizability, we include the case $m{=}a$ to be the standard pathway described at the beginning of this paragraph. Interestingly, there are also energy transfer ESA pathways on the diagonal peaks. On the e_a diagonal (Figure 3.3A), energy transfers from exciton a at the beginning of the population time to exciton n, and the third pulse generates a biexciton state f_{an}. There will be an ESA pathway for each n state with the exception of $n{=}a$ (for the same reason described above). All of the ESA pathways described here scale with the same transition dipole strength as the corresponding SE and GSB pathways. However, the amplitudes of the signals are likely weaker due to lifetime broadening of the shorter-lived biexciton coherence over t_3. The shorter dephasing time spreads the signal over a broader area on the detection axis, which reduces the contribution to each point[33, 38]. The relative weakness of ESA signals can be seen in the largely positive diagonal and below-diagonal 2DES signals of photosynthetic light harvesting complexes[6, 8, 25, 39, 40], demonstrating that the positive SE and GSB pathways produce stronger signals in these regions.

For every set of ESA pathways on a diagonal peak a and below diagonal cross peak a-b, all pathways not corresponding to the t_2 evolution of stimulated emission pathways will evolve with the same kinetics on the diagonal and cross peak. This is illustrated in an example three exciton system in Figure 3.4A-B. The exciton 3 diagonal has two ESA

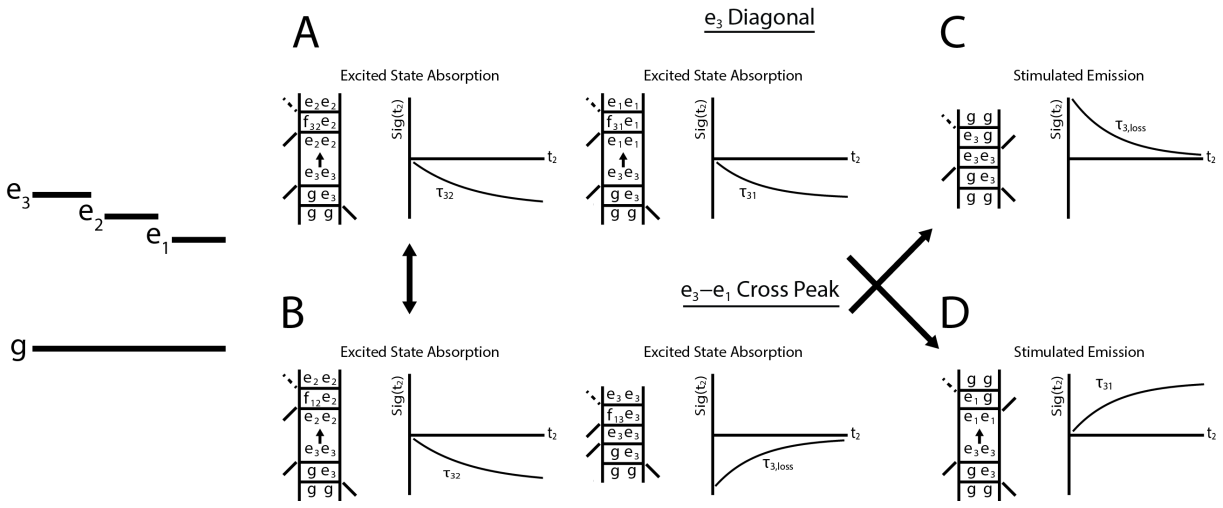

Figure 3.4: Representative excited state absorption pathways for a mock three exciton system. A) Exciton 3 diagonal and B) exciton 3-1 cross peak excited state absorption pathways and their corresponding population time evolution. C) Exciton 3 diagonal and D) exciton 3-1 cross peak stimulated emission pathways and corresponding population time evolution. Arrows between Feynman pathways indicate identical population time kinetics.

pathways (downhill energy transfer to excitons 1 and 2), and the exciton 3-1 cross peak has two ESA pathways (loss of exciton 3 and downhill energy transfer to exciton 2). Between these two peaks, the exciton 3-2 energy transfer pathways evolve according to the same kinetics. In contrast, the remaining pathways evolve differently between the diagonal and cross peak. The 3-1 energy transfer pathway on the diagonal evolves with the same kinetics as the SE pathway on the cross peak (but with a negative sign, see Figure 3.4D). Similarly, the exciton 3 cross peak pathway evolves according to the diagonal SE pathway (but again, with a negative sign, see Figure 3.4C). This example can be inductively generalized to any n exciton system. These symmetries allow us to remove extraneous ESA pathways unrelated to energy transfer between the two excitons.

We take advantage of these symmetries in the bleach recovery and ESA pathways to remove their contribution to the signal evolution. At each peak, the pathways scale with the same transition dipole strength, but the strength is different between peaks. We correct for this difference by first normalizing each signal:

$$norm(Sig(T)) = \frac{Sig(T) - Sig(T_i)}{|Sig(T_f) - Sig(T_i)|} \tag{3.4}$$

Here, T_i and T_f are the initial and final t_2 values for each time interval. The normalization step removes the amplitude differences between the diagonal and cross peaks but keeps the difference curvature due population transfer rates. We subtract the normalized diagonal signal from its corresponding normalized lower diagonal cross peak signal to remove the bleach recovery contribution, maintain the stimulated emission kinetics, and keep only the ESA pathways that correspond to SE kinetics (Figure 3.4). Because the relevant ESA traces evolve equally and oppositely to the SE kinetics on the corresponding peak, the subtraction step will be additive for these kinetics. The time constant for the subtracted signal is a parameter that can be used to fit to energy transfer time constants.

The schematic of steps for isolating the kinetic rate constants is shown in Figure 3.5. For clarity, we use sequential exciton numbering, where exciton 1 is the lowest energy. First, diagonal and cross peak regions of the excitonic peaks are averaged using circular windows. Averaging over finite regions removes the bath dynamics from the signal such as vibrational relaxation and spectral diffusion. These dynamics affect the lineshape evolution in the spectra, and averaging removes this effect so that the signal evolves in time exclusively from excitonic dynamics. Then, a population time interval is selected for curve fitting, typically from times between 50 and 100 fs to about half the experimental time, typically around 1000 fs. The fitting procedure is then performed starting with energy transfer between the lowest two excitonic states. The 2 diagonal and 2-1 cross peak are normalized according to Equation 3.4 and then subtracted from one another. If necessary, the τ_{1L} time constant can be obtained from the exciton 1 diagonal. The bleach recovery signal is removed in the subtraction. The stimulated emission signals and remaining ESA signals evolve according to 2-1 energy transfer. Thus, the fit time constant for the subtracted signal must be the energy transfer time constant τ_{21}.

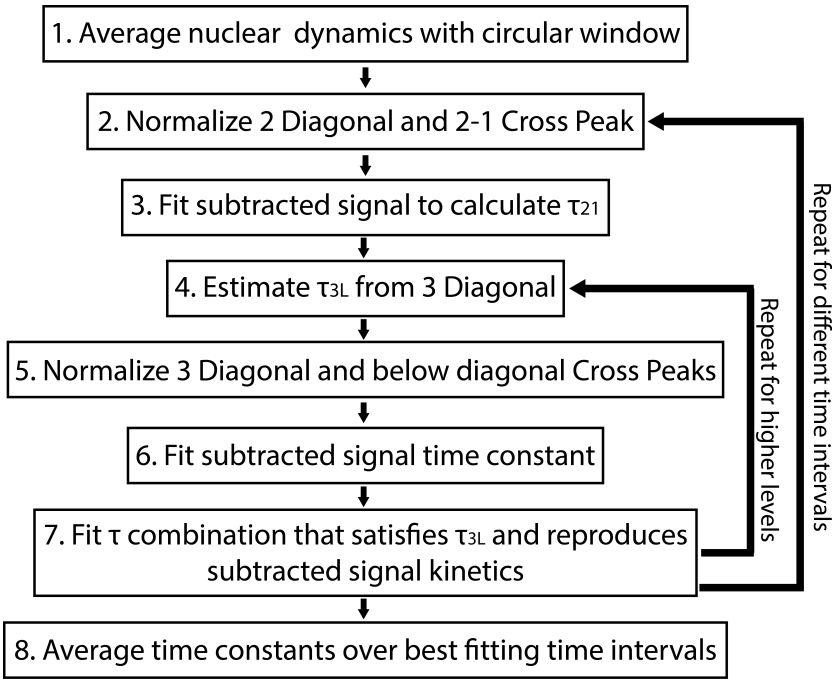

Figure 3.5: Scheme for extracting kinetic time constants from two-dimensional spectroscopic signals. Time constants are calculated from lowest to highest exciton energy. The entire procedure is repeated for multiple time intervals, and those with the best fitting subtracted time trace are averaged to generate the most accurate time constants.

The procedure then moves to the next highest excitonic state. The time constant $\tau_{3\mathrm{L}}$ ('3 loss,' or transfer from exciton 3 to other states) is estimated as the short time constant in a biexponential fit to the 3 diagonal. This τ_{3L} value must satisfy the other energy transfer time constants τ_{32} and τ_{31} according to $k_{3L}=\frac{1}{\tau_{3\mathrm{L}}}=\frac{1}{\tau_{31}}+\frac{1}{\tau_{32}}$. The 3 diagonal and below diagonal cross peaks are then normalized, and one cross peak is selected to be subtracted from the diagonal. Typically, the 3-1 cross peak is chosen to ensure a good fit to the subtracted time constant because the peak signal monotonically increases over short experimental times, rather than the 3-2 cross peak, which often has flatter curvature due to energy transfer in and out of exciton 2. The normalized diagonal and cross peak signals are subtracted from one another, and the remaining signal is fit to a set of kinetic parameters. These parameters are typically a monoexponential decay function in excitonic signals, though other functions can be used if they better fit the data. The subtracted fit is used as an empirical constraint for the numerical procedure. Solutions to differential equations for energy transfer are numerically calculated to fit to the diagonal and cross peak stimulated emission signals, which are also normalized, subtracted, and fit to the same kinetic parameters. The resulting time constant value is compared to the experimental data. The calculation is repeated for all short time values of τ_{31} and τ_{32} under the constraint of $\tau_{3\mathrm{L}}$, and the combination that best matches the experimental subtracted time constant is selected as the best fit for energy transfer. (Note: τ_{21} has already been calculated, as it is used as a parameter in the differential equation.) The numerical fitting procedure is done for higher energy levels as necessary.

This entire analysis, starting from the normalization of the 2 diagonal and 2-1 cross peak, is then repeated with different time intervals until the time interval spans the entire experimental time, typically 2000 fs. For each time interval, the goodness of fit for the numerical signals is evaluated by calculating the root-mean-squared difference between the experimental subtracted 2D signals and the numerically calculated subtracted signals. There is a range of best-fitting time intervals are averaged over to produce the final time constant

values for EET. This final averaging step minimizes error due to the arbitrary choice of time interval. In the Supporting Information, we discuss how this method can be extended to other systems.

We demonstrate this process with data from the Fenna-Matthews-Olson (FMO) complex from green sulfur bacteria in reducing conditions. This analysis is conducted in the following study without the final population time interval average[32]. Figure 3.6A shows a two-dimensional spectrum of FMO at population time 800 fs. The three diagonal peaks represent excitons 4, 2, and 1, which constitute a major energy transfer pathway through the complex[25]. The time traces are averaged using a 70 cm^{-1} circular window. Figure 3.6B-E depicts the signal subtraction process using a population time window range from 100 to 2000 fs. Figure 3.6B is the monoexponential fit to the normalized 2 diagonal subtracted from the normalized 2-1 cross peak, which isolates the τ_{21} time constant. Figure 3.6C is the fit to the averaged exciton 4 diagonal peak, where the short time constant τ_1=225 fs is estimated as the exciton 4 loss time constant. The monoexponential fit to the normalized 4 diagonal subtracted from the normalized 4-1 cross peak (Figure 3.6D) is then reproduced in the numerical simulation (Figure 3.6E) such that τ_{41} and τ_{42} satisfy the τ_{4L} constraint. After repeating this process over population time end points from 600 to 2000 fs, we find that the lowest root-mean-square error falls in the range from 1700 to 2000 fs (Figure 3.6F). After averaging over this range, we obtain the final averaged time constants $\tau_{21,ave}$=453 fs, $\tau_{42,ave}$=409 fs, and $\tau_{41,ave}$=496 fs.

3.4 Global Response and Method Accuracy for Excitonic Systems

We simulated two-dimensional spectra of multi state systems by calculating each component of the total response in the time domain, following the procedure laid out in Ref. [28]. All combinations of Feynman pathways from a system with two excited states (Figure 3.2)

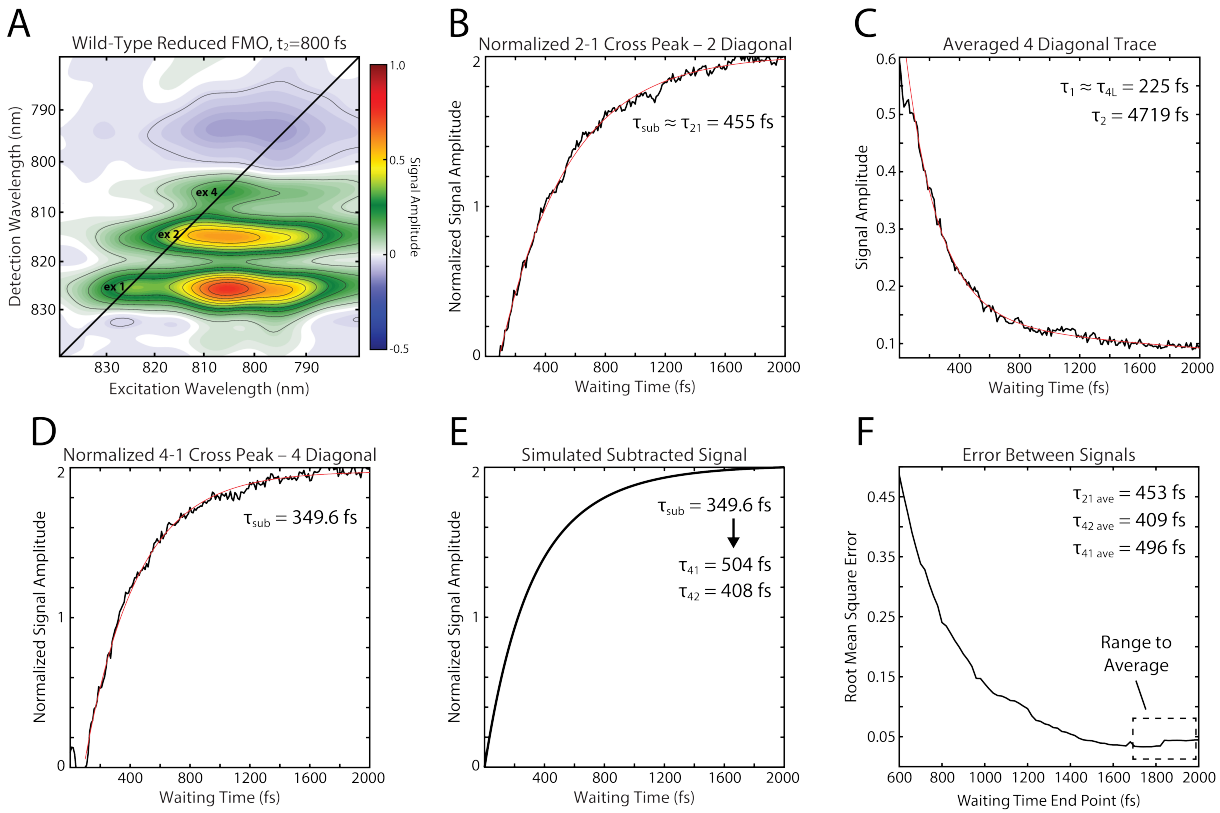

Figure 3.6: Demonstration of the analysis method using the Fenna-Matthews-Olson complex. A) Absorptive population time spectrum at t_2=800 fs. Shown are the exciton 1, 2, and 4 diagonal peaks and their corresponding below diagonal cross peaks. Each peak region is averaged using a 70 cm^{-1} window. B) Fit to the normalized 2 diagonal subtracted from the normalized 2-1 cross peak traces. The monoexponential time constant is approximately equal to the τ_{21} energy transfer time constant 455 fs. C) Biexponential fit to the averaged exciton 4 diagonal trace. The first time constant is used as the 4 loss time. D) Fit to the normalized 4 diagonal subtracted from the normalized 4-1 cross peak traces. E) Simulated subtracted signal reproduces the signal time constant in panel (D) using τ_{41}=504 fs and τ_{42}=408 fs, which satisfies the constraint of τ_{4L}. F) This process is repeated using a series of population time ranges, and the root-mean-square error between the signals in (D) and (E) are calculated. The time constants are averaged over the lowest error region to obtain the final energy transfer time constants.

were used to form a basis set to model systems with multiple excited states, taking care not to double count pathways. We then Fourier transformed the t_1 and t_3 axes of the total response to obtain ω_1 and ω_3. Unless stated otherwise, the spectra were simulated near the limit of infinite biexciton coupling. Three classes of energy transfer systems were simulated, shown in Figure 3.7, to understand the accuracy of this method under differing excited state structures. The first system (Figure 3.7A) is a standard excitonic model, featuring downhill energy transfer between three electronic excited states. All states are dipole allowed from the ground state and have a ground state recovery time τ_g that is at least an order of magnitude higher than the energy transfer times. The second system (Figure 3.7B) is the dark state system, where a fourth electronic state is added with no transition dipole moment between the state and the ground state. Excitons are allowed to transfer between this state and the three bright excited electronic states, however, so its presence will affect the EET kinetics of the three bright excitons. In this analysis, we include systems with a dark state between excitons 1 and 2 and between excitons 2 and 3 and show that the dark state only affects the extracted kinetics of adjacent excitons. In the third system (Figure 3.7C), a vibrational energy level is added to each excited state whose energy gap is resonant with the adjacent exciton energy gap. In this system, vibrational relaxation within one exciton will create below diagonal cross peak signals that constructively interfere with EET signals. We will show that while dark state kinetics and vibrational relaxation affect the cross peak signal growth, the analysis method still accurately extracts the kinetic parameters for exciton energy transfer.

We test the method's accuracy in the two limiting ESA cases and the assumption that coherence pathways don't impact the method. We characterize the accuracy of the standard system parameters when the relative contribution the signal strength of excited state absorption and coherence pathways is increased (Figure 3.8). The former is done by increasing the dipole ratio μ_{fe}/μ_{eg}, where μ_{eg} is the dipole moment of the ground to excited state transi-

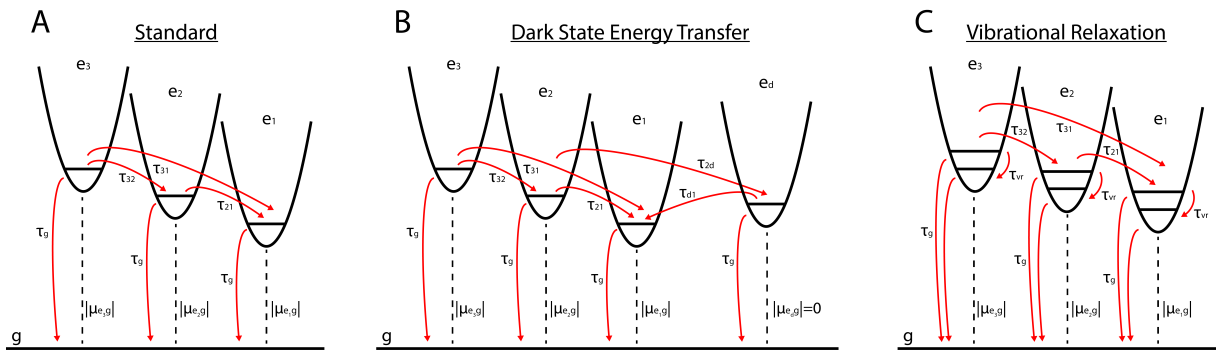

Figure 3.7: Three types of systems are used in global response calculations. A) Standard electronic system with three bright excitonic states allowing downhill energy transfer and slow relaxation to the ground state. B) Dark state system, where a fourth excitonic state is added to the standard system. This state has no oscillator strength with the ground state but still participates in downhill energy transfer with other excitons. Shown is a dark state between excitons 2 and 1, but the same analysis is also conducted using a dark state between excitons 3 and 2. C) Vibrational system, where vibrational modes resonant with the exciton energy gap are added to the standard system. Vibrational relaxation constructively interferes with below diagonal cross peak dynamics and slows the signal evolution.

tion, and μ_{fe} is the dipole moment from the first excited state to the biexciton state. Figure 3.8A shows the error in the standard three exciton system as the μ_{fe}/μ_{eg} dipole ratio ranges from zero to one. In most cases, the error falls below 15%, demonstrating that the method works between the two limiting cases of infinite and weak biexciton coupling. For coherence pathways, dephasing times in the hundreds of femtoseconds range (which are typical dephasing times for vibrational and vibronic coherences[41, 42, 43]) might interfere with the exponential pathways involving energy transfer. The presence of long-lived coherent signals observed in multiple photosynthetic systems[5, 41, 44, 45, 46] might affect the time constant extraction. Figure 3.8B shows the error as the dephasing time for excited state coherences is increased from below 100 fs to 500 fs. The dephasing time has little effect on the accuracy for any of the three EET time constants. The coherence pathways modulate the signal in the population time, but they do little to affect the monotonic signal kinetics and therefore the exponential fits. This result will hold true for both excited state electronic or vibronic coherences and ground state vibrational coherences.

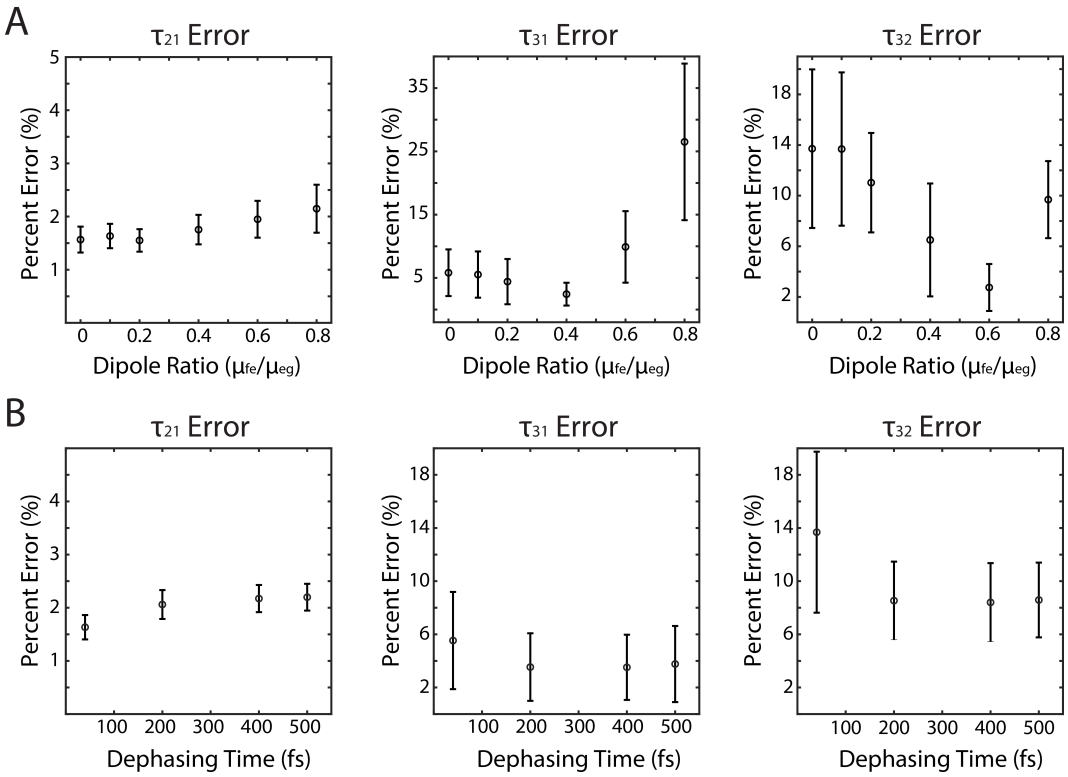

Figure 3.8: Error analysis for interfering excited state absorption and coherence pathways in the kinetic extraction method for a variety of time constants in the standard system. A) Percent error for each time constant as a function of relative transition dipole magnitude between μ_{fe} and μ_{eg}, which corresponds to the relative signal strength of the excited state absorption and ground state bleach/stimulated emission pathways, respectively. B) Percent error as a function of dephasing time for excited state electronic coherences. Long-lived coherences have little effect on the accuracy of the method because they do not contribute to monotonic signal growth or decay.

We now compare the method's accuracy for the systems shown in Figure 3.7 using multiple kinetic schemes for energy transfer. Tables 3.1-3.4 show the percent errors for each time constant for the standard system, two dark state systems, and the vibrational system. For the standard system (Table 3.1), we find that the method is accurate for energy transfer systems with subpicosecond kinetics, as all but one time constant is fit to within 15% accuracy. The τ_{31} time constants are all fit within 10% accuracy, and the τ_{21} constants are all extracted within 5% accuracy. In schemes with picosecond energy transfer constants, the method tends to inaccurately calculate the slow time constant with errors above 20%. However, the accuracy of the subpicosecond time constants remains within 15% (Table 3.1). This effect is likely due to the regression more accurately fitting signals that evolve several e-folds through the population time (as experimental timeframes typically range from 0 to 2000 fs). We should note that for the standard system, averaging over multiple time intervals does not significantly improve the accuracy of the method.

We find that dark states only affect the accuracy of the time constants for adjacent excitons that are directly involved in energy transfer with the dark states. Table 3.2 shows the method accuracy for multiple kinetic schemes when a dark state is added between excitons 1 and 2. For each scheme, the energy transfer to ($\tau_{2\mathrm{d}}$) and from ($\tau_{\mathrm{d}1}$) the dark state is changed to test how the dark state kinetics affect the method's accuracy. All τ_{21} errors are greater than 15%. This error is due to the kinetic sink effect between excitons 2 and 1. However, τ_{31} and τ_{32} remain accurate for all schemes where energy is allowed to flow to and from the dark state, with many of the errors falling below 5%. This result is notable because the presence of dark states on lower exciton manifolds does not disrupt the accuracy of the calculation for higher excitonic states despite the fact that the fit to τ_{31} and τ_{32} relies on knowledge of τ_{21}. Table 3.3 shows the method accuracy when a dark state is added between excitons 2 and 3. In this model, τ_{21} remains accurate for all kinetic schemes within 5%. However, τ_{32} and τ_{31} are each off by >30% for every scheme for the same kinetic sinking effect described

above. In the method, τ_{32} and τ_{32} are simultaneously calculated to reproduce the time constant of the subtracted signal (see Figure 3.5, step 7). An error in one time constant due to the kinetic trap would therefore introduce an error in the other time constant. For both dark state systems, averaging over multiple time intervals does not improve the method accuracy. We should note that the method is only accurate when excitons are allowed to flow in and out of the dark state. Tables 3.2-3.3 show the method is highly inaccurate for all time constants when energy does not flow back. Thus, in systems containing dark states that couple to the excitonic states, knowledge of the electronic states and their couplings must be known*a priori* to know which calculated time constants will be accurate.

In the final step of the analysis, multiple time intervals are averaged to minimize errors due to arbitrary choice of population time intervals (Figure 3.5, step 8). This step does not improve the accuracy of the standard and dark state systems, but it markedly improves the accuracy of the vibrational system. Table 3.4 shows the method accuracy for multiple kinetic schemes when the slow relaxation of resonant vibrations interferes with below diagonal energy transfer cross peaks, as described in the previous section. The analysis method remains accurate to 10% for all time constants after averaging over multiple population time intervals. For the vibrationsl system, we find that the fits with the smallest least squares fit to the subtracted signal and those which most accurately extract the energy transfer time constants occur when shorter time intervals are averaged (e.g. from 50–1050 fs to 50 –1775 fs). This range is long enough to capture multiple energy transfer e-folds but short enough to minimize the effect of picosecond signal changes due to vibrational relaxation. This result is in contrast to the purely electronic standard and dark state kinetic systems, where the smallest least squares error and most accurate time constant fits occur over larger time intervals. In experimental molecular spectra, there will be slow signals due to vibrational relaxation and other nuclear motion not completely removed from the signal averaging[47, 48]. It is necessary to average over the time intervals to most accurately extract

τ_{21} (fs)	Error w/o average	Error w/ average	τ_{32} (fs)	Error w/o average	Error w/ average	τ_{31} (fs)	Error w/o average	Error w/ average
450	1.7%	1.6%	400	13.6%	13.1%	500	5.4%	5.2%
800	2.0%	1.8%	400	9.7%	7.6%	500	1.6%	1.1%
450	1.8%	1.8%	800	22.0%	22.0%	500	5.8%	5.8%
450	1.4%	1.3%	400	14.1%	12.0%	800	11.8%	10.0%
440	1.3%	1.0%	225	10.9%	10.9%	1500	21.9%	25.7%
450	1.9%	1.6%	1500	39.7%	29.1%	500	5.6%	4.5%

Table 3.1: Error in the standard three excited state excitonic system using six sets of energy transfer time constants. The first four sets have only subpicosecond time constants, and the last two have picosecond times. Shown is the percent error for each time constant with and without averaging over multiple population time windows.

the kinetic time constants. The need to average over shorter time intervals could therefore show the presence of interfering Stokes shift signals in experimental 2D measurements.

For all system types, the error in the time constant τ_{21} is smaller than τ_{31} and τ_{32}. (Tables 3.1-3.4). This result is due to a combination of two effects. The first is the relatively smaller number of kinetic pathways involving 2-1 energy transfer. For the 2 diagonal and 2-1 cross peak, there are no competing kinetic pathways that influence the signal. Conversely, exciton migration through both the exciton 3-2-1 pathway and the direct 3-1 pathway both cause the 3 diagonal to decrease and the 3-1 cross peak to increase with time. The competing pathways amplify small errors in the analysis because the τ_{31} and τ_{32} time constants because both τ_{31} and τ_{32} are fit simultaneously, as described above. The second effect is the approximation of the exciton 3 loss pathway (Figure 3.5, step 4). The τ_{3L} time constant is estimated as the short time constant of the diagonal. The loss rate constrains τ_{32} and τ_{31} because the sum $k_{32} + k_{31}$ must equal k_{3L}, but other Feynman pathways such as the ESA pathways and the ground state bleach recovery contribute to signal loss on the 3 diagonal. This approximation thus limits the possibility of reproducing the subtracted signal with complete accuracy. However, we have shown that the time constants are still fit within 15% accuracy despite these limitations.

τ_{2d} (fs)	τ_{d1} (fs)	τ_{21} (fs)	Error w/o average	Error w/ average	τ_{32} (fs)	Error w/o average	Error w/ average	τ_{31} (fs)	Error w/o average	Error w/ average
900	900	450	15.6%	17.5%	400	3.7%	3.4%	500	4.8%	3.4%
600	900	450	19.2%	23.7%	400	1.2%	0.5%	500	11.6%	7.5%
900	600	450	16.9%	18.0%	400	1.7%	1.0%	500	12.6%	9.6%
900	Inf	450	35.2%	34.9%	400	47.9%	41.7%	500	24.2%	22.9%

Table 3.2: Error in the time constant extraction method when a dark state is added between excitons 2 and 1. Here, τ_{2d} is the time constant for energy transfer from exciton 2 to the dark state, and τ_{d1} is the time for energy transfer from the dark state back to exciton 1. The percent error is calculated for each time constant with and without averaging over multiple population time windows.

τ_{3d} (fs)	τ_{d2} (fs)	τ_{21} (fs)	Error w/o average	Error w/ average	τ_{32} (fs)	Error w/o average	Error w/ average	τ_{31} (fs)	Error w/o average	Error w/ average
900	900	450	1.7%	1.3%	400	37.8%	34.3%	500	51.4%	23.3%
600	900	450	1.6%	1.3%	400	51.2%	45.7%	500	173%	49.1%
900	600	450	1.6%	1.3%	400	40.7%	36.4%	500	77.6%	34.0%
900	Inf	450	1.9%	1.6%	400	11.3%	13.5%	500	21.2%	20.6%

Table 3.3: Error in the time constant extraction method when a dark state is added between excitons 3 and 2 with the associated energy transfers given by τ_{3d} and τ_{d2}. (Same as Table 3.2 but with a different dark state.)

τ_{relax} (fs)	τ_{21} (fs)	Error w/o average	Error w/ average	τ_{32} (fs)	Error w/o average	Error w/ average	τ_{31} (fs)	Error w/o average	Error w/ average
5000	450	8.5%	4.9%	400	11.4%	10.3%	500	20.6%	3.59%
5000	800	5.52%	0.98%	400	4.4%	2.0%	500	33.0%	6.7%
5000	450	8.4%	3.05%	800	14.2%	7.0%	500	9.2%	7.6%
5000	450	8.70%	4.08%	400	22.5%	5.8%	800	2.1%	0.1%

Table 3.4: Error in the time constant method when resonant vibrations are added to excitons 1 and 2 that interfere with below diagonal cross peak signal kinetics. The vibrational relaxation times τ_{relax} are all 5000 fs. The percent error is also shown with and without averaging over population time windows. In this system, the averaging step (Figure 3.5, step 8) improves the accuracy for all energy transfer time constants.

3.5 Conclusion and Summary

We develop and characterize a method to accurately fit two-dimensional spectra to elementary kinetic rates for multistate energy transfer systems. We simulated two-dimensional spectra for standard multiexcitonic systems undergoing energy transfer, systems comprised of dark states that act as kinetic traps for energy transfer, and systems with resonant vibrations that undergo vibrational relaxation. The method remains accurate in the efficient energy transfer regime in two common limiting cases for excited state absorption pathways – weak and infinite biexciton coupling – and when the signals are convoluted by long-lived coherence and interfering vibrational relaxation pathways. When dark states are present the system, the fitting is accurate for energy transfer between states that are not adjacent to the dark state. Extracting accurate kinetic information from EET systems can provide information on the subtle microscopic parameters that influence and system and allow for precise comparative analyses between systems with slight differences, such as point mutations and functional group substitutions. As such, the method is widely applicable to excitonic systems undergoing downhill population transfer.

REFERENCES

[1] Minhaeng Cho, Harsha M. Vaswani, Tobias Brixner, Jens Stenger, and Graham R. Fleming. Exciton analysis in 2d electronic spectroscopy. *The Journal of Physical Chemistry B*, 109(21):10542–10556, 2005.

[2] S; Cho M Jeon, J; Park. *Two-dimensional Optical Spectroscopy: Theory and Experiment*. John Wiley Sons, 2010.

[3] Gregory D. Scholes, Graham R. Fleming, Lin X. Chen, Alán Aspuru-Guzik, Andreas Buchleitner, David F. Coker, Gregory S. Engel, Rienk van Grondelle, Akihito Ishizaki, David M. Jonas, Jeff S. Lundeen, James K. McCusker, Shaul Mukamel, Jennifer P. Ogilvie, Alexandra Olaya-Castro, Mark A. Ratner, Frank C. Spano, K. Birgitta Whaley, and Xiaoyang Zhu. Using coherence to enhance function in chemical and biophysical systems. *Nature*, 543(7647):647–656, 2017.

[4] Lili Wang, Marco A. Allodi, and Gregory S. Engel. Quantum coherences reveal excited-state dynamics in biophysical systems. *Nature Reviews Chemistry*, 3(8):477–490, 2019.

[5] Gitt Panitchayangkoon, Dugan Hayes, Kelly A. Fransted, Justin R. Caram, Elad Harel, Jianzhong Wen, Robert E. Blankenship, and Gregory S. Engel. Long-lived quantum coherence in photosynthetic complexes at physiological temperature. *Proceedings of the National Academy of Sciences*, 107(29):12766–12770, 2010.

[6] Jakub Dostál, Jakub Pšenčík, and Donatas Zigmantas. In situ mapping of the energy flow through the entire photosynthetic apparatus. *Nature Chemistry*, 8:705, 2016.

[7] Hong-Guang Duan, Valentyn I. Prokhorenko, Richard J. Cogdell, Khuram Ashraf, Amy L. Stevens, Michael Thorwart, and R. J. Dwayne Miller. Nature does not rely on long-lived electronic quantum coherence for photosynthetic energy transfer. *Proceedings of the National Academy of Sciences*, 114(32):8493–8498, 2017.

[8] Franklin D. Fuller, Jie Pan, Andrius Gelzinis, Vytautas Butkus, S. Seckin Senlik, Daniel E. Wilcox, Charles F. Yocum, Leonas Valkunas, Darius Abramavicius, and Jennifer P. Ogilvie. Vibronic coherence in oxygenic photosynthesis. *Nature Chemistry*, 6(8):706–711, 2014.

[9] Minjung Son, Alberta Pinnola, Roberto Bassi, and Gabriela S. Schlau-Cohen. The electronic structure of lutein 2 is optimized for light harvesting in plants. *Chem*, 5(3):575–584, 2019.

[10] Minjung Son, Alberta Pinnola, Samuel C. Gordon, Roberto Bassi, and Gabriela S. Schlau-Cohen. Observation of dissipative chlorophyll-to-carotenoid energy transfer in light-harvesting complex ii in membrane nanodiscs. *Nature Communications*, 11(1):1295, 2020.

[11] Tobias Brixner, Jens Stenger, Harsha M. Vaswani, Minhaeng Cho, Robert E. Blankenship, and Graham R. Fleming. Two-dimensional spectroscopy of electronic couplings in photosynthesis. *Nature*, 434(7033):625–628, 2005.

[12] Philip J. M. Johnson, Marwa H. Farag, Alexei Halpin, Takefumi Morizumi, Valentyn I. Prokhorenko, Jasper Knoester, Thomas L. C. Jansen, Oliver P. Ernst, and R. J. Dwayne Miller. The primary photochemistry of vision occurs at the molecular speed limit. *The Journal of Physical Chemistry B*, 121(16):4040–4047, 2017.

[13] Samer Gozem, Philip J. M. Johnson, Alexei Halpin, Hoi Ling Luk, Takefumi Morizumi, Valentyn I. Prokhorenko, Oliver P. Ernst, Massimo Olivucci, and R. J. Dwayne Miller. Excited-state vibronic dynamics of bacteriorhodopsin from two-dimensional electronic photon echo spectroscopy and multiconfigurational quantum chemistry. *The Journal of Physical Chemistry Letters*, 11(10):3889–3896, 2020.

[14] Lili Wang, Graham B. Griffin, Alice Zhang, Feng Zhai, Nicholas E. Williams, Richard F.

Jordan, and Gregory S. Engel. Controlling quantum-beating signals in 2d electronic spectra by packing synthetic heterodimers on single-walled carbon nanotubes. *Nature Chemistry*, 9(3):219–225, 2017.

[15] Sara H. Sohail, John P. Otto, Paul D. Cunningham, Young C. Kim, Ryan E. Wood, Marco A. Allodi, Jacob S. Higgins, Joseph S. Melinger, and Gregory S. Engel. Dna scaffold supports long-lived vibronic coherence in an indodicarbocyanine (cy5) dimer. *Chemical Science*, 11(32):8546–8557, 2020.

[16] Franz Milota, Valentyn I. Prokhorenko, Tomas Mancal, Hans von Berlepsch, Oliver Bixner, Harald F. Kauffmann, and Jürgen Hauer. Vibronic and vibrational coherences in two-dimensional electronic spectra of supramolecular j-aggregates. *The Journal of Physical Chemistry A*, 117(29):6007–6014, 2013.

[17] James Lim, David Paleček, Felipe Caycedo-Soler, Craig N. Lincoln, Javier Prior, Hans von Berlepsch, Susana F. Huelga, Martin B. Plenio, Donatas Zigmantas, and Jürgen Hauer. Vibronic origin of long-lived coherence in an artificial molecular light harvester. *Nature Communications*, 6(1):7755, 2015.

[18] Ryan E. Wood, Lawson T. Lloyd, Fauzia Mujid, Lili Wang, Marco A. Allodi, Hui Gao, Richard Mazuski, Po-Chieh Ting, Saien Xie, Jiwoong Park, and Gregory S. Engel. Evidence for the dominance of carrier-induced band gap renormalization over biexciton formation in cryogenic ultrafast experiments on mos2 monolayers. *The Journal of Physical Chemistry Letters*, 11(7):2658–2666, 2020. PMID: 32168454.

[19] Christopher L. Smallwood and Steven T. Cundiff. Multidimensional coherent spectroscopy of semiconductors. *Laser Photonics Reviews*, 12(12):1800171, 2018.

[20] Shaul Mukamel. *Principles of Nonlinear Optical Spectroscopy*. Oxford University Press, New York, 1995.

[21] Andrei Tokmakoff. *Time-dependent Quantum Mechanics and Spectroscopy, tdqms.uchicago.edu*. 2014.

[22] Sean T. Roberts, Joseph J. Loparo, and Andrei Tokmakoff. Characterization of spectral diffusion from two-dimensional line shapes. *The Journal of Chemical Physics*, 125(8):084502, 2006.

[23] Kyungwon Kwak, Sungnam Park, Ilya J. Finkelstein, and M. D. Fayer. Frequency-frequency correlation functions and apodization in two-dimensional infrared vibrational echo spectroscopy: A new approach. *The Journal of Chemical Physics*, 127(12):124503, 2007.

[24] Emily E. Fenn and M. D. Fayer. Extracting 2d ir frequency-frequency correlation functions from two component systems. *The Journal of Chemical Physics*, 135(7):074502, 2011.

[25] Marco A. Allodi, John P. Otto, Sara H. Sohail, Rafael G. Saer, Ryan E. Wood, Brian S. Rolczynski, Sara C. Massey, Po-Chieh Ting, Robert E. Blankenship, and Gregory S. Engel. Redox conditions affect ultrafast exciton transport in photosynthetic pigment–protein complexes. *The Journal of Physical Chemistry Letters*, 9(1):89–95, 2018.

[26] Erling Thyrhaug, Karel Žídek, Jakub Dostál, David Bína, and Donatas Zigmantas. Exciton structure and energy transfer in the fenna–matthews–olson complex. *The Journal of Physical Chemistry Letters*, 7(9):1653–1660, 2016.

[27] Jakub Dostál, Barbora Benešová, and Tobias Brixner. Two-dimensional electronic spectroscopy can fully characterize the population transfer in molecular systems. *The Journal of Chemical Physics*, 145(12):124312, 2016.

[28] P. Hamm and M. T. Zanni. *Concepts and methods of 2D Infrared Spectroscopy*. Cambridge UP, 2011.

[29] Robert Silbey. Description of quantum effects in the condensed phase. *Procedia Chemistry*, 3(1):188–197, 2011.

[30] Karthik Gururangan and Elad Harel. Coherent and dissipative quantum process tensor reconstructions in two-dimensional electronic spectroscopy. *The Journal of Chemical Physics*, 150(16):164127, 2019.

[31] Andrea Volpato, Luca Bolzonello, Elena Meneghin, and Elisabetta Collini. Global analysis of coherence and population dynamics in 2d electronic spectroscopy. *Opt. Express*, 24(21):24773–24785, Oct 2016.

[32] Jacob S. Higgins, Lawson T. Lloyd, Sara H. Sohail, Marco A. Allodi, John P. Otto, Rafael G. Saer, Ryan E. Wood, Sara C. Massey, Po-Chieh Ting, Robert E. Blankenship, and Gregory S. Engel. Photosynthesis tunes quantum mechanical mixing of electronic and vibrational states to steer exciton energy transfer. *Proceedings of the National Academy of Sciences*, 2021.

[33] Robert Boyd. *Nonlinear Optics*. Academic Press, 3rd edition, 2008.

[34] Bernard; Laloe Frank Cohen-Tannoudji, Claude; Diu. *Quantum Mechanics*. Wiley, 1 edition, 1991.

[35] Mino Yang and Graham R. Fleming. Third-order nonlinear optical response of energy transfer systems. *The Journal of Chemical Physics*, 111(1):27–39, 1999.

[36] Richard D. Mattuck. *A Guide to Feynman Diagrams in the Many-Body Problem*. Dover Publications, 2nd edition, 1992.

[37] Dario Polli, Piero Altoè, Oliver Weingart, Katelyn M. Spillane, Cristian Manzoni, Daniele Brida, Gaia Tomasello, Giorgio Orlandi, Philipp Kukura, Richard A. Mathies, Marco Garavelli, and Giulio Cerullo. Conical intersection dynamics of the primary photoisomerization event in vision. *Nature*, 467(7314):440–443, 2010.

[38] Michael D. Harris, Daniel C.; Bertolucci. *Symmetry and Spectroscopy: An Introduction to Vibrational and Electronic Spectroscopy*. Oxford University Press, Inc., New York, 1978.

[39] Sara H. Sohail, Peter D. Dahlberg, Marco A. Allodi, Sara C. Massey, Po-Chieh Ting, Elizabeth C. Martin, C. Neil Hunter, and Gregory S. Engel. Communication: Broad manifold of excitonic states in light-harvesting complex 1 promotes efficient unidirectional energy transfer in vivo. *The Journal of Chemical Physics*, 147(13):131101, 2017.

[40] Peter D. Dahlberg, Po-Chieh Ting, Sara C. Massey, Marco A. Allodi, Elizabeth C. Martin, C. Neil Hunter, and Gregory S. Engel. Mapping the ultrafast flow of harvested solar energy in living photosynthetic cells. *Nature Communications*, 8(1):988, 2017.

[41] Jacob S. Higgins, William R. Hollingsworth, Lawson T. Lloyd, and Gregory S. Engel. *Quantum Coherence in Chemical and Photobiological Systems*, volume 1398 of *ACS Symposium Series*, book section 18, pages 411–436. American Chemical Society, 2021.

[42] Niklas Christensson, Harald F. Kauffmann, Tõnu Pullerits, and Tomáš Mančal. Origin of long-lived coherences in light-harvesting complexes. *Journal of Physical Chemistry B*, 116(25):7449–7454, 2012.

[43] Shu-Hao Yeh, Ross D. Hoehn, Marco A. Allodi, Gregory S. Engel, and Sabre Kais. Elucidation of near-resonance vibronic coherence lifetimes by nonadiabatic electronic-vibrational state character mixing. *Proceedings of the National Academy of Sciences*, 116(37):18263, 2019.

[44] G. S. Engel, T. R. Calhoun, E. L. Read, T. K. Ahn, T. Mancal, Y. C. Cheng, R. E. Blankenship, and G. R. Fleming. Evidence for wavelike energy transfer through quantum coherence in photosynthetic systems. *Nature*, 446(7137):782–6, 2007.

[45] Margherita Maiuri, Evgeny E. Ostroumov, Rafael G. Saer, Robert E. Blankenship, and Gregory D. Scholes. Coherent wavepackets in the fenna–matthews–olson complex are robust to excitonic-structure perturbations caused by mutagenesis. *Nature Chemistry*, 10:177, 2018.

[46] Jacob S. Higgins, Marco A. Allodi, Lawson T. Lloyd, John P. Otto, Sara H. Sohail, Rafael G. Saer, Ryan E. Wood, Sara C. Massey, Po-Chieh Ting, Robert E. Blankenship, and Gregory S. Engel. Redox conditions correlated with vibronic coupling modulate quantum beats in photosynthetic pigment–protein complexes. *Proceedings of the National Academy of Sciences*, 118(49):e2112817118, 2021.

[47] Tihana Mirkovic, Evgeny E. Ostroumov, Jessica M. Anna, Rienk van Grondelle, Govindjee, and Gregory D. Scholes. Light absorption and energy transfer in the antenna complexes of photosynthetic organisms. *Chemical Reviews*, 117(2):249–293, 2017.

[48] Vladimir I. Novoderezhkin and Rienk van Grondelle. Physical origins and models of energy transfer in photosynthetic light-harvesting. *Physical Chemistry Chemical Physics*, 12(27):7352–7365, 2010.

CHAPTER 4

PHOTOSYNTHESIS TUNES QUANTUM MECHANICAL MIXING OF ELECTRONIC AND VIBRATIONAL STATES TO STEER EXCITON ENERGY TRANSFER

The work presented in this Chapter has been published and adapted with permission from: J.S. Higgins, L.T. Lloyd, S.H. Sohail, M.A. Allodi, J.P. Otto, R.G. Saer, R.E. Wood, S.C. Massey, P-C. Ting, R.E. Blankenship, and G.S. Engel, "Photosynthesis Tunes Quantum Mechanical Mixing of Electronic and Vibrational States to Steer Exciton Energy Transfer," *PNAS* 118, e2018240118 2021.[1]

Photosynthetic species evolved to protect their light-harvesting apparatus from photoxidative damage driven by intracellular redox conditions or environmental conditions [1, 2]. The Fenna-Matthews-Olson (FMO) pigment-protein complex from green sulfur bacteria exhibits redox-dependent quenching behavior partially due to two internal cysteine residues [3]. Here, we show evidence that a photosynthetic complex exploits the quantum mechanics of vibronic mixing to activate an oxidative photoprotective mechanism. We use two-dimensional electronic spectroscopy (2DES) to capture energy transfer dynamics in wild-type and cysteine-deficient FMO mutant proteins under both reducing and oxidizing conditions. Under reducing conditions, we find equal energy transfer through the exciton 4-1 and 4-2-1 pathways because the exciton 4-1 energy gap is vibronically coupled with a bacteriochlorophyll-a vibrational mode. Under oxidizing conditions, however, the resonance of the exciton 4-1 energy gap is detuned from the vibrational mode, causing excitons to preferentially steer through the indirect 4-2-1 pathway to increase the likelihood of exciton

1. Thank you to Prof. Robert Blankenship and Dr. Rafael Saer for providing the biological samples, to Dr. Karen Watters for scientific editing of the manuscript, to Prof. Ryszard Jankowiak and Dr. Adam Kell for detailed insight into their Redfield Model "C" and guidance for implementation of the model, and to Dr. Jonathan Fetherolf for detailed discussions.

quenching. We use a Redfield model to show that the complex achieves this effect by tuning the site III energy via the redox state of its internal cysteine residues. This result shows how pigment-protein complexes exploit the quantum mechanics of vibronic coupling to steer energy transfer.

4.1 Significance of Redox-Dependent Vibronic Coupling

Photosynthetic light harvesting antennae transfer energy toward reaction centers with high efficiency, but in high light or oxidative environments, the antennae divert energy to protect the photosynthetic apparatus. For a decade, quantum effects driven by vibronic coupling, where electronic and vibrational states couple, have been suggested to explain the energy transfer efficiency, but questions remain whether quantum effects are merely consequences of molecular systems. Here, we show evidence that biology tunes inter-pigment vibronic coupling, indicating that the quantum mechanism is operative in the efficient transfer regime and exploited by evolution for photoprotection. Specifically, the FMO complex uses redox-active cysteine residues to tune the resonance between its excitons and a pigment vibration to steer excess excitation toward a quenching site.

4.2 Introduction to Redox Conditions in Photosynthesis

Photosynthetic organisms convert solar photons into chemical energy by taking advantage of the quantum mechanical nature of their molecular systems and the chemistry of their environment[1, 4, 5, 6]. Antenna complexes, composed of one or more pigment-protein complexes, facilitate the first steps in the photosynthesis process: They absorb photons and determine which proportion of excitations to move to reaction centers, where charge separation occurs[6]. In oxic environments, excitations can generate highly reactive singlet oxygen species. These pigment-protein complexes can quench excess excitations in these

environments with molecular moieties such as quinones and cysteine residues[1, 7, 8].

The FMO complex, a trimer of pigment-protein complexes found in the green sulfur bacterium *Chlorobaculum tepidum* [9], has emerged as a model system to study the photophysical properties of photosynthetic antenna complexes[3, 10, 11, 12, 13, 14, 15, 16, 17, 18, 19]. Each subunit in the FMO complex contains eight bacteriochlorophyll-a site molecules (PDB: 3ENI) that are coupled to form a basis of eight partially-delocalized excited states called excitons (Figure 4.1) [20, 21, 22, 23]. Previous experiments on FMO have observed the presence of long-lived coherences in nonlinear spectroscopic signals at both cryogenic and physiological temperatures[11, 13]. The coherent signals are thought to arise from some combination of electronic[24, 25, 26], vibrational[16, 17, 18], and vibronic[27] coherences in the system[28, 29, 30]. One previous study reported that the coherent signals in FMO remain unchanged upon mutagenesis of the protein, suggesting that the signals are ground state vibrational coherences[17]. Others discuss the role of vibronic coupling, where electronic and nuclear degrees of freedom become coupled[29]. Other dimeric model systems have demonstrated the regimes in which these vibronically coupled states produce coherent or incoherent transport and vibronic coherences[31, 32, 33]. Recent spectroscopic data has suggested that vibronic coupling plays a role in driving efficient energy transfer through photosynthetic complexes[27, 31, 33, 34], but to date there is no direct experimental evidence suggesting that biological systems use vibronic coupling as part of their biological function.

It has been shown that redox conditions affect excited state properties in pigment-protein complexes, yet little is known about the underlying microscopic mechanisms for these effects[1, 3]. Many commonly studied light-harvesting complexes, including the FMO complex[20], light-harvesting complex 2 (LH2)[35], the PC645 phycobiliprotein[36], and the cyanobacterial antenna complex isiA[37], contain redox-active cysteine residues in close proximity to their chromophores. As the natural low light environment of *C. tepidum* does not necessitate photoprotective responses to light quantity and quality, its primary photoprotec-

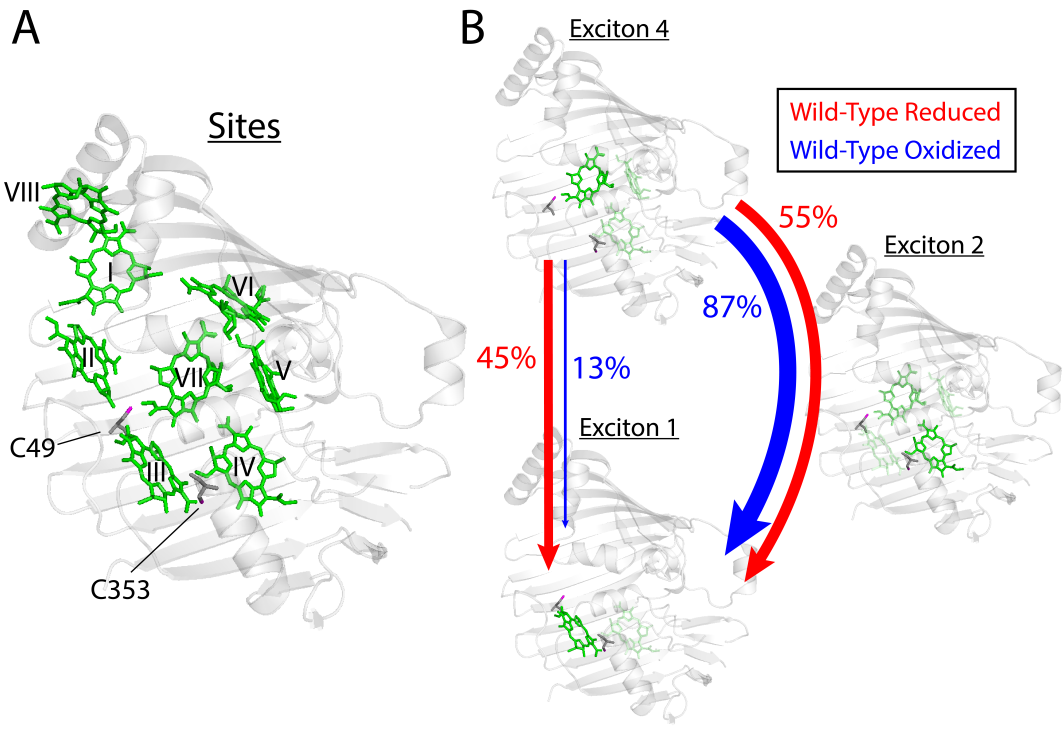

Figure 4.1: A) Numbered sites and side chains of cysteines C353 and C49 in the FMO pigment-protein complex (PDB: 3ENI)[20]. B) Site densities for excitons 4, 2, and 1 in reducing conditions with the energy transfer branching ratios for the wild-type oxidized and reduced protein. The saturation of pigments in each exciton denotes the relative contribution number to the exciton. The C353 residue is located near excitons 4 and 2, which have most electron density along one side of the complex, and other redox active residues such as the Trp/Tyr chain. C353 and C49 surround site III, which contains the majority of exciton 1 density. Excitons 2 and 4 are generally delocalized over sites IV, V, and VII.

tive mechanism concerns its response to oxidative stress. *C. tepidum* is an obligate anaerobe, but the presence of many active anoxygenic genes such as *sodB* for superoxide dismutase and *roo* for rubredoxin oxygen oxidoreductase [38] suggests that it is frequently exposed to molecular oxygen[8, 39]. Using time-resolved fluorescence measurements, Orf *et al.* demonstrated that two cysteine residues in the FMO complex, C49 and C353, quench excitons under oxidizing conditions[1], which could protect the excitation from generating reactive oxygen species[8, 40, 41, 42]. In two-dimensional electronic spectroscopy (2DES) experiments, Allodi *et al.* showed that redox conditions in both the wild-type and C49A/C353A double mutant proteins affect the ultrafast dynamics through the FMO complex[3, 43]. The recent discovery that many proteins across the evolutionary landscape possess chains of tryptophan and tyrosine residues provides evidence that these redox-active residues may link the internal protein behavior with the chemistry of the surrounding environment[41, 43].

In this paper, we present data showing that pigment-protein complexes tune the vibronic coupling of their chromophores and that the absence of this vibronic coupling activates an oxidative photoprotective mechanism. We use 2DES to show that a pair of cysteine residues in FMO, C49 and C353, can steer excitations toward quenching sites in oxic environments. The measured reaction rate constants demonstrate unusual non-monotonic behavior. We then use a Redfield model to determine how the EET time constants arise from changing chlorophyll site energies and their system-bath couplings[44, 45]. The analysis reveals that the cysteine residues tune the resonance between exciton 4-1 energy gap and an intramolecular chlorophyll vibration in reducing conditions to induce vibronic coupling and detune the resonance in oxidizing conditions. This redox-dependent modulation of the vibronic coupling steers excitations through different pathways in the complex to change the likelihood that they interact with exciton quenchers.

4.3 Redox-Dependent Exciton Steering by Cysteine Residues

We investigate the excitonic pathways that give rise to the different 2DES signals to determine the roles of the cysteine C353 and C49 residues in exciton energy transfer. Two-dimensional electronic spectra map the couplings between excitonic states and show how the couplings evolve over time. The excitation energy (x-axis) of the system is correlated with the detection energy (y-axis) at each waiting time delay T. We can plot the intensity of peaks in the spectra with increased waiting time to observe the kinetic evolution of the exciton populations. For example, a cross peak below the diagonal can report on energy absorbed at a higher energy state and detected at a lower energy state, indicating energy transfer between these states. Figure 4.2 shows 2DES spectra for the FMO wild-type, C353A and C49A single mutants, and C353A/C49A double mutant samples under both oxidizing and reducing conditions at waiting time T=1 ps. At later waiting times, the growth of below diagonal cross peaks, where the excitation energy is greater than the detection energy, indicates that there is downhill EET in the system at sub-picosecond rates. Using averaged time traces for each of these spectra, we extracted the EET time constants for exciton 4-1, 4-2, and 2-1 energy transfer in each sample (see previous chapter).

Experimental time constant data in Table 4.1 show that the redox environment determines which pathways the excitation energy takes through the complex. Looking first at wild-type FMO under reducing conditions, we see that τ_{41}, τ_{42} and τ_{21} are comparable at 504 $\pm$ 12 fs, 408 $\pm$ 12 fs, and 455 $\pm$ 11 fs, respectively, indicating that exciton 4 is equally likely to transfer energy to exciton 1 through the direct 4-1 or indirect 4-2-1 pathways. The branching ratios representing relative probability of EET for these two pathways are 0.45 and 0.55, respectively[46]. When the wild-type FMO is oxidized, τ_{41} gets slower (1.5 ps), τ_{42} gets faster (227 fs), and τ_{21} does not change, indicating that exciton 4 is more likely to transfer energy through the indirect pathway under oxidizing conditions. Under these conditions, the branching ratios for the direct versus indirect pathway become 0.13 and 0.87, respectively.

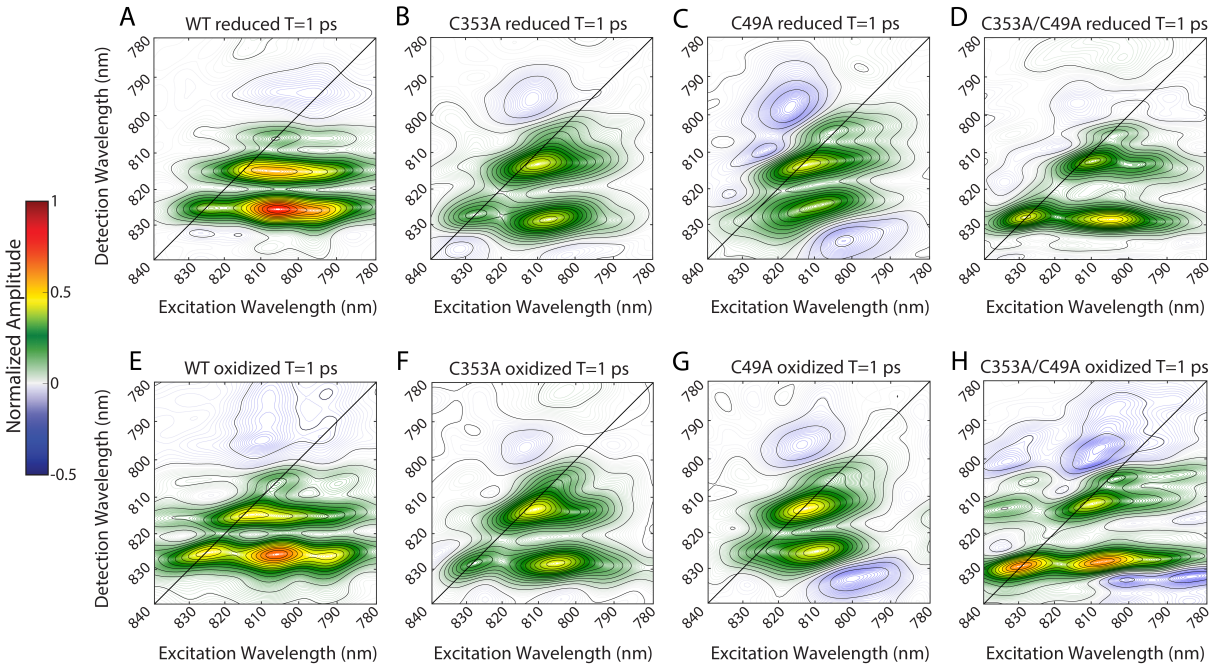

Figure 4.2: Absorptive 2D spectra of the eight FMO samples at waiting time T=1 ps under reducing (top row, A-D) and oxidizing (bottom row, E-H) conditions. In 2DES, the excitation energy of a system is correlated with the detection energy, and the waiting time T indicates the delay time between the pump and probe pulses. Spectra were normalized to the peak amplitude at time T=0. The three peaks of the diagonal features in each spectrum represent excitons 4, 2, and 1. The growth of cross peaks below the diagonal indicates downhill EET on the timescale of hundreds of femtoseconds.

Experiment			
	τ_{21} (fs)	τ_{41} (fs)	τ_{42} (fs)
WT reduced	**455 ± 11**	**504 ± 12**	**408 ± 12**
C353A reduced	544 ± 15	>5000	204 ± 20
C49A reduced	485 ± 13	558 ± 25	537 ± 25
C353A/C49A reduced	567 ± 20	>5000	205 ± 24
WT oxidized	**439 ± 10**	**1480 ± 11**	**227 ± 11**
C353A oxidized	438 ± 11	853 ± 14	328 ± 14
C49A oxidized	452 ± 9	520 ± 19	524 ± 19
C353A/C49A oxidized	594 ± 17	1642 ± 21	301 ± 21

Table 4.1: Experimental energy transfer time constants for wild-type (WT), singly mutated, and doubly mutated FMO samples under reducing and oxidizing conditions extracted from two-dimensional spectra using the method detailed in the previous chapter.

In the 4-2-1 pathway, the excitation is steered to generate higher electron density near the periphery of the system (exciton 2, Figure 4.1). The amino acids near this region contain, among other redox-active residues, a Trp-Tyr chain which has been suggested to play a role in the redox-dependent ultrafast dynamics of the FMO complex[3]. Given that τ_{21} does not change, steering the excitation through the 4-2-1 pathway under oxidizing conditions would increase the likelihood of quenching at the cysteine 353 trapping site or charge transfer to the Trp-Tyr chain [43]. As shown in previous work [1, 3], we see that the long time signal amplitudes of the oxidized wild-type complex decay faster than those of the reduced wild-type complex. The signal amplitudes of the oxidized wild-type complex also decay faster than those of the C353A/C49A double mutant samples, which decay at similar rates under both redox conditions, indicating that the cysteines are responsible for the observed quenching.

Overall, we find that the C353 residue is responsible for exciton steering in reducing conditions, based on the drastic change in time constants in the C353A mutants in reducing conditions. However, we find that both C49 and C353 are active in oxidizing conditions. We observe that the patterns in the time constants are non-monotonic and, in oxidizing conditions, non-cooperative, as one would expect. A detailed analysis of all single and double mutant EET time constants can be found in the supplementary sections.

4.4 Redfield Model Reveals Vibronic Coupling Mechanism for Controlling Energy Transfer

To understand the complex, non-monotonic changes in the time constants for energy transfer as a function of both redox environment and mutation, we employ a Redfield model to show that the FMO protein structure facilitates redox-dependent exciton steering by tuning its resonant coupling with a vibrational mode in bacteriochlorophyll-*a*. The Redfield equation describes the relaxation of an exciton through the excited states of the complex after second order perturbation by the system-bath coupling. The rate of energy transfer increases with the spatial overlap of excitons, resonance between the excitonic energy gap and bath oscillations through the spectral density, and the magnitude of coupling between the system and these bath modes (Huang-Rhys factor) [47, 48]. An increased Huang-Rhys factor indicates that there is greater system-bath coupling, meaning that the bath more strongly couples to the excitonic states, and increases the rate of EET [47]. We varied the pigment site energies and Huang-Rhys factors for bacteriochlorophyll-*a* sites II, III, and IV. These sites are proximal (within 10 angstroms) to C353 and C49 and are most likely to be electrostatically perturbed by cysteine mutation and oxidation [20]. We use a log-normal spectral density with an added Gaussian curve centered at 260 cm^{-1} representing coupling to a vibrational mode in bacteriochlorophyll-*a* [44, 45]. The most illustrative energy transfer dynamics maps were for sites III and IV, shown in Figure 4.3B-D. In the maps, the x-axis represents the relative change in Huang-Rhys factor for a given site, the y-axis represents the change in site energy, the colormap represents the value of the energy transfer time constant as a function of these two variables, and the arrows represent changes upon mutation. Our results represent the only consistent set of changes that reproduce the experimental data. The calculated EET time constants can be found in Table 4.2. For example, in Figure 4.3B the dashed blue line pointing downward from 'WT oxidized' to 'oC49A' shows that under oxidizing conditions, mutation of the C49 residue lowers the site III energy by 100 cm^{-1} but

Redfield Theory									
	Site II change (cm^{-1})	Site III change (cm^{-1})	Site IV change (cm^{-1})	Spectral Density Site II change (S/S_0)	Spectral Density Site III change (S/S_0)	Spectral Density Site IV change (S/S_0)	τ_{21} (fs)	τ_{41} (fs)	τ_{42} (fs)
WT reduced	**0**	**0**	**0**	**1**	**1**	**1**	**508**	**499**	**437**
C353A reduced	0	-60	10	1	0.8	1.1	537	1601	397
C49A reduced	20	0	0	1	1	1	504	535	476
C353A/C49A reduced	20	-60	10	1	0.8	1.1	525	1884	427
WT oxidized	**40**	**120**	**70**	**1**	**1**	**1**	**264**	**1532**	**412**
C353A oxidized	40	60	40	1	0.8	1.2	395	725	398
C49A oxidized	20	20	10	1	1	1	455	504	443
C353A/C49A oxidized	20	-40	-20	1	0.8	1.2	534	988	509

Table 4.2: Calculated changes made to the FMO Hamiltonian to reproduce the general trends in spectroscopic data. The time constants were calculated using the 'Model C' Redfield model described in the text. The trends in the time constants are mapped visually in Figure 4.3.

does not affect the Huang-Rhys factor, in agreement with the difference in the corresponding experimental time constant in Table 4.1.

Our Redfield model reveals that the FMO protein structure modulates different energy transfer rates by tuning its resonant coupling with the vibrational mode centered at 260 cm^{-1}. Figure 4.3A-B shows that when oxidized or reduced FMO is perturbed by mutation, the energy of site III changes such that the distribution of the exciton 4-1 energy gaps shifts in its resonance with the chlorophyll vibration. When site III energy is raised in this FMO Hamiltonian, the exciton 4-1 energy gap decreases. In the wild-type reduced Hamiltonian, the vibronic coupling between the energy gap distribution and the chlorophyll vibration produces a subpicosecond τ_{41} time constant[23]. The oxidized wild-type protein has a 120 cm^{-1} increase in site III energy relative to the reduced wild-type; the slower time constant reflects the fact that the 4-1 energy gap is detuned from the chlorophyll mode (Figure 4.2A-B). In both oxidizing and reducing conditions, we find that the changes to the system Hamiltonian actually represent cooperative effects between mutations, meaning that the changes to the double mutant are a combination of the changes to the two single mutants

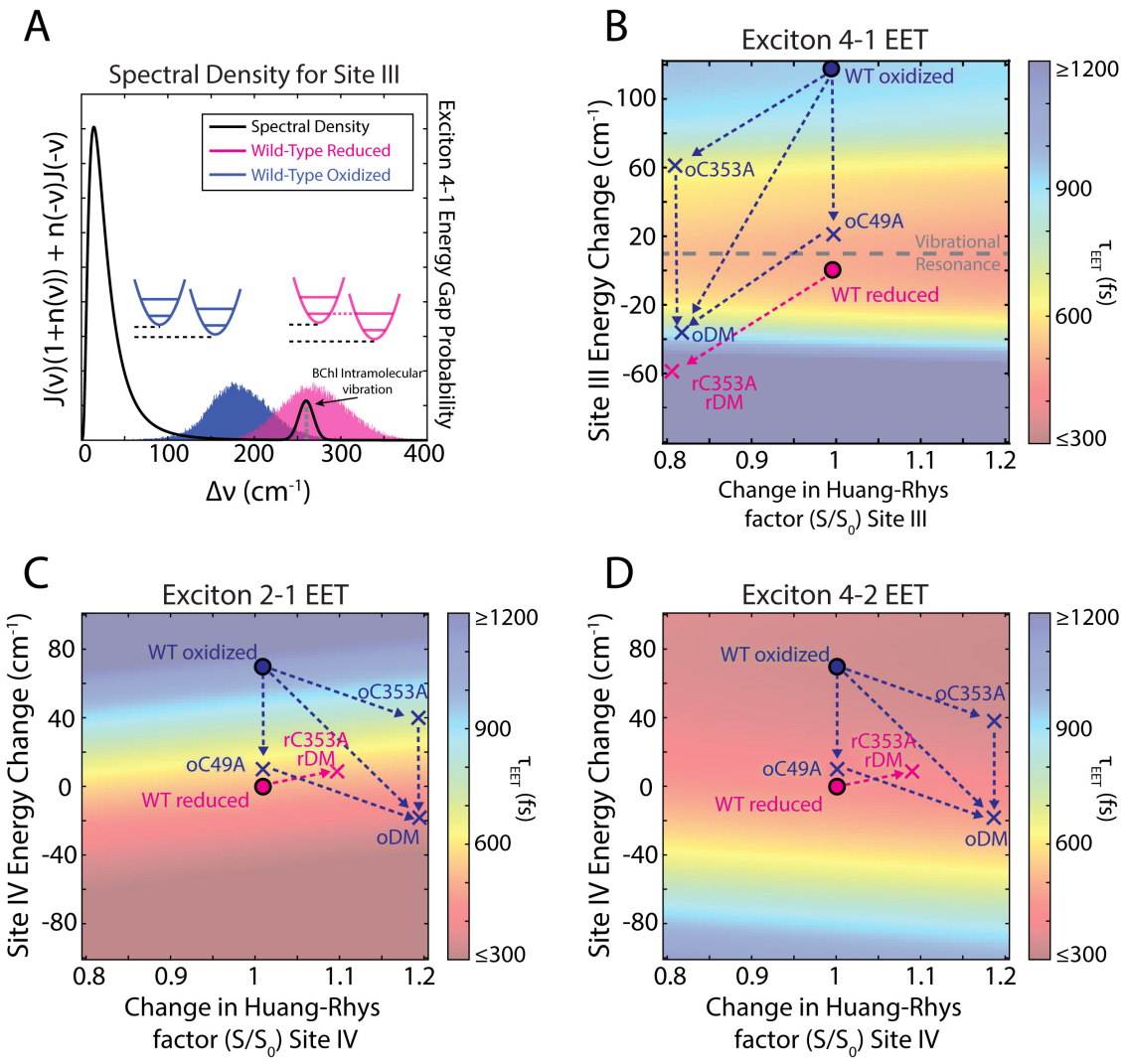

Figure 4.3: Calculated Redfield energy transfer rates of the FMO Hamiltonian upon changing the site energies and degree of system-bath coupling (Huang-Rhys factors, S) for pigments III (A-B) and IV (C-D). The center points (S/S_0=1; site energy change $\Delta\nu$=0 cm^{-1}; plotted as red circle) represent the wild-type FMO in reducing conditions. The blue circles represent wild-type FMO in oxidizing conditions. A) Overlap of the distribution of exciton 4-1 energy gaps in FMO with the spectral density for site III, representing relative vibronic coupling with an intramolecular vibration. Increased overlap with the spectral density indicates that the bath can more readily couple the two excitons, which increases the EET rate. B) Change in the τ_{41} time constant as site III energy and Huang-Rhys factor is changed. C-D) Change in the τ_{21} and τ_{42} time constants as site IV is changed. The arrows represent how mutation changes each FMO sample. The 'o' and 'r' prefixes represent the oxidized and reduced parameters, respectively. For the reduced FMO samples, there is no change in the C49A parameters, and the C353A changes are the same as the double mutant (DM) changes. In every case, the double mutant is a sum of the two single mutant vectors. The calculated changes are shown in Table 4.2.

(Table 4.2).

Generally, the effect of oxidation raises the site III energy based on the number of unmutated cysteines present, while the effect of mutation lowers the site III energy (Table 4.2). Our experimental data showed that τ_{41} slowed down significantly (>5 ps) when the C353 residue was mutated under reducing conditions, discussed above. In the Redfield model, this change is least perturbatively achieved by lowering the energy of site III by >50 cm^{-1}, which increases the 4-1 energy gap and diminishes the vibronic coupling with the chlorophyll mode, as shown by the arrows representing site mutation in Figure 4.3B. The reduced C49A time constants are relatively less changed, so we assume that the site energies for this mutant are roughly equal to the wild-type reduced parameters. The changes in the reduced double mutant C49A/C353A parameters are thus exclusively caused by the C353A mutation.

In the oxidized samples, mutating C353 or C49 subsequently lowers the site III energy such that the vibronic resonance with the bacteriochlorophyll-a mode is increased in each single mutant and is decreased cooperatively in the double mutant. In Figure 4.3B, we see that the calculated τ_{41} time constants in the oxidized single mutants are faster than the double mutant because each single mutant is passing through the resonance vibronic coupling region. These changes to site III upon mutation of the oxidized cysteine residues shift the exciton 4-1 energy gap through various magnitudes of vibronic coupling with the intrinsic chlorophyll mode to facilitate steering of energy transfer pathways.

In the reduced FMO complex, the resonance between the 4-1 energy gap and the spectral density demonstrates that the chlorophyll vibration is able to couple the excitonic states and facilitate energy transfer. The cysteine residues manipulate the electronic Hamiltonian of FMO by tuning the degree of vibronic coupling between the exciton 4-1 energy gap and the intramolecular vibration centered at 260 cm^{-1}. The resulting assignments of site changes to the FMO Hamiltonian are supported within the limitations of Redfield theory because the mutations and redox-conditions primarily perturb the excitonic Hamiltonian, not the system-

bath coupling, as evident from the changes in peak position of the linear absorption spectra. In this new mechanism, the system steers the excited-state energy transfer toward quenching sites near the protein periphery in response to potentially dangerous oxic conditons.

4.5 Discussion: Exciton Steering by Vibronic Tuning

In this study, we show that redox-active residues in FMO steer energy transfer through different pathways in the complex by tuning the excitonic energy in and out of resonance with a vibrational mode of the pigments. In the oxidized wild-type protein and the reduced mutated C353A and C353A/C49A proteins, the vibronic coupling is detuned because the site III energy is changed, causing the exciton 4-1 energy gap to shift out of resonant coupling with an intramolecular vibration in the bacteriochlorophyll molecule. In these conditions, the indirect exciton 4-2-1 energy transfer pathway becomes more kinetically favorable than the direct exciton 4-1 pathway, increasing the likelihood of interacting with quenching sites in the protein. The redox-dependent vibronic coupling shown here exemplifies an evolutionary mechanism by which photosynthetic organisms can exploit the quantum mixing between electronic and vibrational states to control excited state energy transfer dynamics.

4.6 Materials and Methods

4.6.1 Experimental Parameters

Two-dimensional spectra of wild-type, C353A, C49A, and C535A/C49A FMO under oxidizing and reducing conditions were acquired at 77 K, as described in detail in a previous publication[3]. Briefly, we used a cryostat containing liquid nitrogen (Oxford Instruments) to cool the sample to 77K. To generate a glass, we mixed the protein buffer (CAPS, pH 10.5) with 50% glycerol and loaded the solution into a 200 μm quartz cuvette (Starna) coated with SigmaCote. We generated 'oxidizing' conditions by handling the sample in ambient air prior

to cooling. To create 'reducing' conditions, we added sodium dithionite to a concentration of 10 mM.

For the spectroscopic measurements, using the output of a regenerative amplifier (Coherent Inc. Legend Elite USP, 35 fs, centered at 800 nm), we generated coherent light spanning from 775 to 840 nm via self-phase modulation in 15 psi of argon. The pulse was then temporally compressed to less than 20 fs using a pulse shaper (Biophotonic Solutions, MIIPS). We acquired 25 2DES spectra for each sample using our single-shot, GRadient Assisted Photon Echo Spectroscopy (GRAPES) setup, described in detail elsewhere[49, 50, 51, 52]. We also collected pump-probe spectra of each sample to phase the data using the projection-slice theorem. We phased each spectrum separately and then averaged them to produce an averaged fully absorptive signal.

4.6.2 Extraction of Kinetic Parameters

To obtain the time constants τ_{21}, τ_{42}, and τ_{41} for each FMO sample, we averaged over the diagonal and below diagonal cross peak signals using a circular window with a 70 cm^{-1} range. The center points of the circles for each exciton pair were taken from the peaks of the respective linear absorption spectrum. The signals were then normalized, and the normalized diagonal signals were subtracted from the normalized cross peak signals to remove the bleach recovery contribution. The subtracted signals were then fit to phenomenological kinetic equations for energy transfer. The time constant τ_{21} was fit with the 2 diagonal and 2-1 cross peak, and the τ_{41} and τ_{42} time constants were fit with the 4 diagonal and 4-1 cross peak using the 4 diagonal time constant as a fit constraint.

4.6.3 Redfield Energy Transfer Calculations

We calculated the Redfield energy transfer rates resulting from changing the FMO Hamiltonian. We used the 'Model C' FMO Redfield model developed by Kell et al. 2016 (Ref [45])

and their most recent FMO Hamiltonian as listed in Ref [23]. Calculated rates using uncorrelated sites were averaged over static disorder with 5,000 Hamiltonians for each site using the same disorder parameters, Huang-Rhys factors, variances, and bath cutoff frequencies as listed in Ref [45]. We added a Gaussian line centered at 260 cm^{-1} with a FWHM of 20 cm^{-1} to the spectral density of each site. We calculate the energy rates after varying the site energies and Huang-Rhys factors for sites II, III, and IV. We fit to the set of changes for each FMO sample and constrained the set such that mutation and oxidation are consistent for all FMO samples.

4.7 Supporting Material: Exciton Steering by Individual Cysteine Residues

Reduced C49A mutant kinetics are similar to those of the reduced wild-type, which implies that C49 does not play a role in energy transfer when reduced. However, mutation of C353 singly or in the double mutant C353A/C49A under reducing conditions (Table 4.1) also redirects energy transfer to the 4-2-1 pathway. In both C353A and C353A/C49A, τ_{41} slows down (from 504 fs to >5 ps) while τ_{42} becomes faster (from 408 fs to 204 fs). The time constant τ_{21} also slows down (from 455 fs to 544 fs) although the difference in transfer rate between wild-type and mutants is much less pronounced, and we note that the slower τ_{21} in the mutant C353A sample does not directly affect the propensity of exciton 4 to be steered through either the direct or indirect pathway. Due to significantly slower τ_{41} time constants in the C353A and C353A/C49A samples, the relative probability of an exciton moving through the 4-2-1 pathway is significantly increased. The unfavorable kinetics of the direct 4-1 pathway in the reduced C353A sample provides evidence that the C353 residue plays an active role in steering through the 4-1 pathway in FMO under reducing conditions.

In the oxidized FMO complex, the time constant data show that both C353 and C49 residues steer excitations through the direct 4-1 or the indirect 4-2-1 pathways. As discussed

in a previous section, when wild-type FMO is oxidized, τ_{41} slows down (1.5 ps) and τ_{42} speeds up (227 fs) as energy transfer is steered through the 4-2-1 pathway. When C353 or C49 are individually mutated under oxidizing conditions the time constant values approach the wild-type reduced values: τ_{41} gets faster (853 fs and 520 fs for C353A and C49A respectively), τ_{42} gets slower (328 fs and 524 fs, respectively), and τ_{21} once again exhibits little change. These τ_{41} and τ_{42} results for the individual mutant samples indicate that C353 and C49 cysteine residues are both involved in steering through the 4-1 and 4-2-1 pathways under oxidizing conditions. Additionally, the C353A time constants change significantly between reducing and oxidizing conditions, which further suggests that the C49 residue, which is present in this mutant, becomes activated when oxidized and plays a large role in the excitonic steering in ambient conditions.

Based on these results, we might expect to observe a cooperative effect in the oxidized double mutant C353A/C49A. However, in the oxidized double mutant, τ_{41} essentially returns to the oxidized wild-type time constant value. Further, it appears that redox-active residues other than C353 and C49 are involved in steering excitations. For example, the τ_{41} time constant in the oxidized double mutant (1642 fs), while comparable to the oxidized wild-type (1480 fs), is still much faster than τ_{41} in the reduced double mutant (>5 ps). Oxidation therefore likely affects exciton dynamics through other redox-active residues besides C49 and C353 in the complex.

It has been previously shown that C353 is the more active quenching residue in oxidized FMO on longer timescales [1]. C353 is located in the center of the electron density for excitons 1, 2, and 4, whereas C49 is near exciton 1 but not the bulk of electron density for excitons 2 and 4 (Figure 4.1). The spatial location of the two residues within the lower exciton manifold may explain, in part, their relative importance in controlling the excited-state energy transfer properties: C353 is active under both reducing and oxidizing conditions, while C49 is active only under oxidizing conditions when it can act as a thiyl radical.

Our results show that under oxidizing conditions, exciton density is steered toward quenching sites and the tryptophan/tyrosine chain. This chain has been identified as conserved within FMO[3], and Gray and coworkers have identified these chains as redox active outlets in other enzymatic systems[43]. We believe that steering toward the periphery of the chromophore structure does not significantly increase the chance of interacting with molecular oxygen because of the competition from this Trp/Tyr quencher. Indeed, it has been shown in previous publications that excitons are quenched more rapidly in the wild-type FMO protein under oxidizing conditions than under reducing conditions[1, 7]. We show the same trend in absolute valued signal amplitude at long waiting times. This data agrees with the dithionite effect reported by Blankenship in the 1990s[53]. In the wild-type protein, the signal amplitude decreases significantly faster in oxidizing conditions than reducing conditions for the diagonal peaks and the 4-1 and 2-1 cross peaks. In the doubly mutated C353A/C49A samples, the signal amplitudes under both redox conditions decay at similar rates. These results show that the redox-dependent steering of excitons in oxidizing conditions does indeed lead to increased quenching by the cysteine residues.

4.8 Supporting Material: Redfield Model Accounts for All Perturbative Changes to System

The Redfield model, an equation for EET that is perturbative in the system-bath coupling, explains how the cysteine residues electrostatically change the electronic Hamiltonian of the chromophores under different redox conditions. In 2016, Kell et al. used an updated FMO Hamiltonian averaged over static disorder with different spectral density and static disorder parameters for site III, which enabled a more accurate model of energy transfer between adjacent excitons in FMO [45]. This model reproduces the τ_{21} and τ_{42} time constants for the reduced wild-type FMO from our experimental data, but not the τ_{41} time constant. The energy gap between excitons 4 and 1 is approximately 260 cm^{-1}, which corresponds to

a mode observed in the hole-burning spectra of bacteriochlorophyll-a[54, 55] and has been assigned to an intrinsic vibration in the pigment. Once we add a Gaussian curve centered at 260 cm^{-1} to the spectral density of each site (Figure 4.3A), we are able to reproduce the τ_{41} time constant (approx. 500 fs) from the reduced wild-type experimental data. We take this Hamiltonian and spectral density parameters in our calculations to represent the reduced wild-type FMO.

The necessary addition of the resonant vibrational mode to the Redfield model developed by Kell et al. in order to reproduce the τ_{41} time constant suggests vibronic coupling in the reduced FMO protein. Vibronic coupling occurs when an electronic energy level mixes with an excited vibrational state of another exciton. Here, the electronic and vibrational eigenstates of the system Hamiltonian become non-trivially mixed due to the energy gap between the electronic states being nearly resonant with the vibrational transition[29]. This coupling implies that the eigenstates of the FMO Hamiltonian cannot be purely electronic in nature but must have some vibrational component. This mixing necessarily affects the energy transfer dynamics. In the case of 4-1 energy transfer in FMO, a vibrational mode in bacteriochlorophyll-a couples the two excitonic states.

We found the six-dimensional space formed by perturbation of the energies and Huang-Rhys factors of sites II, III, and IV, which each make up a portion of the electron density for excitons 1, 2, and 4 (see Figure 4.1), sufficient to fit all our observations. In this six-dimensional space, mutation and oxidation can each be represented as vectors, shifting site energies and bath couplings. We constrained the time constant fits by requiring that the eight samples (FMO wild-type and C353A, C49A, and C353A/C49A mutant samples under oxidizing and reducing conditions) be internally consistent such that the mutation and oxidation vectors are both additive (Figure 4.3 and 4.4, respectively).

In the Redfield analysis, we varied the Huang-Rhys factors because the centerline slope (CLS) traces for excitons were different between samples. It has been shown that the wait-

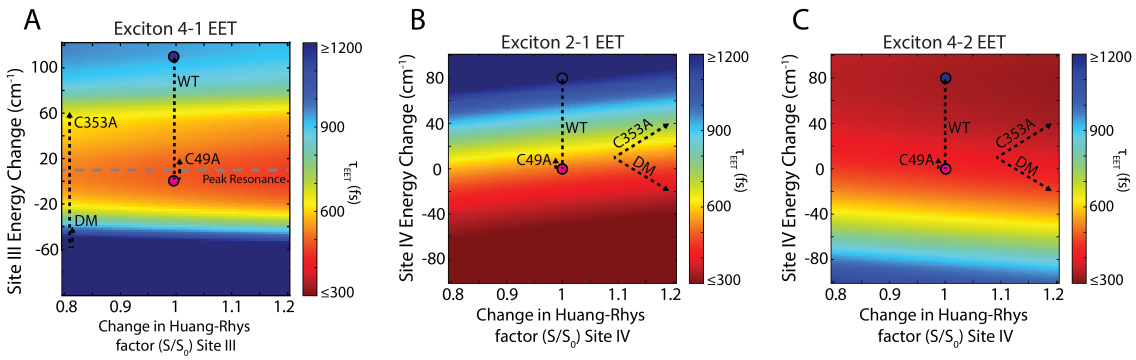

Figure 4.4: Redfield energy transfer maps displaying the cooperative effect of oxidizing each sample.

ing time change in the CLS in a two-dimensional spectrum corresponds to the decay of the frequency-frequency correlation function for that transition[56]. Thus, there are bath dynamics that differently modulate the energy levels of the excitons in each system. We can thus expect reasonable differences in the bath coupling terms (Huang-Rhys factors) in each FMO sample.

The fitting for the Redfield analysis was constrained such that the values for site energies and Huang-Rhys factors are internally consistent for all samples and all three time constants τ_{41}, τ_{42}, and τ_{21}. For mutation, it can be seen that for both sets of oxidizing and reducing samples, the changes in double mutant values are the sum of the changes in the two single mutant values:

$$\Delta mut_{\mathrm{C353A/C49A}} = \Delta mut_{\mathrm{C49A}} + \Delta mut_{\mathrm{C353A}} \tag{4.1}$$

This is true both for individual site changes and individual spectral density changes. We discussed that there are other redox-active residues in the complex that affect the ultrafast dynamics because the double mutant time constants change when oxidized. When we oxidize C353 plus C49 plus these 'other' residues individually, their sum total effect is equal to oxidizing the wild-type. Thus, the total change in the wild-type parameters must be equal to the change in the parameters due to these other residues plus the change due to each single

mutant. However, the oxidation of each single mutant sample also includes the contribution from the other residues. Therefore, the oxidation effect of each individual cysteine residue must be from the other corresponding single mutant minus the double mutant. Internal consistency under oxidation follows the following formula:

$$\begin{aligned} \Delta ox_{\mathrm{WT}} &= \Delta ox_{\mathrm{DM}} + (\Delta ox_{\mathrm{C353A}} - \Delta ox_{\mathrm{DM}}) + (\Delta ox_{\mathrm{C49A}} - \Delta ox_{\mathrm{DM}}) \\ &= \Delta ox_{\mathrm{C353A}} + \Delta ox_{\mathrm{C49A}} - \Delta ox_{\mathrm{DM}} \end{aligned} \tag{4.2}$$

Here, Δox_i= *site energy*$_{oxidized,i}$ - *site energy*$_{reduced,i}$ for each time constant. The term $\Delta ox_{\mathrm{C353A/C49A}}$ represents oxidation of the 'other' residues, the term Δ $\mathrm{ox_{C353A}}$-$\Delta\mathrm{ox_{DM}}$ represents oxidation of C49, and the term $\Delta\mathrm{ox_{C49A}}$-$\Delta\mathrm{ox_{DM}}$ represents oxidation of C353. When we oxidize the double mutant, we are only oxidizing the 'other' residues. When we oxidize the C353A sample, we are in reality oxidizing C49 plus the 'other' residues, and vise versa for oxidizing the C49A sample. This effect can be seen visually in Figure 4.4. Each individual site and Huang-Rhys factor in the theoretical values of Table 4.2 follows this pattern of consistency.

In addition to vibronic tuning, the changes to the FMO Hamiltonian revealed by our Redfield model suggest that changes to the protein environment likely affect site II, but the specific effects are more difficult to determine with confidence because the contribution numbers $\mathrm{c_{mM}}^2$ for site II to excitons 1, 2, and 4 are small[21]. The redox-dependent change in bacteriochlorophyll-*a* site IV energy, however, shows similar trends to that of site III. Under reducing conditions, the C353A and C353A/C49A mutants have slower τ_{21} and τ_{41} time constants and faster τ_{42} time constants than the wild-type sample (Table 4.1). This effect is achieved in the Redfield model by raising the energy of site IV by 10-20 $\mathrm{cm^{-1}}$ (Figure 4.3C-D). As with site III, oxidizing the wild-type protein raises the energy of site IV. Figure 4.3C-D shows that when the energy of site IV is raised, the 2-1 energy gap increases and the 4-2 energy gap decreases; τ_{21} slows down and τ_{42} speeds up as the energy gaps shift

in resonance with the low energy region in the spectral density. We also note that while oxidation increases site III energy in both single mutants, the changes in site III and IV energies are more significant in C353A than in C49A (Tables 4.1 and 4.2). As C353A is inactive in the oxidized C353A mutant, we conclude that the C49 residue exerts a larger redox-dependent effect on the energy transfer between excitons.

REFERENCES

[1] Gregory S. Orf, Rafael G. Saer, Dariusz M. Niedzwiedzki, Hao Zhang, Chelsea L. McIntosh, Jason W. Schultz, Liviu M. Mirica, and Robert E. Blankenship. Evidence for a cysteine-mediated mechanism of excitation energy regulation in a photosynthetic antenna complex. *Proceedings of the National Academy of Sciences*, 113(31):E4486–E4493, 2016.

[2] Rafael Saer, Gregory S Orf, Xun Lu, Hao Zhang, Matthew J Cuneo, Dean AA Myles, and Robert E Blankenship. Perturbation of bacteriochlorophyll molecules in fenna–matthews–olson protein complexes through mutagenesis of cysteine residues. *Biochim. Biophys. Acta - Bioenergetics*, 1857(9):1455–1463, 2016.

[3] Marco A. Allodi, John P. Otto, Sara H. Sohail, Rafael G. Saer, Ryan E. Wood, Brian S. Rolczynski, Sara C. Massey, Po-Chieh Ting, Robert E. Blankenship, and Gregory S. Engel. Redox conditions affect ultrafast exciton transport in photosynthetic pigment–protein complexes. *The Journal of Physical Chemistry Letters*, 9(1):89–95, 2018.

[4] R. E. Fenna and B. W. Matthews. Chlorophyll arrangement in a bacteriochlorophyll protein from chlorobium limicola. *Nature*, 258(5536):573–577, 1975.

[5] Zhenfeng Liu, Hanchi Yan, Kebin Wang, Tingyun Kuang, Jiping Zhang, Lulu Gui, Xiaomin An, and Wenrui Chang. Crystal structure of spinach major light-harvesting complex at 2.72 Å resolution. *Nature*, 428(6980):287–292, 2004.

[6] Robert E. Blankenship. *Molecular Mechanisms of Photosynthesis*. Wiley/Blackwell, Chichester, West Sussex, 2nd edition, 2014.

[7] Gregory S. Orf and Robert E. Blankenship. Chlorosome antenna complexes from green photosynthetic bacteria. *Photosynthesis Research*, 116(2):315–331, 2013.

[8] Hui Li, Niels-Ulrik Frigaard, and Donald A. Bryant. [2fe-2s] proteins in chlorosomes: Csmi and csmj participate in light-dependent control of energy transfer in chlorosomes of chlorobaculum tepidum. *Biochemistry*, 52(8):1321–1330, 2013.

[9] Thomas M. Wahlund, Carl R. Woese, Richard W. Castenholz, and Michael T. Madigan. A thermophilic green sulfur bacterium from new zealand hot springs, chlorobium tepidum sp. nov. *Archives of Microbiology*, 156(2):81–90, 1991.

[10] Tobias Brixner, Jens Stenger, Harsha M. Vaswani, Minhaeng Cho, Robert E. Blankenship, and Graham R. Fleming. Two-dimensional spectroscopy of electronic couplings in photosynthesis. *Nature*, 434(7033):625–628, 2005.

[11] G. S. Engel, T. R. Calhoun, E. L. Read, T. K. Ahn, T. Mancal, Y. C. Cheng, R. E. Blankenship, and G. R. Fleming. Evidence for wavelike energy transfer through quantum coherence in photosynthetic systems. *Nature*, 446(7137):782–6, 2007.

[12] Masoud Mohseni, Patrick Rebentrost, Seth Lloyd, and Alán Aspuru-Guzik. Environment-assisted quantum walks in photosynthetic energy transfer. *The Journal of Chemical Physics*, 129(17):174106, 2008.

[13] Gitt Panitchayangkoon, Dugan Hayes, Kelly A. Fransted, Justin R. Caram, Elad Harel, Jianzhong Wen, Robert E. Blankenship, and Gregory S. Engel. Long-lived quantum coherence in photosynthetic complexes at physiological temperature. *Proceedings of the National Academy of Sciences*, 107(29):12766–12770, 2010.

[14] Erling Thyrhaug, Karel Žídek, Jakub Dostál, David Bína, and Donatas Zigmantas. Exciton structure and energy transfer in the fenna–matthews–olson complex. *The Journal of Physical Chemistry Letters*, 7(9):1653–1660, 2016.

[15] Jakub Dostál, Jakub Pšenčík, and Donatas Zigmantas. In situ mapping of the energy flow through the entire photosynthetic apparatus. *Nature Chemistry*, 8:705, 2016.

[16] Hong-Guang Duan, Valentyn I. Prokhorenko, Richard J. Cogdell, Khuram Ashraf, Amy L. Stevens, Michael Thorwart, and R. J. Dwayne Miller. Nature does not rely on long-lived electronic quantum coherence for photosynthetic energy transfer. *Proceedings of the National Academy of Sciences*, 114(32):8493–8498, 2017.

[17] Margherita Maiuri, Evgeny E. Ostroumov, Rafael G. Saer, Robert E. Blankenship, and Gregory D. Scholes. Coherent wavepackets in the fenna–matthews–olson complex are robust to excitonic-structure perturbations caused by mutagenesis. *Nature Chemistry*, 10:177, 2018.

[18] Erling Thyrhaug, Roel Tempelaar, Marcelo J. P. Alcocer, Karel Žídek, David Bína, Jasper Knoester, Thomas L. C. Jansen, and Donatas Zigmantas. Identification and characterization of diverse coherences in the fenna–matthews–olson complex. *Nature Chemistry*, 10(7):780–786, 2018.

[19] Marten L. Chaillet, Florian Lengauer, Julian Adolphs, Frank Müh, Alexander S. Fokas, Daniel J. Cole, Alex W. Chin, and Thomas Renger. Static disorder in excitation energies of the fenna–matthews–olson protein: Structure-based theory meets experiment. *The Journal of Physical Chemistry Letters*, 11(24):10306–10314, 2020.

[20] Jianzhong Wen, Hao Zhang, Michael L. Gross, and Robert E. Blankenship. Membrane orientation of the fmo antenna protein from lt;emgt;chlorobaculum tepidumlt;/emgt; as determined by mass spectrometry-based footprinting. *Proceedings of the National Academy of Sciences*, 106(15):6134, 2009.

[21] Simone I. E. Vulto, Michiel A. de Baat, Robert J. W. Louwe, Hjalmar P. Permentier, Tatjana Neef, Mette Miller, Herbert van Amerongen, and Thijs J. Aartsma. Exciton simulations of optical spectra of the fmo complex from the green sulfur bacterium chlorobium tepidum at 6 k. *The Journal of Physical Chemistry B*, 102(47):9577–9582, 1998.

[22] Julia Adolphs and Thomas Renger. How proteins trigger excitation energy transfer in the fmo complex of green sulfur bacteria. *Biophysical Journal*, 91(8):2778–2797, 2006.

[23] Anton Khmelnitskiy, Adam Kell, Tonu Reinot, Rafael G. Saer, Robert E. Blankenship, and Ryszard Jankowiak. Energy landscape of the intact and destabilized fmo antennas from c. tepidum and the l122q mutant: Low temperature spectroscopy and modeling study. *Biochimica et Biophysica Acta (BBA) - Bioenergetics*, 1859(3):165–173, 2018.

[24] Brian S. Rolczynski, Haibin Zheng, Ved P. Singh, Polina Navotnaya, Alan R. Ginzburg, Justin R. Caram, Khuram Ashraf, Alastair T. Gardiner, Shu-Hao Yeh, Sabre Kais, Richard J. Cogdell, and Gregory S. Engel. Correlated protein environments drive quantum coherence lifetimes in photosynthetic pigment-protein complexes. *Chem*, 4(1):138–149, 2018.

[25] Elisabet Romero, Ramunas Augulis, Vladimir I. Novoderezhkin, Marco Ferretti, Jos Thieme, Donatas Zigmantas, and Rienk van Grondelle. Quantum coherence in photosynthesis for efficient solar-energy conversion. *Nature Physics*, 10(9):676–682, 2014.

[26] A. W. Chin, J. Prior, R. Rosenbach, F. Caycedo-Soler, S. F. Huelga, and M. B. Plenio. The role of non-equilibrium vibrational structures in electronic coherence and recoherence in pigment–protein complexes. *Nature Physics*, 9(2):113–118, 2013.

[27] Franklin D. Fuller, Jie Pan, Andrius Gelzinis, Vytautas Butkus, S. Seckin Senlik, Daniel E. Wilcox, Charles F. Yocum, Leonas Valkunas, Darius Abramavicius, and Jennifer P. Ogilvie. Vibronic coherence in oxygenic photosynthesis. *Nature Chemistry*, 6(8):706–711, 2014.

[28] Jianshu Cao, Richard J. Cogdell, David F. Coker, Hong-Guang Duan, Jürgen Hauer, Ulrich Kleinekathöfer, Thomas L. C. Jansen, Tomáš Mančal, R. J. Dwayne Miller, Jennifer P. Ogilvie, Valentyn I. Prokhorenko, Thomas Renger, Howe-Siang Tan, Roel

Tempelaar, Michael Thorwart, Erling Thyrhaug, Sebastian Westenhoff, and Donatas Zigmantas. Quantum biology revisited. *Science Advances*, 6(14):eaaz4888, 2020.

[29] Lili Wang, Marco A. Allodi, and Gregory S. Engel. Quantum coherences reveal excited-state dynamics in biophysical systems. *Nature Reviews Chemistry*, 3(8):477–490, 2019.

[30] Gregory D. Scholes, Graham R. Fleming, Lin X. Chen, Alán Aspuru-Guzik, Andreas Buchleitner, David F. Coker, Gregory S. Engel, Rienk van Grondelle, Akihito Ishizaki, David M. Jonas, Jeff S. Lundeen, James K. McCusker, Shaul Mukamel, Jennifer P. Ogilvie, Alexandra Olaya-Castro, Mark A. Ratner, Frank C. Spano, K. Birgitta Whaley, and Xiaoyang Zhu. Using coherence to enhance function in chemical and biophysical systems. *Nature*, 543(7647):647–656, 2017.

[31] Doran I. G. Bennett, Pavel Malý, Christoph Kreisbeck, Rienk van Grondelle, and Alán Aspuru-Guzik. Mechanistic regimes of vibronic transport in a heterodimer and the design principle of incoherent vibronic transport in phycobiliproteins. *The Journal of Physical Chemistry Letters*, 9(10):2665–2670, 2018.

[32] Samuel M. Blau, Doran I. G. Bennett, Christoph Kreisbeck, Gregory D. Scholes, and Alán Aspuru-Guzik. Local protein solvation drives direct down-conversion in phycobiliprotein pc645 via incoherent vibronic transport. *Proceedings of the National Academy of Sciences*, 115(15):E3342, 2018.

[33] Shu-Hao Yeh, Ross D. Hoehn, Marco A. Allodi, Gregory S. Engel, and Sabre Kais. Elucidation of near-resonance vibronic coherence lifetimes by nonadiabatic electronic-vibrational state character mixing. *Proceedings of the National Academy of Sciences*, 116(37):18263, 2019.

[34] Pavel Malý, Oscar J. G. Somsen, Vladimir I. Novoderezhkin, Tomáš Mančal, and

Rienk vanGrondelle. The role of resonant vibrations in electronic energy transfer. *ChemPhysChem*, 17(9):1356–1368, 2016.

[35] Miroslav Z. Papiz, Steve M. Prince, Tina Howard, Richard J. Cogdell, and Neil W. Isaacs. The structure and thermal motion of the b800–850 lh2 complex from rps.acidophila at 2.0Å resolution and 100k: New structural features and functionally relevant motions. *Journal of Molecular Biology*, 326(5):1523–1538, 2003.

[36] Stephen J. Harrop, Krystyna E. Wilk, Rayomond Dinshaw, Elisabetta Collini, Tihana Mirkovic, Chang Ying Teng, Daniel G. Oblinsky, Beverley R. Green, Kerstin Hoef-Emden, Roger G. Hiller, Gregory D. Scholes, and Paul M. G. Curmi. Single-residue insertion switches the quaternary structure and exciton states of cryptophyte light-harvesting proteins. *Proceedings of the National Academy of Sciences*, 111(26):E2666, 2014.

[37] Hui-Yuan S. Chen, Michelle Liberton, Himadri B. Pakrasi, and Dariusz M. Niedzwiedzki. Reevaluating the mechanism of excitation energy regulation in iron-starved cyanobacteria. *Biochimica et Biophysica Acta (BBA) - Bioenergetics*, 1858(3):249–258, 2017.

[38] Hui Li, Sara Jubelirer, Amaya M. Garcia Costas, Niels-Ulrik Frigaard, and Donald A. Bryant. Multiple antioxidant proteins protect chlorobaculum tepidum against oxygen and reactive oxygen species. *Archives of Microbiology*, 191(11):853, 2009.

[39] Elena V. Vassilieva, Mikhail L. Antonkine, Boris L. Zybailov, Fan Yang, Christiane U. Jakobs, John H. Golbeck, and Donald A. Bryant. Electron transfer may occur in the chlorosome envelope: the csmi and csmj proteins of chlorosomes are 2fe-2s ferredoxins. *Biochemistry*, 40(2):464–473, 2001.

[40] Katerina Krumova and Gonzalo Cosa. *Chapter 1 Overview of Reactive Oxygen Species*, volume 1, pages 1–21. The Royal Society of Chemistry, 2016.

[41] Harry B. Gray and Jay R. Winkler. The rise of radicals in bioinorganic chemistry. *Israel Journal of Chemistry*, 56(9-10):640–648, 2016.

[42] Brian S. Rolczynski, Polina Navotnaya, Hallie R. Sussman, and Gregory S. Engel. Cysteine-mediated mechanism disrupts energy transfer to prevent photooxidation. *Proceedings of the National Academy of Sciences*, 113(31):8562, 2016.

[43] Harry B. Gray and Jay R. Winkler. Hole hopping through tyrosine/tryptophan chains protects proteins from oxidative damage. *Proceedings of the National Academy of Sciences*, 112(35):10920–10925, 2015.

[44] Adam Kell, Ximao Feng, Mike Reppert, and Ryszard Jankowiak. On the shape of the phonon spectral density in photosynthetic complexes. *The Journal of Physical Chemistry B*, 117(24):7317–7323, 2013.

[45] Adam Kell, Robert E. Blankenship, and Ryszard Jankowiak. Effect of spectral density shapes on the excitonic structure and dynamics of the fenna–matthews–olson trimer from chlorobaculum tepidum. *The Journal of Physical Chemistry A*, 120(31):6146–6154, 2016.

[46] Paul W. Seakins. Product branching ratios in simple gas phase reactions. *Annual Reports Section "C" (Physical Chemistry)*, 103(0):173–222, 2007.

[47] Mino Yang and Graham Fleming. Influence of phonons on exciton transfer dynamics: comparison of the redfield, förster, and modified redfield equations. *Chemical Physics*, 275:355–372, 2002.

[48] Abraham Nitzan. *Chemical Dynamics in Condensed Phases: Relaxation, Transfer, And*

Reactions In Condensed Molecular Systems, volume 1 of *Oxford Graduate Texts*. Oxford University Press, 1st edition, 2014.

[49] Elad Harel, Andrew F. Fidler, and Gregory S. Engel. Real-time mapping of electronic structure with single-shot two-dimensional electronic spectroscopy. *Proceedings of the National Academy of Sciences*, 107(38):16444–16447, 2010.

[50] Elad Harel, Andrew F. Fidler, and Gregory S. Engel. Single-shot gradient-assisted photon echo electronic spectroscopy. *The Journal of Physical Chemistry A*, 115(16):3787–3796, 2011.

[51] Peter D. Dahlberg, Po-Chieh Ting, Sara C. Massey, Marco A. Allodi, Elizabeth C. Martin, C. Neil Hunter, and Gregory S. Engel. Mapping the ultrafast flow of harvested solar energy in living photosynthetic cells. *Nature Communications*, 8(1):988, 2017.

[52] Sara H. Sohail, Peter D. Dahlberg, Marco A. Allodi, Sara C. Massey, Po-Chieh Ting, Elizabeth C. Martin, C. Neil Hunter, and Gregory S. Engel. Communication: Broad manifold of excitonic states in light-harvesting complex 1 promotes efficient unidirectional energy transfer in vivo. *The Journal of Chemical Physics*, 147(13):131101, 2017.

[53] Wenli Zhou, Russell LoBrutto, Su Lin, and Robert E. Blankenship. Redox effects on the bacteriochlorophyll -containing fenna-matthews-olson protein fromchlorobium tepidum. *Photosynthesis Research*, 41(1):89–96, 1994.

[54] V. Zazubovich, I. Tibe, and G. J. Small. Bacteriochlorophyll a franckcondon factors for the s0 $\rightarrow$ s1(qy) transition. *The Journal of Physical Chemistry B*, 105(49):12410–12417, 2001.

[55] Vivek Tiwari, William K. Peters, and David M. Jonas. Electronic resonance with anticorrelated pigment vibrations drives photosynthetic energy transfer outside the adiabatic framework. *Proceedings of the National Academy of Sciences*, 110(4):1203, 2013.

[56] Kyungwon Kwak, Sungnam Park, Ilya J. Finkelstein, and M. D. Fayer. Frequency-frequency correlation functions and apodization in two-dimensional infrared vibrational echo spectroscopy: A new approach. *The Journal of Chemical Physics*, 127(12):124503, 2007.

CHAPTER 5

REDOX CONDITIONS CORRELATED WITH VIBRONIC COUPLING MODULATE QUANTUM BEATS IN PHOTOSYNTHETIC PIGMENT-PROTEIN COMPLEXES

The work presented in this Chapter has been published and adapted with permission from: J.S. Higgins, M.A. Allodi, L.T. Lloyd, J.P. Otto, S.H. Sohail, R.G. Saer, R.E. Wood, S.C. Massey, P-C. Ting, R.E. Blankenship, and G.S. Engel, "Redox conditions correlated with vibronic coupling modulate quantum beats in photosynthetic pigment-protein complexes," *PNAS* 118, e2112817118 2021.[1]

Quantum coherences, observed as time-dependent beats in ultrafast spectroscopic experiments, arise when light-matter interactions prepare systems in superpositions of states with differing energy and fixed phase across the ensemble. Such coherences have been observed in photosynthetic systems following ultrafast laser excitation, but what these coherences imply about the underlying energy transfer dynamics remains subject to debate. Recent work showed that redox conditions tune vibronic coupling in the Fenna-Matthews-Olson (FMO) pigment-protein complex in green sulfur bacteria, raising the question of whether redox conditions may also affect the long-lived (100 fs) quantum coherences observed in this complex. In this work, we perform ultrafast two-dimensional electronic spectroscopy measurements on the FMO complex under both oxidizing and reducing conditions. We observe that many excited state coherences are exclusively present in reducing conditions and are absent or attenuated in oxidizing conditions. Reducing conditions mimic the natural conditions of the complex more closely. Further, the presence of these coherences correlates with the vibronic coupling that produces faster, more efficient energy transfer through the complex under re-

1. Thank you to Prof. Robert Blankenship and Dr. Rafael Saer for providing the biological samples, and to Dr. Karen Watters for scientific editing of the manuscript

ducing conditions. The growth of coherences across the waiting time and the number of beating frequencies across hundreds of wavenumbers in the power spectra suggest that the beats are excited state coherences with mostly vibrational character whose phase relationship is maintained through the energy transfer process. Our results suggest that excitonic energy transfer proceeds through a coherent mechanism in this complex and that the coherences may provide a tool to disentangle coherent relaxation from energy transfer driven by stochastic environmental fluctuations.

5.1 Significance of Long-Lived Coherences

Photosynthetic organisms evolved their light harvesting antenna complexes to optimize energy transfer. It was recently shown that the redox environment can tune the mixing of electronic and vibrational states to steer energy through different pathways of a pigment-protein complex. Quantum beating signals in spectra of pigment-protein complexes have been used to probe the excited state dynamics within the complexes, but the microscopic dynamics that generate these signals and their role in promoting energy transfer are not fully understood. Here, we show that the redox environment that tunes energy transfer similarly tunes the quantum beating signals in the same complex. We find that the beats report on excited state vibrations that maintain coherence through the vibronically enhanced energy transfer process.

5.2 Introduction to Quantum Coherences

Photosynthesis relies on light harvesting pigment-protein complexes that absorb sunlight and transfer the energy to reaction centers[1]. The growth, development, and productivity of a photosynthetic organism are bounded by how efficiently antenna complexes can funnel solar energy to reaction centers [2, 3, 4] and the robustness of these complexes to environmental

damage. To optimize both light absorption and energy transfer, the protein both serves as a structural scaffold that holds the light-absorbing pigments at specific relative orientations and also a dissipative bath to facilitate relaxation [5]. Both inter-pigment coupling and pigment-bath coupling contribute to the energy transfer dynamics of antenna complexes [6, 7, 8].

The microscopic motions that drive energy transfer can preserve the quantum coherence in a system. Quantum coherence is an ensemble phenomenon that results from sustained phase relationships between superpositions of states across space and time [9]. It can be detected as time-domain beating signals in two-dimensional and pump-probe spectra. Dephasing and decoherence, which diminish the beating amplitude of the signal, depend critically on complex dynamical interactions between the system and the bath; therefore, quantum beats arising from coupling between excited states offer unique insight into system-bath interactions and the relevant energy transport dynamics of complex systems [10, 11]. Long-lived quantum beats persisting for hundreds of femtoseconds to picoseconds have been observed in the FMO pigment-protein complex from green sulfur bacteria [8, 12, 13, 14]. Although initially assigned to long-lived coherences between electronic states [8], later studies have hypothesized that these coherences arise from vibrational states on the ground state surface [15, 16, 17] or between vibronic states [18, 19], which could microscopically explain how the beats can persist for hundreds of femtoseconds. Vibronic states arise when excitonic states with different levels of vibrational excitation couple to form a new basis of mixed electronic-vibrational states[20]. Recent work using rephasing pathways to isolate excited state coherence signals has suggested that the purely electronic coherences in FMO dephase within 100 fs[19, 21]. The longer lived coherences are likely a combination of ground state vibrational, and excited state vibrational, and vibronic coherences, though their functional role in photosynthetic light harvesting is not yet fully understood[22, 23, 24, 25].

Changes in the redox environment of an antenna complex can additionally affect the

observed photophysical and transport properties. In the FMO complex, the addition of an oxygen-scavenging reducing agent, such as sodium dithionite, significantly enhances the fluorescence quantum yield[26]. The addition of such a reducing agent mimics the physiological environment of green sulfur bacteria, which are anaerobic phototrophs that cannot survive in highly oxic environments[27]. Recent work on the FMO complex identified a pair of cysteine residues (Figure 5.1A) that, upon oxidation of the side chain thiol to a thiyl radical, nonradiatively quench excitations via a charge transfer and recombination mechanism[28, 29, 30]. Ultrafast spectroscopic experiments have shown that the excitonic transport dynamics through the FMO complex are faster under reducing conditions[31]. In reducing conditions, the cysteine residues tune the resonant vibronic coupling between the excitons and pigment vibrations to enhance energy transfer, whereas in oxidizing conditions, the vibronic coupling is detuned to steer excitations toward the nonradiative quenching sites[32]. These results showed that resonant vibrations play a definitive role in photosynthetic energy transport, as conceptualized originally by the Olaya-Castro group[33, 34, 35]. In particular, quantized vibrations can promote non-sequential energy transport [33], shown by the vibronically enhanced exciton 4-1 energy transfer in FMO in reducing conditions[32]. Given the influence of redox on excitonic energy transport, it is likely that redox environment also affects excited state quantum beating signals observed in photosynthetic complexes.

In this work, we use two-dimensional electronic spectroscopy (2DES) to investigate how the long-lived quantum coherences observed in the FMO complex are affected by oxidizing and reducing conditions and the subsequent influence on energy transfer. We observe a positive relationship between enhanced quantum coherence signals and the vibronic coupling observed in reducing conditions[32]. Using a spectral analysis method described previously[19], we find that under reducing conditions, the beating magnitudes of many long-lived coherences are increased relative to their magnitudes under oxidizing conditions and that many of the quantum beats appear as below-diagonal stimulated emission features in the 2D spec-

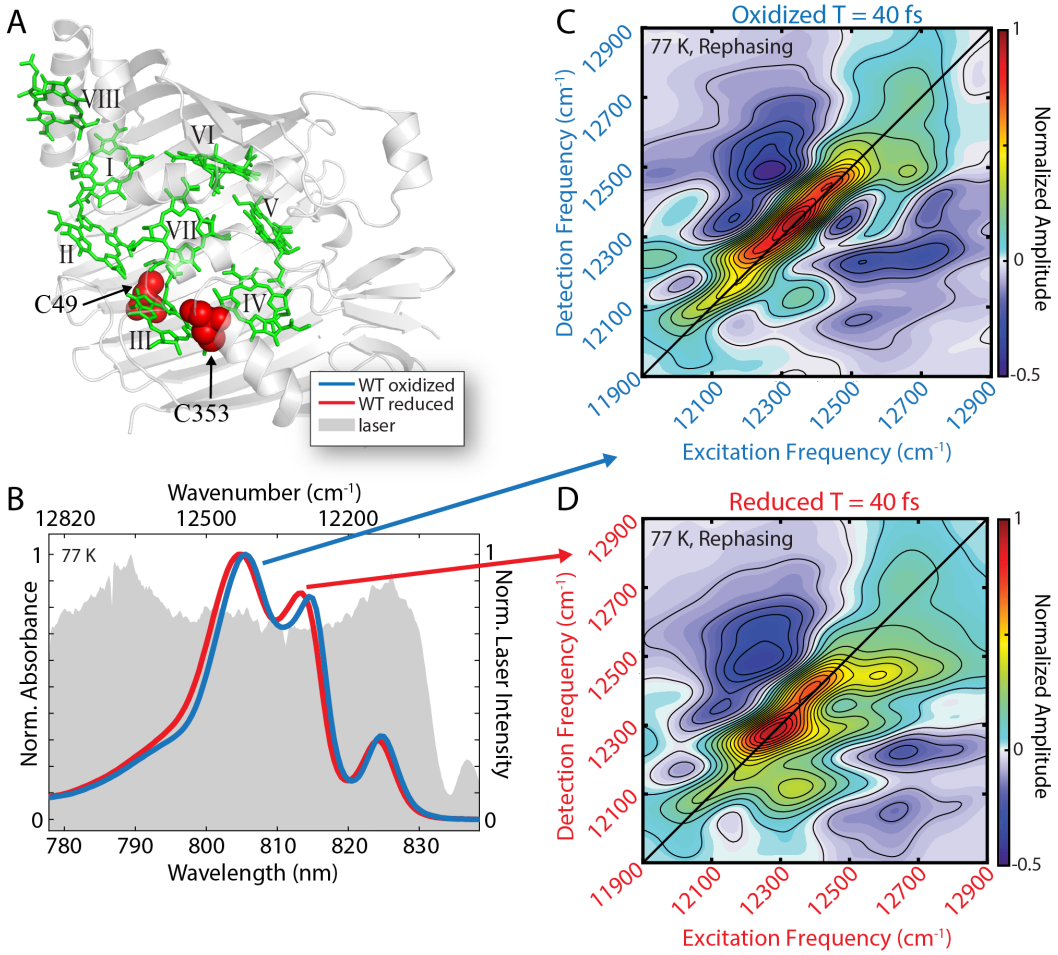

Figure 5.1: Redox condition affects excited state behavior in the wild-type FMO complex. A) Structure of the FMO complex and the eight bacteriochlorophyll-a sites held by the protein scaffold (PDB: 3ENI)[29]. Shown in red are the two cysteine residues, C49 and C353, that are known to steer and quench excitations in oxidizing conditions and tune vibronic coupling for enhanced energy transfer in reducing conditions[30, 32]. B) Linear absorption spectra of the wild-type oxidized (blue) and wild-type reduced (red) FMO complex at 77 K. Shown in gray is the laser spectrum used. C, D) Rephasing 2D electronic spectra under oxidizing and reducing conditions at waiting time T = 40 fs. Differences in the lower-diagonal cross peaks between experiments indicate faster, more efficient energy transfer when the complex is reduced.

trum (i.e. features which result from downhill energy transfer in the excited state). The location of the long-lived coherences correlates with increased vibronic coupling and more efficient downhill energy transfer through the FMO complex[31, 32]. The strength of beating increases with waiting time up to two picoseconds, which we ascribe to an excited state coherence transfer. The persistence of multiple beating frequencies below the diagonal and their growth with waiting time suggests that many of the coherences arise from excited state vibrational coherences that retain their phase relationship through the vibronically enhanced energy transfer process. The redox-dependent coherent behavior shown here suggests that sample preparation and handling between experiments may underlie much of the controversy surrounding the assignment of quantum coherences in biology.

5.3 Quantum Beats Correlate with Redox Conditions and Enhanced Energy Transport

Linear absorption spectra and 2D electronic spectra of the FMO complex at 77 K were collected under both oxidizing and reducing conditions using the same methods described previously[31, 32]. The linear absorption spectra (Figure 5.1B) show that a change in the redox condition shifts the peak positions of the absorption spectrum, previously shown to be due to the oxidation state of the cysteine residues C49 and C353 and likely other residues[30, 31]. Two-dimensional electronic spectroscopy (2DES) can follow the time evolution of both population and coherence signals as they evolve through the waiting time, allowing us to investigate whether the coherent behavior of the FMO complex is redox-dependent. In 2DES, we illuminate the sample with four laser pulses to observe the molecular response as a function of the three time periods between pulses, $R^{(3)}$=(τ,T,t). Using Fourier analysis and interpolation, we process the signal and cast the first and third domains into the frequency representation, Sig(ω_τ,T,ω_t). Doing so allows us to correlate the excitation frequency of the system ω_τ with the detection frequency ω_t at different waiting times T. Rephasing

spectra for oxidized and reduced FMO are plotted in Figure 5.1C-D for T = 40 fs. These spectra show clear differences in the cross-peak amplitude between reducing and oxidizing conditions, indicating more efficient population transfer in reducing conditions that has been observed previously[31, 36]. This enhanced efficiency is due to a resonant vibrational mode that couples excitons 4 and 1[32].

Time-domain beats appear as signal oscillations during the waiting time T with a frequency proportional to the energy difference between the states[8, 11, 37, 38]. To isolate the coherent beating signals, we remove the exponentially decaying contributions to the waiting time signals that correspond to population dynamics. We then Fourier transform the detrended traces to generate a waiting time frequency signal, Sig(ω_τ,ω_T,ω_t). To focus solely on the longer-lived coherences in the spectra, we only include data points after waiting time T = 240 fs in the Fourier transform. The oxidized and reduced data are normalized so that we can compare the relative magnitude of the spectral power between the two redox conditions.

In rephasing pathways, the sign of the phase evolution during τ is opposite to that of t because the state with higher energy switches from the bra to the ket in the t domain [19]. Positive and negative wavenumbers in ω_T report on coherences that oscillate in opposite directions in T [39, 40], corresponding to which state of the density matrix is higher in energy. This distinction enables differentiation between beating features occurring on the ground or excited state. For our 77 K experiments, ground state bleach contributions to the rephasing pathway can only oscillate at negative frequency in the beating maps because the first two interactions prepare a $|\mathrm{g_0}\rangle\langle\mathrm{g_v}|$ coherence, where $\mathrm{g_v}$ denotes a higher vibrational state on the electronic ground state[11]. The only ground state bleach pathways that give a positive frequency occur from an initially vibrationally excited ground state $|\mathrm{g_v}\rangle\langle\mathrm{g_v}|$; however, these vibrations are suppressed because the necessary frequencies are several factors higher in energy than k_BT at the cryogenic temperatures measured here. Features that oscillate at positive frequencies therefore must be generated by stimulated emission or excited-state

absorption pathways and thus report on electronic, vibrational, or vibronic coherences in the excited state[19].

Power spectra for all beating frequencies ω_T integrated over different regions of the 2D spectra are shown in Figure 5.2. In the negative waiting time frequencies of each region, we observe many beating frequencies that likely are ground state vibrational coherences. There are also many positive beating frequencies between 0 and +1000 cm^{-1} that report on coherences in the excited state. Several of the observed frequencies are in good agreement with the fluorescence line narrowing spectra of FMO in the literature[41]. Many coherences match the frequencies observed in two-dimensional spectra of isolated bacteriochlorophyll-*a* molecules reported by Fransted et al. (e.g. 730 cm^{-1} and 550 cm^{-1})[42] and Ogilvie and coworkers (e.g. 201 cm^{-1} and 348 cm^{-1}) [24]. In the diagonal spectra (Figure 5.2E-F), some frequencies are only present in reducing conditions (e.g. the 335 cm^{-1} and 378 cm^{-1} pair in the exciton 4 diagonal region), but in general, many of the observed beats are similar in magnitude between redox conditions. In contrast, virtually all the positive beats in the below-diagonal beating spectra (Figure 5.2B-D) are higher in magnitude in reducing conditions than in oxidizing conditions. Because of the large number of observed frequencies, the beats likely report on energy gaps between states with mostly excited state vibrational character[6, 41, 43, 44, 45] rather than between purely electronic states. The below-diagonal regions correspond to the downhill energy transfer that is enhanced in reducing conditions (Figure 5.1C-D) due to the tuned vibronic coupling shown in a previous study [32], further suggesting that the redox-dependent positive-frequency beats are related to the vibronic coupling present only in reducing conditions. Additionally, many negative frequencies are enhanced in reducing conditions in the below-diagonal cross peak regions. We assign these beats to ground state vibrational coherences that are enhanced by the vibronic states in reducing conditions, as has been shown and discussed extensively in the literature[18, 15, 46, 47]. Other integrated regions display similar overall trends.

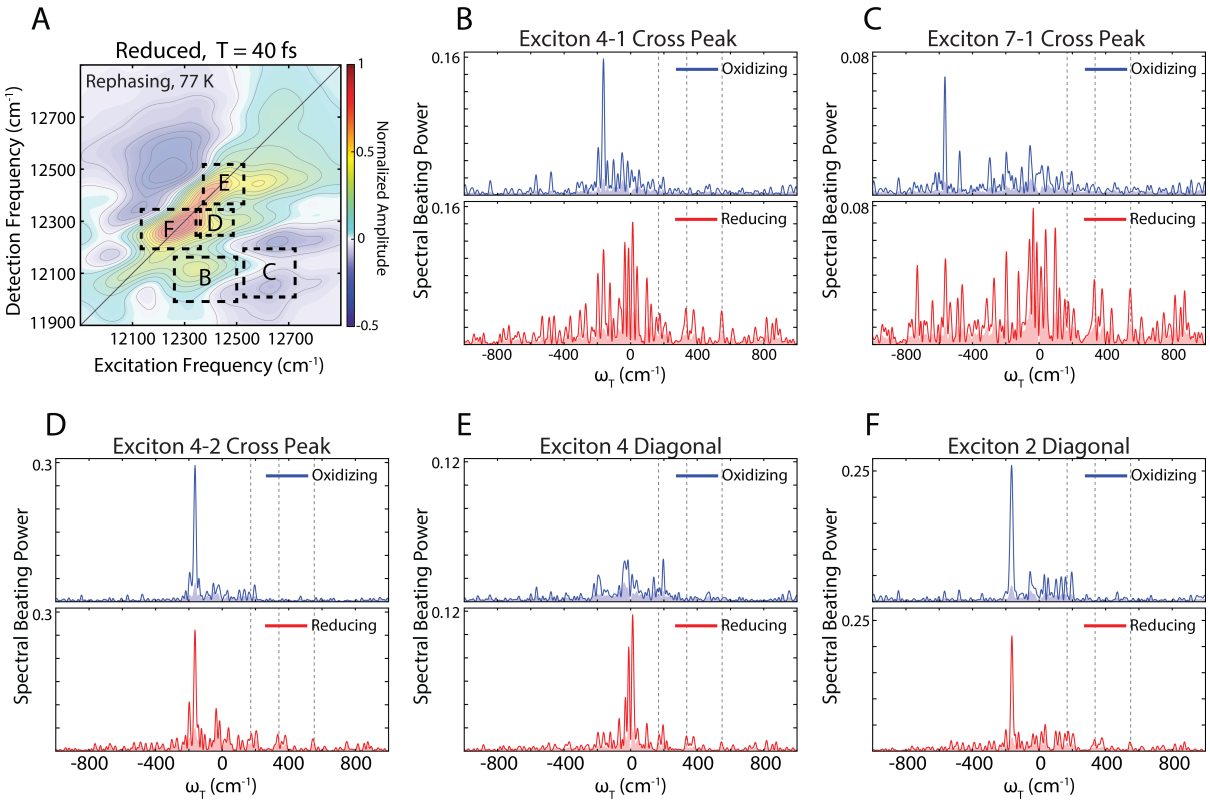

Figure 5.2: Rephasing power spectra for oscillations in T integrated over regions of the 2D spectrum. A) Reduced FMO 2D spectrum at T = 40 fs showing integrated regions. Regional power spectra for B-D) below-diagonal regions and E-F) diagonal regions. Oxidizing and reducing data are plotted in blue and red, respectively. The shaded regions represent the standard error over the mean. The dashed vertical lines mark positive beating frequencies at 167 cm^{-1}, 335 cm^{-1}, and 550 cm^{-1}, shown as beating maps in the next figure. In general, the magnitude of the beating signals is larger in the reduced data below the diagonal, particularly at positive frequencies, which result from coherences on the excited state. Diagonal power spectra show similar beating magnitudes between redox conditions. All time traces were Fourier transformed after T = 240 fs to focus on the long-lived coherent dynamics.

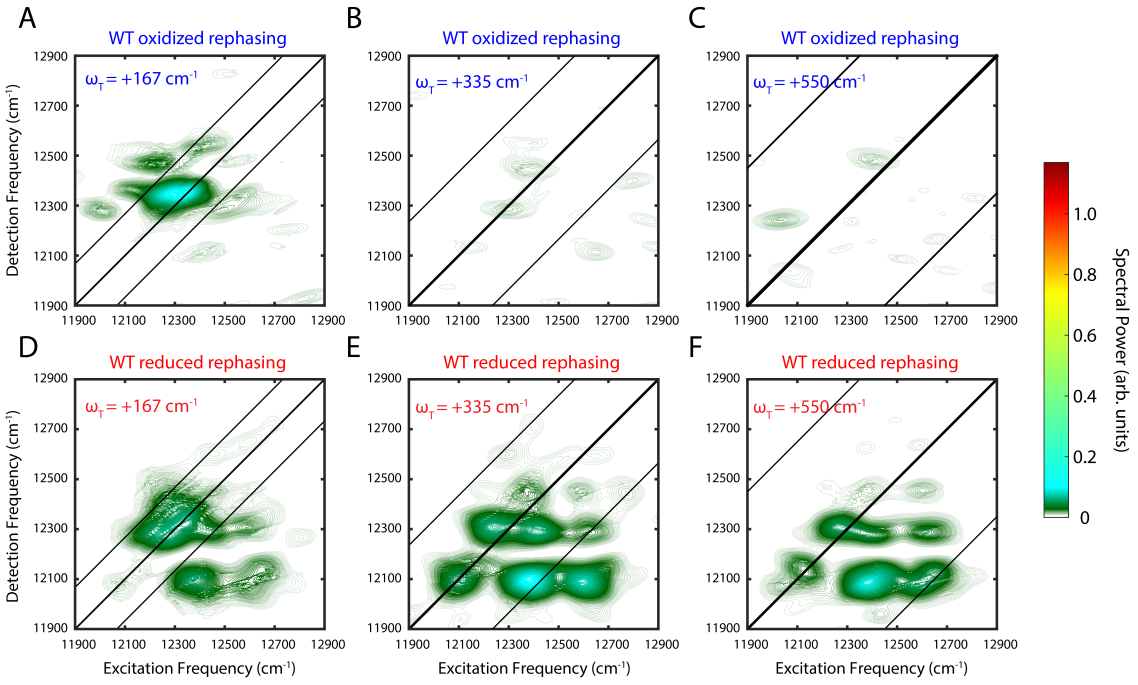

Figure 5.3: Beating amplitude maps at (A, D) +167 cm^{-1}, (B, E) +335 cm^{-1}, and (C, F) +550 cm^{-1} for rephasing FMO spectra under oxidizing and reducing conditions. The magnitude represents the relative beating strength for the ω_T frequency at each point on the 2D spectrum. A below-diagonal feature at the positive frequency only appears in reducing conditions. This region corresponds to downhill energy transfer in the complex, which is enhanced in reducing conditions[31, 32].

We generate beating maps at specific waiting time frequencies to reveal quantifiable changes in the quantum beats throughout the 2D spectrum. The spectra for the +167 cm^{-1}, +335 cm^{-1}, and +550 cm^{-1} coherent oscillations for both oxidizing and reducing conditions are shown in Figure 5.3. The magnitudes report on the relative strength of the beating signal at each point on the 2D spectrum. All beat maps for a given redox condition are normalized to the beating value of the summed frequency cube. At each frequency, there are clear differences between the two redox conditions. For the +167 cm^{-1} beating maps (Figure 5.3A, D), both oxidized and reduced spectra show a feature of similar magnitude on the main diagonal around 12,300 cm^{-1}, corresponding to the exciton 2-4 energies. However, the lineshape of the diagonal feature of the beating map is different between redox conditions, and the diagonal peak width is larger in reducing conditions. Similar features are notably absent in the oxidized spectra for +335 cm^{-1} and +550 cm^{-1} (Figure 5.3B, C) but present in the corresponding reduced spectra (Figure 5.3E, F). Additionally, the reduced beating maps for the three frequencies show a clear below-diagonal peak centered at 12,100 cm^{-1} on the detection axis that is almost entirely absent in the oxidized measurements. This feature is in close proximity to the exciton 1 energy on the detection axis[43, 48]. We observe the same structural pattern (i.e., below-diagonal features only present in reducing conditions) for several other positive beating frequencies, including 815 cm^{-1} and 1082 cm^{-1}. Taken together, the region-specific power spectra in Figure 5.2 and the beating maps in Figure 5.3 show that many observed long-lived quantum beats correlate with vibronically enhanced energy transfer through the FMO complex[32].

5.4 Time Evolution of Excited State Vibrational Coherences

To better understand the time evolution of these excited state coherences, we apply a sliding window Fourier transform to the detrended waiting time traces. We apply a window in the waiting time domain with a 1000 fs width and center waiting time value, T'[49]. Figure

5.4B shows a sliding window trace of the regionally averaged intensity of the below-diagonal beating feature in the reduced spectrum at +167 cm^{-1}. The feature clearly grows in at larger T' values. This effect can also be seen in Figure 5.5, which shows a reduced beating spectrum for the +167 cm^{-1} frequency at early (200 – 1200 fs) and later waiting times (1200 – 2200 fs). Both representations show that the beating intensities of the diagonal and below-diagonal features are greater at later waiting times. We show that the overall growth pattern of the +167 cm^{-1} feature does not change with different sliding window sizes in T or the size of the averaged region in ω_τ and ω_t. We show the growth and decay patterns in other excited state coherences. Beating frequencies adjacent to +167 cm^{-1} (125 cm^{-1} and 203 cm^{-1}) show qualitatively different trends, indicating that the sliding window Fourier transform does not affect all frequencies in the same manner. For a given beating frequency, there is a competition between growth due to coherence transfer and decay due to dephasing and decoherence[11]. This interplay produces different behavior between beating frequencies as the bath couples differently to each mode. Sliding window time trace differences between frequencies indicate that the bath environment affects these two competing forces differently. Frequencies such as +550 and +1082 cm^{-1} show similar growth to +167 cm^{-1}, indicating that many of the below-diagonal beats present only in reducing conditions grow with waiting time.

The previous observation that vibronic coupling between excitons 4 and 1 enhances energy transfer efficiency under reducing conditions[32] correlates with the beating patterns we observe. However, given the number of frequencies we see in reducing conditions (Figure 5.3), it is unlikely that the coherences are between these particular vibronic states, as the beating frequencies cannot all match the 4-1 exciton energy gap. The observed beats span over 1000 cm^{-1} (Figure 5.2), so it is unlikely that the coherences arise from different pairs of vibronic states because the beats would otherwise span a smaller frequency window. Rather, the beating signals most likely arise from coherences with largely vibrational character. The consistency between the coherence frequencies of isolated bacteriochlorophyll-*a* and these

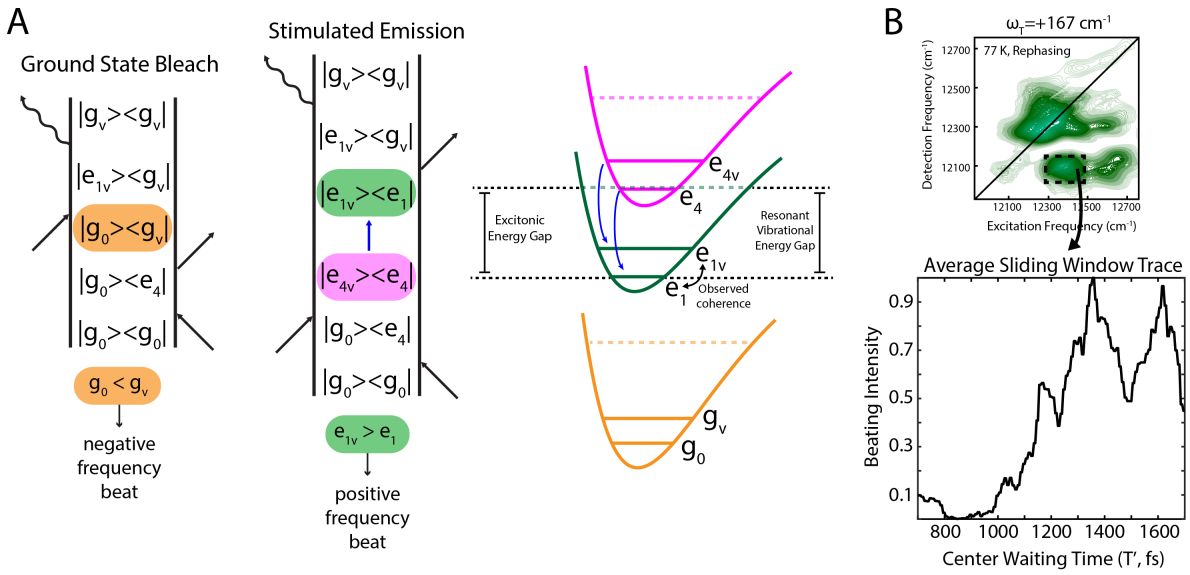

Figure 5.4: Proposed Feynman pathway explaining below-diagonal coherences observed at positive frequencies in the rephasing spectra. A) Ground state bleach pathways cannot contribute to the positive frequency because the energy of g_v, where the subscript v denotes an excited vibrational quantum, is greater than g_0, producing a negative frequency in T. The stimulated emission pathway contains a coherence transfer during T between excited state vibrational coherences on excitons 4 and 1. The observed beats below the diagonal are the vibrational coherences on exciton 1. Because $e_{1v}>e_1$, the waiting time frequency is positive. The enhanced energy transfer promoted by vibronic coupling in reducing conditions preserves the vibrational coherence[32]. B) Sliding window Fourier transform of the below-diagonal feature at +167 cm^{-1} using a 1000 fs window in T. The sliding trace shows that the coherence grows in with T, providing evidence for the coherence transfer pathway.

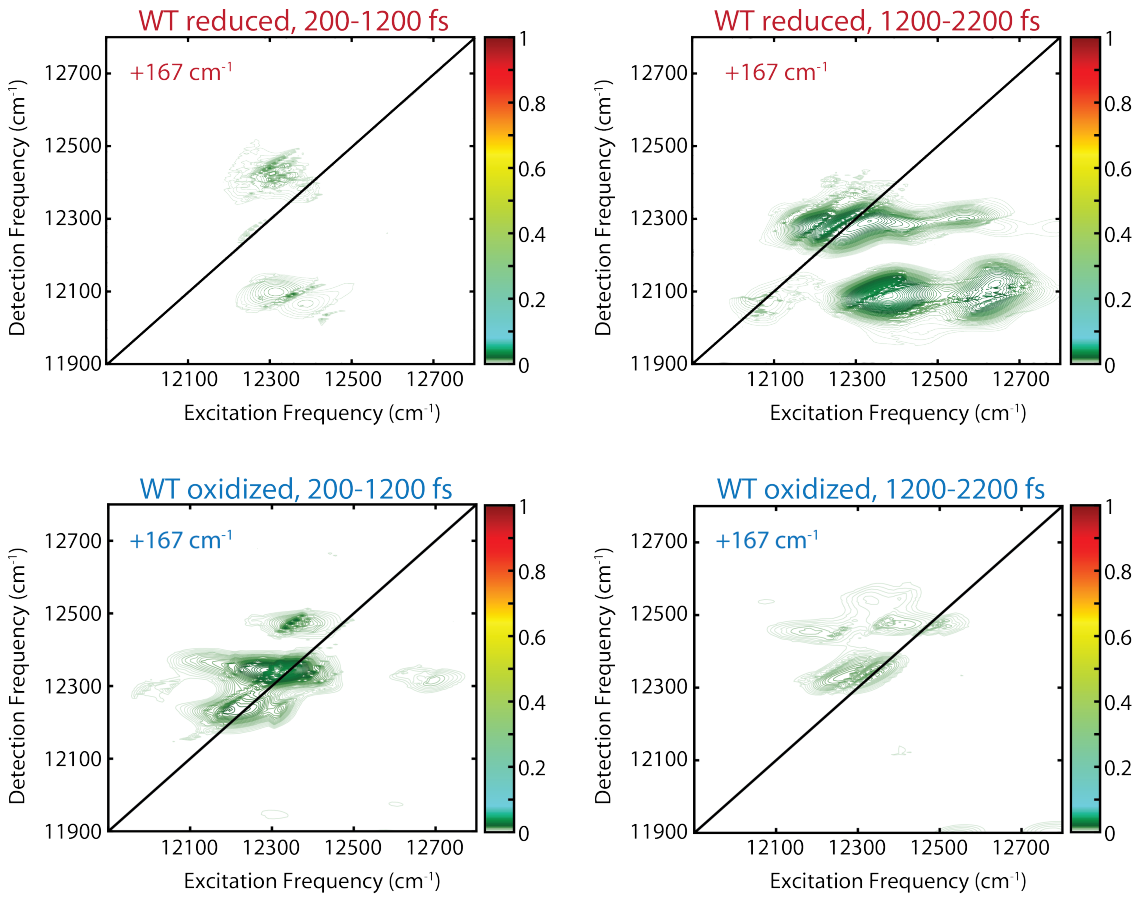

Figure 5.5: Beating amplitude maps for two waiting time ranges for the +167 cm^{-1} beating frequency of rephasing FMO spectra. In reducing conditions, the majority of the beating occurs over 1200 fs to 2200 fs, while the relatively smaller amount of beating in the oxidized spectra occurs over 200 fs to 1200 fs.

beats supports this vibrational picture[24, 42]. These coherences could be 'purely' vibrational or have small degrees of vibronic mixing with other excitonic surfaces. Either assignment would explain their long dephasing times and structural similarity in the beating spectra.

A proposed stimulated emission Feynman pathway that explains the beating signals is shown in Figure 5.4A. In this pathway, an excited state vibrational coherence starting on exciton 4 transfers to exciton 1 during the waiting time while maintaining the vibrational coherence. This latter coherence is observed as a below-diagonal beating signal. This is the most likely pathway for the beating signals because 1) the bra-ket energy difference is maintained over the energy transfer process, and 2) the position of the signals on the 2D spectrum is invariant to the energy of the excited vibration (see Supporting Section)[50, 51]. Similar pathways have been prescribed in the bacterial reaction center in purple bacteria[52]. Many excited state coherences of different excited state vibrational modes are accessed in the first two laser interactions in our experiment, which explains why we observe multiple beating frequencies in this region (Figure 5.3). The sliding window Fourier transform traces further support the downhill vibrational coherence transfer picture, as we see the growth of many modes with waiting time (Figure 5.4B). In this picture, the vibrational modes must be on a pigment or pigments where the two excitonic states overlap.

The process described here operates outside the typical assumptions for energy transfer because the vibrational coherence is not destroyed in the energy transfer process. The preserved coherence across multiple vibrational modes strongly suggests that the vibronically enhanced energy transfer must be a coherent process. In these data, the long-lived coherences present in reducing conditions are simply spectators to the enhanced energy transfer in reducing conditions. While the coherences themselves are largely vibrational in character, they are only observable because of the vibronic mixing that promotes energy transfer in the system. The vibrational coherences are thus sensitive probes of both enhanced energy transfer and the strong mixing of vibronic states in reducing conditions. Previous studies

have shown that cooperative bath motion around different pigments within a complex can maintain the lifetime of excited state coherences[53, 54, 55, 56]. These bath motions preserve the phase relationships across the ensemble due to the resonant vibronic coupling that promotes energy transfer in reducing conditions[57]. Such preservation of phase necessitates coherence transfer alongside population transfer, implying significant non-secular terms in the relaxation superoperator (see Ref. [58]). A full quantum mechanical description of this process would require that all relevant vibrations be treated as part of the system. Within a semiclassical approximation considering only the electronic states explicitly, the bath must be treated parametrically such that the same bath motions affect the time-varying Hamiltonian operating on both sides of the density matrix. This semiclassical approximation shows explicitly how the same bath motions can drive simultaneous relaxation on both the bra- and the ket-states to preserve phase across the ensemble.

It is further possible that the resonant vibronic coupling induced in reducing conditions alters the excited state potential energy surfaces such that many excited state vibrational energies are markedly different from their ground state energies. This coupling would drastically change the Duschinsky rotation matrix and subsequently alter the absorption and emission vibrational profiles and, in turn, the excited state vibrational coherences [59]. This effect may explain a number of coherences observed in this study that have not been observed in ground state spectroscopic experiments. The Duschinsky matrix has been calculated for isolated bacteriochlorophyll-a[44] and chlorophyll-a[59] molecules, and the subsequent effect on the excited state dynamics of light harvesting complexes has been discussed[59]. Future high-resolution spectroscopic methods should investigate the effect that redox-induced vibronic coupling has on the excited state vibrational structure of the FMO complex and how Duschinsky rotation ties in with the preservation of coherence through the energy transfer process.

5.5 Conclusions: Long-Lived Coherences, Vibronic Coupling, and Redox Conditions

In this study, we observe excited state quantum beats in the FMO complex that are exclusively present in reducing conditions. The coherences are located in below-diagonal regions of the 2D spectrum that correspond to enhanced energy transfer due to vibronic coupling between excitons. The coherences exist at multiple beating frequencies, from 100 cm^{-1} to 1000 cm^{-1}, indicating that the observed beats are likely excited state coherences with mostly vibrational character. Many of these coherences located on the below diagonal cross-peaks appear to increase in magnitude with waiting time, and we hypothesize that they result from a coherence transfer between excited state coherences on different excitonic surfaces (see Figure 5.4A, stimulated emission pathway). Interestingly, the location and growth of the coherences suggests that the vibronic coupling that enhances energy transfer in reducing conditions also preserves the coherence between a number of excited state vibrational modes. Coherence transfer has been previously observed and correlated with vibronic coupling in the reaction center of purple bacteria[52]. Alternatively, it is possible that the coherence itself is actually growing or being spontaneously generated with time as suggested by Olaya-Castro and coworkers [33, 34] as well as Plenio, Huelga, and coworkers[60]. Our results indicate that the redox condition of a pigment-protein complex must be known when assigning an observed beat signal to a specific quantum coherence. Indeed, much of the debate in the literature regarding the nature of these long-lived coherences may result from differences in experimental sample preparation between research groups as both samples and reducing agents are air-sensitive. Our results also show that excited state coherences observed in these spectra can serve as reporters on the vibronically enhanced energy transfer through the complex.

5.6 Experimental Methods

C. tepidum was grown, and FMO was isolated in CAPS (N-cyclohexyl-3-aminopropanesulfonic acid) buffer (pH 10.5) following well established literature procedures[30, 61, 62, 63]. Measurements in this study were taken on a mixture of glycerol (50 % by volume) and 20 mM CAPS-buffered (pH 10.5) FMO protein. Under oxidizing conditions, the samples were handled under ambient conditions without any further preparation; in the reducing case, sodium dithionite was added to the protein, buffer, and glycerol mixture to a concentration of 10 mM. The mixture was placed in a 200 μm quartz cuvette (Starna) that was prepared with a hydrophobic coating (SigmaCote, Sigma-Aldrich). The cuvette was loaded into a nitrogen-cooled cryostat (Oxford Instruments) and rapidly cooled to 77 K, forming a glass. The sample was held at 77 K for all measurements.

The 2D electronic spectra were acquired using the GRAPES single-shot spectrometer described in detail elsewhere[64, 65, 66]. In these experiments, the output of an ultrafast regenerative amplifier (Legend Elite USP, Coherent) centered at 800 nm and running at a 5 kHz repetition rate was focused through a tube containing 15 psi of Ar gas. The broadened light was subsequently focused in air a second time to produce a spectrum that spans from 775 nm to 840 nm. This bandwidth was compressed to a < 20 fs laser pulse using an optical pulse shaper (MIIPS Box 640, Biophotonics Solutions) running a MIIPS algorithm[67]. Beamsplitters generated four beams with parallel electric-field polarizations that were aligned to form a shifted boxcars geometry. Pulse 1 has a geometric tilt relative to pulses 2 and 3, meaning that different parts of the isotropic sample encode different coherence times, with 0.9 fs steps between different coherence times. Beams 1 and 2 were chopped together at 50 Hz and the signal was collected in the $-k_1 + k_2 + k_3$ phase-matched direction on the slit of an imaging spectrometer (Shamrock, Andor Technologies) and recorded on a CMOS camera (Miro M310, Vision Research). Pulse 4 in the boxcar geometry was attenuated using a neutral-density filter and mixed with the signal on the camera to enable a phase-sensitive

heterodyne detection of the signal field. The delay time between pulse 3 and the pulse 1-2 pair was swept continuously during acquisition using an optomechanical delay line (Aerotech, Inc.). Individual 2DES spectra were recorded at waiting times from -300 fs to +2240 fs with a 0.4 fs spacing. The rephasing pathways were isolated in post-processing by selecting the positive-valued coherence times.

The data were Fourier filtered in the waiting-time domain to remove scattered light, generating a final data set with 10 fs spacing between waiting times[66]. The 2DES data were phased by fitting to separately acquired pump-probe data using a sum-of-squared-error regression. Each experiment was repeated to collect a total of 25 independent measurements that were subsequently averaged after phasing. Beating maps were generated by fitting the exponentially decaying dynamics of the phased, complex-valued data and subtracting the fit. The residuals of the full waiting time and the sliding window spectra were apodized, zero-padded out to 2001 total points, and then Fourier transformed.

5.7 Supporting Material: Analysis of Feynman Pathways and Their Signal Contribution

We believe the pathway proposed in Figure 5.4 of the main text offers the best explanation for the beats we observe in the below-diagonal reducing spectra in reducing conditions. Figure 5.6 shows the possible rephasing Feynman pathways that could contribute to the signal in the 4-1 cross peak region, adapted from Refs. [51] and [50] but with downhill coherence transfer pathways added. The pathways are split into waiting time populations, coherences without transfer, and coherences with transfer. They are color-coded by the sign of their time evolution during the waiting time and further split into ground state bleach (GSB), stimulated emission (SE), and excited state absorption (ESA) components. We adapt a system with two excitonic states and add a vibrational mode to all states that is nearly resonant with the exciton energy gap. We note that the energy level spacing of this

vibrational system is similar in form to one where the near-resonant states are vibronically mixed, as shown at the bottom of Figure 5.6. We only include Feynman pathways in the vibrational picture to minimize redundancy.

A number of conditions must be met for a pathway to explain the beating signals we observe in our rephasing spectra. First, the ket side of the density matrix must be of a higher energy state than the bra side during the waiting time to generate a positive beat frequency. This necessity eliminates the majority of the coherence pathways without coherence transfer (Figure 5.6), leaving only two pathways featuring a $|e_4\rangle\langle e_{1v}|$ waiting time coherence. These pathways have a low beating frequency for the near-resonance condition to be met, so they cannot explain the beating we observe at hundreds of wavenumbers. The second condition that must be met is that the bra-ket energy difference should remain constant during the coherence transfer event. Each complex within the ensemble undergoes energy transfer over a stochastic distribution of waiting times. A change in the bra-ket energy difference would thus diminish the fixed phase relationship that must exist to observe the coherence. The transfer pathways under which the energy difference does not change are marked with a diamond ($\diamond$) symbol. For the third condition, the pathway must remain in the same below-diagonal region of the 2D spectrum for all frequencies we observe in Figure 5.2. In other words, the pathway must hold for vibrational modes ranging over several hundred wavenumbers to explain the large numbers of beating frequencies. The pathways which satisfy this condition are marked with a double dagger ($\ddagger$) symbol. The only pathway that satisfies all three conditions is the pathway proposed in the main text. Here, a vibrational coherence located predominantly on exciton 4 is transferred to a vibrational coherence during exciton 1 during the waiting time. This pathway requires that excitons 4 and 1 are coupled and subsequently delocalized over the same chromophores. Otherwise, the final state in the Feynman pathway would be a coherence state between ground state vibrations on different chromophores.

Due to the enhanced vibronic coupling in reducing conditions, we would expect stronger

ground state vibrational coherence pathways due to increased oscillator strength between vibronic states and vibrationally excited ground state energies, as has been suggested in other studies[18, 15, 46, 47]. We observe this effect in the below-diagonal beating maps in Figure 5.2, where many negative frequencies are stronger in reducing conditions. It is worth noting that the diagonal peaks, illustrated by the left pathway in panel B, show a relatively smaller enhancement of negative beats in reducing conditions, possibly because of the relatively weaker transitions involving $|e_{4v}\rangle$ in the third laser interaction and signal generation. This trend has some exceptions, such as the 125 cm^{-1} beat. Finally, we wish to note that the excitation of only one vibrational mode is shown in each pathway in Figure 5.6, though it is possible that the bra and ket sides could each have excitations along different vibrational coordinates so long as the same ω_τ and ω_t frequencies were roughly maintained.

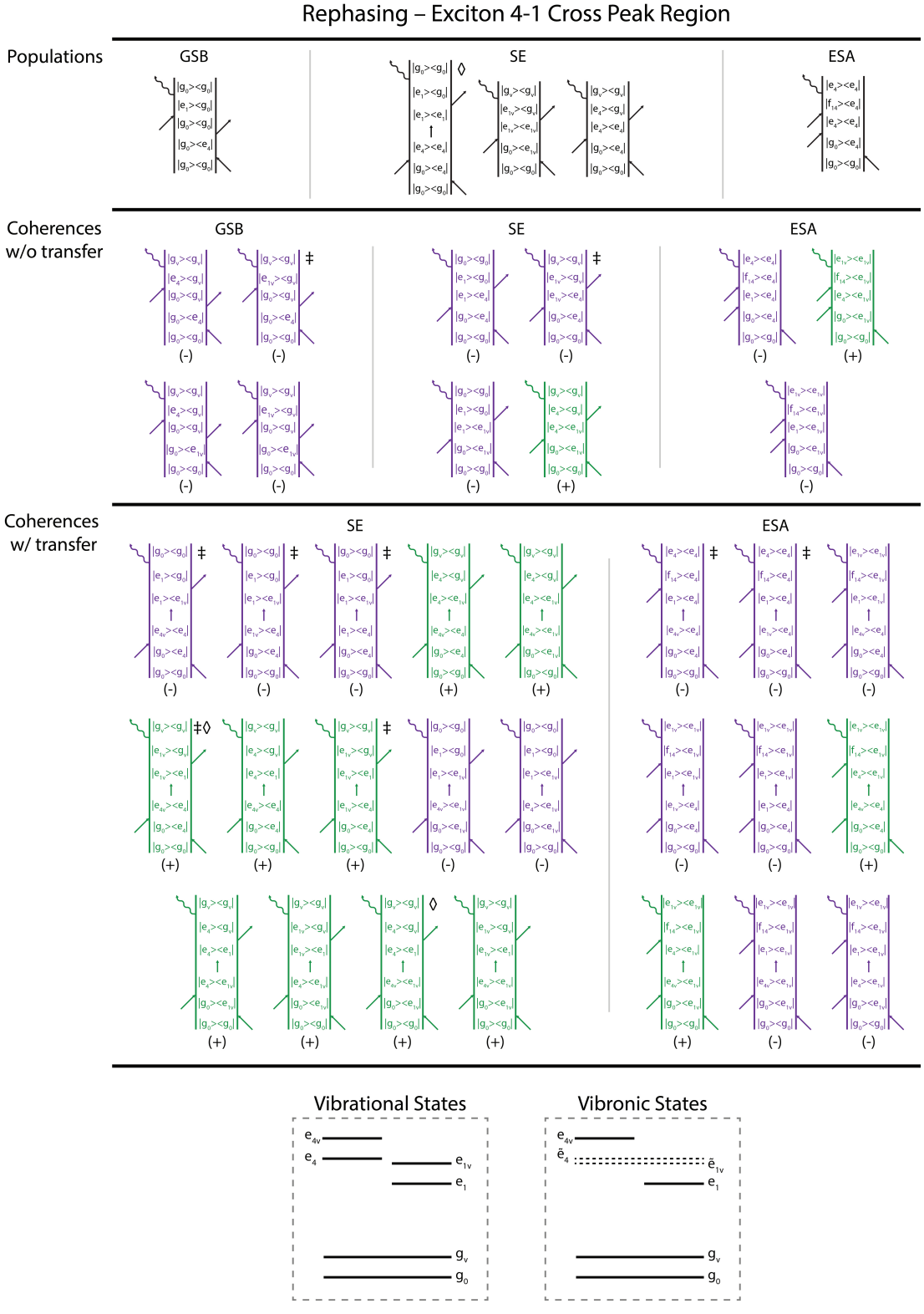

Figure 5.6: (Continued on the following page.)

Figure 5.6: Pathways that could contribute to a below-diagonal rephasing signal in an excitonic picture with near-resonant vibrations. Shown are populations, coherences without waiting time transfer, and coherences with waiting time transfer grouped by their ground state bleach (GSB), stimulated emission (SE), or excited state absorption (ESA) character. Pathways coded in black have no beating sign during the waiting time, while green and purple denote pathways that beat during the waiting time with a positive and negative frequency, respectively. The diamond ($\diamond$) symbol indicates that the bra-ket energy spacing is maintained through energy transfer in the waiting time, and the double dagger ($\ddagger$) symbol indicates that the near-resonance condition need not hold for the pathway to contribute to the exciton 4-1 cross peak region. Only one positive-beating pathway, shown in the main text, holds each condition. The schematic energy level diagram (bottom) shows that purely vibrational systems and systems with vibronically coupled states have similar energy level spacings and thus follow identical Feynman pathway patterns even though the characters of the states change significantly. For brevity, only the purely vibrational Feynman pathways are shown.

REFERENCES

[1] Robert E. Blankenship. *Molecular Mechanisms of Photosynthesis.* Wiley/Blackwell, Chichester, West Sussex, 2nd edition, 2014.

[2] Alexander V. Ruban. Crops on the fast track for light. *Nature*, 541:36, 2017.

[3] Roderick K. Clayton and Betty J. Clayton. B850 pigment-protein complex of rhodopseudomonas sphaeroides: Extinction coefficients, circular dichroism, and the reversible binding of bacteriochlorophyll. *Proceedings of the National Academy of Sciences, USA*, 78(9):5583–5587, 1981.

[4] Zhenfeng Liu, Hanchi Yan, Kebin Wang, Tingyun Kuang, Jiping Zhang, Lulu Gui, Xiaomin An, and Wenrui Chang. Crystal structure of spinach major light-harvesting complex at 2.72 Å resolution. *Nature*, 428(6980):287–292, 2004.

[5] R. E. Fenna and B. W. Matthews. Chlorophyll arrangement in a bacteriochlorophyll protein from chlorobium limicola. *Nature*, 258(5536):573–577, 1975.

[6] Tobias Brixner, Jens Stenger, Harsha M. Vaswani, Minhaeng Cho, Robert E. Blankenship, and Graham R. Fleming. Two-dimensional spectroscopy of electronic couplings in photosynthesis. *Nature*, 434(7033):625–628, 2005.

[7] Jakub Dostál, Jakub Pšenčík, and Donatas Zigmantas. In situ mapping of the energy flow through the entire photosynthetic apparatus. *Nature Chemistry*, 8:705, 2016.

[8] G. S. Engel, T. R. Calhoun, E. L. Read, T. K. Ahn, T. Mancal, Y. C. Cheng, R. E. Blankenship, and G. R. Fleming. Evidence for wavelike energy transfer through quantum coherence in photosynthetic systems. *Nature*, 446(7137):782–6, 2007.

[9] Gregory D. Scholes, Graham R. Fleming, Lin X. Chen, Alán Aspuru-Guzik, Andreas Buchleitner, David F. Coker, Gregory S. Engel, Rienk van Grondelle, Akihito Ishizaki,

David M. Jonas, Jeff S. Lundeen, James K. McCusker, Shaul Mukamel, Jennifer P. Ogilvie, Alexandra Olaya-Castro, Mark A. Ratner, Frank C. Spano, K. Birgitta Whaley, and Xiaoyang Zhu. Using coherence to enhance function in chemical and biophysical systems. *Nature*, 543(7647):647–656, 2017.

[10] Seth Lloyd, Vazrik Chiloyan, Yongjie Hu, Samuel Huberman, Zi-Wen Liu, and Gang Chen. No energy transport without discord. 2015.

[11] Shaul Mukamel. *Principles of Nonlinear Optical Spectroscopy*. Oxford University Press, New York, 1995.

[12] Sergei Savikhin, Daniel R. Buck, and Walter S. Struve. Oscillating anisotropies in a bacteriochlorophyll protein: Evidence for quantum beating between exciton levels. *Chemical Physics*, 223(2):303–312, 1997.

[13] Gitt Panitchayangkoon, Dugan Hayes, Kelly A. Fransted, Justin R. Caram, Elad Harel, Jianzhong Wen, Robert E. Blankenship, and Gregory S. Engel. Long-lived quantum coherence in photosynthetic complexes at physiological temperature. *Proceedings of the National Academy of Sciences*, 107(29):12766–12770, 2010.

[14] E. Collini, C. Y. Wong, K. E. Wilk, P. M. Curmi, P. Brumer, and G. D. Scholes. Coherently wired light-harvesting in photosynthetic marine algae at ambient temperature. *Nature*, 463(7281):644–7, 2010.

[15] Vivek Tiwari, William K. Peters, and David M. Jonas. Electronic resonance with anticorrelated pigment vibrations drives photosynthetic energy transfer outside the adiabatic framework. *Proceedings of the National Academy of Sciences*, 110(4):1203, 2013.

[16] Margherita Maiuri, Evgeny E. Ostroumov, Rafael G. Saer, Robert E. Blankenship, and Gregory D. Scholes. Coherent wavepackets in the fenna–matthews–olson complex are

robust to excitonic-structure perturbations caused by mutagenesis. *Nature Chemistry*, 10:177, 2018.

[17] R. Tempelaar, T. L. Jansen, and J. Knoester. Vibrational beatings conceal evidence of electronic coherence in the fmo light-harvesting complex. *Journal of Physical Chemistry B*, 118(45):12865–72, 2014.

[18] Niklas Christensson, Harald F. Kauffmann, Tõnu Pullerits, and Tomáš Mančal. Origin of long-lived coherences in light-harvesting complexes. *Journal of Physical Chemistry B*, 116(25):7449–7454, 2012.

[19] Erling Thyrhaug, Roel Tempelaar, Marcelo J. P. Alcocer, Karel Žídek, David Bína, Jasper Knoester, Thomas L. C. Jansen, and Donatas Zigmantas. Identification and characterization of diverse coherences in the fenna–matthews–olson complex. *Nature Chemistry*, 10(7):780–786, 2018.

[20] Lili Wang, Marco A. Allodi, and Gregory S. Engel. Quantum coherences reveal excited-state dynamics in biophysical systems. *Nature Reviews Chemistry*, 3(8):477–490, 2019.

[21] S. Irgen-Gioro, K. Gururangan, R. G. Saer, R. E. Blankenship, and E. Harel. Electronic coherence lifetimes of the fenna-matthews-olson complex and light harvesting complex ii. *Chem Sci*, 10(45):10503–10509, 2019.

[22] S. Irgen-Gioro, A. P. Spencer, W. O. Hutson, and E. Harel. Coherences of bacteriochlorophyll a uncovered using 3d-electronic spectroscopy. *J Phys Chem Lett*, 9(20):6077–6081, 2018.

[23] S. Irgen-Gioro, K. Gururangan, A. P. Spencer, and E. Harel. Non-uniform excited state electronic-vibrational coupling of pigment-protein complexes. *J Phys Chem Lett*, pages 10388–10395, 2020.

[24] V. R. Policht, A. Niedringhaus, and J. P. Ogilvie. Characterization of vibrational coherence in monomeric bacteriochlorophyll a by two-dimensional electronic spectroscopy. *J Phys Chem Lett*, 9(22):6631–6637, 2018.

[25] E. A. Arsenault, Y. Yoneda, M. Iwai, K. K. Niyogi, and G. R. Fleming. Vibronic mixing enables ultrafast energy flow in light-harvesting complex ii. *Nat Commun*, 11(1):1460, 2020.

[26] Wenli Zhou, Russell LoBrutto, Su Lin, and Robert E. Blankenship. Redox effects on the bacteriochlorophyll -containing fenna-matthews-olson protein fromchlorobium tepidum. *Photosynthesis Research*, 41(1):89–96, 1994.

[27] Thomas M. Wahlund, Carl R. Woese, Richard W. Castenholz, and Michael T. Madigan. A thermophilic green sulfur bacterium from new zealand hot springs, chlorobium tepidum sp. nov. *Archives of Microbiology*, 156(2):81–90, 1991.

[28] Rafael Saer, Gregory S Orf, Xun Lu, Hao Zhang, Matthew J Cuneo, Dean AA Myles, and Robert E Blankenship. Perturbation of bacteriochlorophyll molecules in fenna–matthews–olson protein complexes through mutagenesis of cysteine residues. *Biochim. Biophys. Acta - Bioenergetics*, 1857(9):1455–1463, 2016.

[29] Jianzhong Wen, Hao Zhang, Michael L. Gross, and Robert E. Blankenship. Membrane orientation of the fmo antenna protein from lt;emgt;chlorobaculum tepidumlt;/emgt; as determined by mass spectrometry-based footprinting. *Proceedings of the National Academy of Sciences*, 106(15):6134, 2009.

[30] Gregory S. Orf, Rafael G. Saer, Dariusz M. Niedzwiedzki, Hao Zhang, Chelsea L. McIntosh, Jason W. Schultz, Liviu M. Mirica, and Robert E. Blankenship. Evidence for a cysteine-mediated mechanism of excitation energy regulation in a photosynthetic an-

tenna complex. *Proceedings of the National Academy of Sciences*, 113(31):E4486–E4493, 2016.

[31] Marco A. Allodi, John P. Otto, Sara H. Sohail, Rafael G. Saer, Ryan E. Wood, Brian S. Rolczynski, Sara C. Massey, Po-Chieh Ting, Robert E. Blankenship, and Gregory S. Engel. Redox conditions affect ultrafast exciton transport in photosynthetic pigment–protein complexes. *The Journal of Physical Chemistry Letters*, 9(1):89–95, 2018.

[32] Jacob S. Higgins, Lawson T. Lloyd, Sara H. Sohail, Marco A. Allodi, John P. Otto, Rafael G. Saer, Ryan E. Wood, Sara C. Massey, Po-Chieh Ting, Robert E. Blankenship, and Gregory S. Engel. Photosynthesis tunes quantum mechanical mixing of electronic and vibrational states to steer exciton energy transfer. *Proceedings of the National Academy of Sciences*, 2021.

[33] A. Kolli, E. J. O'Reilly, G. D. Scholes, and A. Olaya-Castro. The fundamental role of quantized vibrations in coherent light harvesting by cryptophyte algae. *J Chem Phys*, 137(17):174109, 2012.

[34] Edward J. O'Reilly and Alexandra Olaya-Castro. Non-classicality of the molecular vibrations assisting exciton energy transfer at room temperature. *Nature Communications*, 5(1):3012, 2014.

[35] Richard Stones and Alexandra Olaya-Castro. Vibronic coupling as a design principle to optimize photosynthetic energy transfer. *Chem*, 1(6):822–824, 2016.

[36] P. Hamm and M. T. Zanni. *Concepts and methods of 2D Infrared Spectroscopy*. Cambridge UP, 2011.

[37] Robert S. Knox. Electronic excitation transfer in the photosynthetic unit: Reflections on work of william arnold. *Photosynthesis Research*, 48(1):35–39, 1996.

[38] Jan A. Leegwater. Coherent versus incoherent energy transfer and trapping in photosynthetic antenna complexes. *Journal of Physical Chemistry*, 100(34):14403–14409, 1996.

[39] Vytautas Butkus, Leonas Valkunas, and Darius Abramavicius. Vibronic phenomena and exciton–vibrational interference in two-dimensional spectra of molecular aggregates. *Journal of Chemical Physics*, 140(3):034306, 2014.

[40] Vytautas Butkus, Jan Alster, Eglė Bašinskaitė, Ramunas Augulis, Patrik Neuhaus, Leonas Valkunas, Harry L. Anderson, Darius Abramavicius, and Donatas Zigmantas. Discrimination of diverse coherences allows identification of electronic transitions of a molecular nanoring. *Journal of Physical Chemistry Letters*, 8(10):2344–2349, 2017.

[41] Margus Rätsep and Arvi Freiberg. Electron–phonon and vibronic couplings in the fmo bacteriochlorophyll a antenna complex studied by difference fluorescence line narrowing. *Journal of Luminescence*, 127(1):251–259, 2007.

[42] Kelly A. Fransted, Justin R. Caram, Dugan Hayes, and Gregory S. Engel. Two-dimensional electronic spectroscopy of bacteriochlorophyll a in solution: Elucidating the coherence dynamics of the fenna-matthews-olson complex using its chromophore as a control. *The Journal of Chemical Physics*, 137(12):125101, 2012.

[43] Minhaeng Cho, Harsha M. Vaswani, Tobias Brixner, Jens Stenger, and Graham R. Fleming. Exciton analysis in 2d electronic spectroscopy. *The Journal of Physical Chemistry B*, 109(21):10542–10556, 2005.

[44] Margus Rätsep, Zheng-Li Cai, Jeffrey R. Reimers, and Arvi Freiberg. Demonstration and interpretation of significant asymmetry in the low-resolution and high-resolution qy fluorescence and absorption spectra of bacteriochlorophyll a. *Journal of Chemical Physics*, 134(2):024506, 2011.

[45] Matteo Ceccarelli, Marc Lutz, and Massimo Marchi. A density functional normal mode calculation of a bacteriochlorophyll a derivative. *Journal of the American Chemical Society*, 122(14):3532–3533, 2000.

[46] M. B. Plenio, J. Almeida, and S. F. Huelga. Origin of long-lived oscillations in 2d-spectra of a quantum vibronic model: electronic versus vibrational coherence. *J Chem Phys*, 139(23):235102, 2013.

[47] A. Chenu, N. Christensson, H. F. Kauffmann, and T. Mancal. Enhancement of vibronic and ground-state vibrational coherences in 2d spectra of photosynthetic complexes. *Sci Rep*, 3:2029, 2013.

[48] Dugan Hayes and Gregory S Engel. Extracting the excitonic hamiltonian of the fenna-matthews-olson complex using three-dimensional third-order electronic spectroscopy. *Biophysical Journal*, 100(8):2043–2052, 2011.

[49] Stephanie M. Hart, James L. Banal, Mark Bathe, and Gabriela S. Schlau-Cohen. Identification of nonradiative decay pathways in cy3. *The Journal of Physical Chemistry Letters*, 11(13):5000–5007, 2020.

[50] Lili Wang, Graham B. Griffin, Alice Zhang, Feng Zhai, Nicholas E. Williams, Richard F. Jordan, and Gregory S. Engel. Controlling quantum-beating signals in 2d electronic spectra by packing synthetic heterodimers on single-walled carbon nanotubes. *Nature Chemistry*, 9(3):219–225, 2017.

[51] Daniel B. Turner, Rayomond Dinshaw, Kyung-Koo Lee, Michael S. Belsley, Krystyna E. Wilk, Paul M. G. Curmi, and Gregory D. Scholes. Quantitative investigations of quantum coherence for a light-harvesting protein at conditions simulating photosynthesis. *Physical Chemistry Chemical Physics*, 14(14):4857–4874, 2012.

[52] A.; Willow R.; Laible P.; Bocian D.; Kirmaier C; Holten D.; Mančal T.; Ogilvie J. Policht, V.; Niedringhaus. Hidden vibronic and excitonic structure and vibronic coherence transfer in the bacterial reaction center. *arXiv*, 2021.

[53] Alexandra Olaya-Castro, Chiu Fan Lee, Francesca Fassioli Olsen, and Neil F. Johnson. Efficiency of energy transfer in a light-harvesting system under quantum coherence. *Phys. Rev. B*, 78:085115, Aug 2008.

[54] Patrick Rebentrost, Masoud Mohseni, and Alán Aspuru-Guzik. Role of quantum coherence and environmental fluctuations in chromophoric energy transport. *The Journal of Physical Chemistry B*, 113(29):9942–9947, 2009. PMID: 19603843.

[55] Francesca Fassioli, Ahsan Nazir, and Alexandra Olaya-Castro. Quantum state tuning of energy transfer in a correlated environment. *The Journal of Physical Chemistry Letters*, 1(14):2139–2143, 2010.

[56] Alexandra Olaya-Castro and Gregory D. Scholes. Energy transfer from förster–dexter theory to quantum coherent light-harvesting. *International Reviews in Physical Chemistry*, 30(1):49–77, 2011.

[57] Mino Yang and Graham Fleming. Influence of phonons on exciton transfer dynamics: comparison of the redfield, förster, and modified redfield equations. *Chemical Physics*, 275:355–372, 2002.

[58] Peter A. Eckert and Kevin J. Kubarych. Vibrational coherence transfer illuminates dark modes in models of the fefe hydrogenase active site. *The Journal of Chemical Physics*, 151(5):054307, 2019.

[59] Jeffrey R. Reimers, Margus Rätsep, and Arvi Freiberg. Asymmetry in the qy fluorescence and absorption spectra of chlorophyll a pertaining to exciton dynamics. *Frontiers in Chemistry*, 8(1104), 2020.

[60] A. W. Chin, J. Prior, R. Rosenbach, F. Caycedo-Soler, S. F. Huelga, and M. B. Plenio. The role of non-equilibrium vibrational structures in electronic coherence and recoherence in pigment–protein complexes. *Nature Physics*, 9(2):113–118, 2013.

[61] Yi-Fen Li, Wenli Zhou, Robert E Blankenship, and James P Allen. Crystal structure of the bacteriochlorophyll a protein from chlorobium tepidum. *Journal of molecular biology*, 271(3):456–471, 1997.

[62] Paolo D Gerola and John M Olson. A new bacteriochlorophyll a-protein complex associated with chlorosomes of green sulfur bacteria. *Biochim. Biophys. Acta - Bioenergetics*, 848(1):69–76, 1986.

[63] Jianzhong Wen, Hao Zhang, Michael L Gross, and Robert E Blankenship. Native electrospray mass spectrometry reveals the nature and stoichiometry of pigments in the fmo photosynthetic antenna protein. *Biochemistry*, 50(17):3502–3511, 2011.

[64] Elad Harel, Andrew F. Fidler, and Gregory S. Engel. Real-time mapping of electronic structure with single-shot two-dimensional electronic spectroscopy. *Proceedings of the National Academy of Sciences*, 107(38):16444–16447, 2010.

[65] Elad Harel, Andrew F. Fidler, and Gregory S. Engel. Single-shot gradient-assisted photon echo electronic spectroscopy. *The Journal of Physical Chemistry A*, 115(16):3787–3796, 2011.

[66] P. D. Dahlberg, A. F. Fidler, J. R. Caram, P. D. Long, and G. S. Engel. Energy transfer observed in live cells using two-dimensional electronic spectroscopy. *Journal of Physical Chemistry Letters*, 4(21):3636–3640, 2013.

[67] Vadim V. Lozovoy, Igor Pastirk, and Marcos Dantus. Multiphoton intrapulse interference.iv.ultrashort laser pulse spectral phase characterization and compensation. *Optics Letters*, 29(7):775–777, 2004.

CHAPTER 6

PROPOSED DIRECTIONS FOR FUTURE RESEARCH

The work presented here shows that the Fenna-Matthews-Olson complex adapts to changing redox environments by tuning the vibronic structure of its excitons. Green sulfur bacteria is a relatively simple photosynthetic organism, and FMO only eight chromophores. Other pigment-protein complexes have tens to hundreds of pigments[1]. While the pigment density of these complexes causes spectral congestion and convolves the signatures of vibronic couplings, work should be done to study vibronic effects in more complex photobiological systems. In the first half of this chapter, I will discuss preliminary ideas for studying redox dependence in another photosynthetic system and for studying nonadiabatic effects in a different class of photobiological complexes, rhodopsin proteins. In both of these sections, I will focus on how we can use the full information encoded in a two-dimensional spectrum to extract the dynamics. In Chapter 3, I described a new method using Feynman pathways that enabled the research in the rest of this thesis. I will discuss ideas for extending this method in the second half of this chapter. The first part will discuss how the method could extract sub-ensemble information from two-dimensional spectroscopic signals, and the second part will discuss how we can use the combinatorial structure of coherence pathways to understand vibronic states in more complex, spectrally congested photosynthetic complexes.

6.1 Redox-Dependent Dynamics in Other Photosynthetic Complexes

The redox environment plays a pivotal role in both the population and coherence dynamics of the Fenna-Matthews-Olson complex[2]. The ultrafast dynamics are directly linked to the biochemistry of the organism, as green sulfur bacteria has several active genes that protect the organism from oxidative damage[3, 4]. It is not clear whether the biochemical or the

quantum mechanical redox dependence evolved first, or if they evolved simultaneously, but their linkage suggests that redox environments are important for light harvesting in other photosynthetic organisms.

Take, for example, the membrane protein IsiA from cyanobacteria. This protein is produced in iron-deficient environments and aids in energy transfer with photosystem I. It has been suggested that IsiA has a similar cysteine-mediated exciton quenching mechanism as FMO[5]. That is, an excited electron is transferred to a thiyl radical followed by charge recombination, bringing the excitation to the ground state. The crystal structure for IsiA has not yet been published, but a highly homologous protein, CP43, found in spinach has been solved[6]. The protein is shown in Figure 6.1. At the inset, two bacteriochlorophyll molecules are shown, along with two cysteine residues (magenta) and a valine residue (orange). This valine residue is singly substituted by cysteine across multiple IsiA proteins, while the surrounding amino acids are conserved. As a result of this point change, CP43 has different quenching properties as IsiA, which suggests that the cysteine is responsible for quenching excitons in IsiA. Further, it has been shown that the addition of a reducing agent in IsiA prolongs the fluorescence lifetime, as with FMO[5, 2]. These data strongly suggest that cysteine plays a regulatory role in energy transfer in IsiA proteins, which should be further investigated by ultrafast studies.

It would be straightforward to test this hypothesis using the same experimental procedures conducted here and in Ref. [7]. The cysteine residues should have the same redox potentials as those in FMO, so oxidizing conditions can be generated by exposing the complex to open air, and reducing conditions by adding a small concentration of a reducing agent such as sodium dithionite. In a two-dimensional spectrum, one could look to the population dynamics, coherences, and other spectral features such as lineshapes to investigate differences between the two redox conditions. The population dynamics allow for comparison of relative rates of downhill energy transfer between redox conditions. The short and long

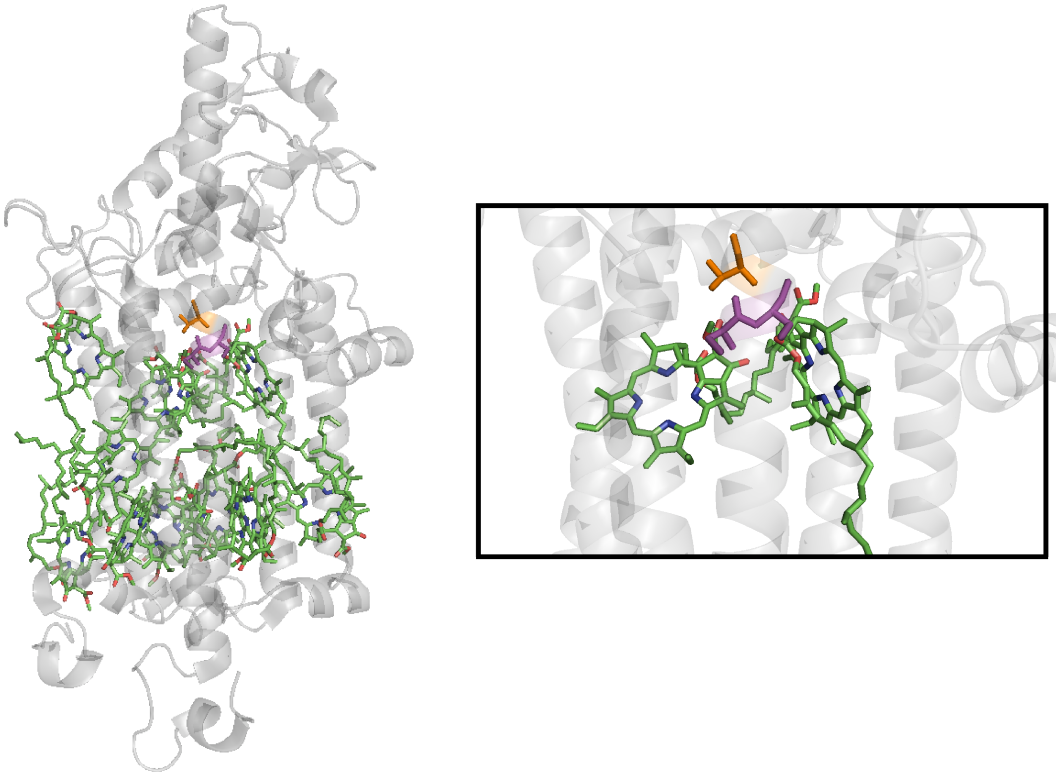

Figure 6.1: Structure of the protein complex CP43 from spinach, which is largely homologous with the complex IsiA from cyanobacteria[6]. Inset: Two bacteriochlorophyll-a pigments neighbor a pair of cysteine residues (magenta) and a valine (orange), which is a point mutation of a cysteine in IsiA. It has been proposed that the cysteines quench excitations in IsiA in a similar manner to FMO, making the IsiA complex an ideal target for redox-dependent effects in other photosynthetic proteins.

time dynamics should reveal competing energy transfer pathways such as cysteine-mediated exciton quenching. Coherences can be used to understand the differences in couplings between redox conditions. The duration of coherences will give insight into the system-bath couplings that underlie energy transfer, as described in Chapter 5. The pattern of coherent beats on the two-dimensional spectrum can help elucidate the vibronic structure, as described in the section below. The beating strengths can be correlated with the population dynamics to relate the changing coupling strengths with the corresponding time dynamics of energy transfer. Time-dependent lineshapes are another feature that can reveal differences in system-bath couplings between the samples[8]. It has been shown that the centerline slope of a diagonal feature is directly proportional to the frequency-frequency correlation function of the exciton[9, 10]. The rate at which the slope decays during the waiting time is intimately related to the dephasing dynamics[11] and the spectral diffusion of an inhomogeneous ensemble. These three observables, populations, coherences, and lineshapes, allow us to fully interrogate how other photosynthetic proteins respond to changes in the redox condition.

6.2 Measuring Nonadiabatic Dynamics in Rhodopsin Proteins

Another family of photobiological complexes, rhodopsin proteins, are known to exhibit excited state electronic-vibrational mixing. There is a wealth of ultrafast literature, mostly transient absorption studies, that studied the dynamics of rhodopsin proteins [12, 13, 14, 15, 16, 17, 18, 19, 20], but to date there are still many questions regarding how the protein environment dictates the outcome of the process. Rhodopsins are transmembrane proteins found in organisms across all of biology, from bacteriorhodopsin in halobacteria to animal rhodopsin in the eyes of animals[21]. They contain one chromophore, retinal, that is covalently bound to a lysine residue inside the protein. The retinal chromophore (see Figure 6.2) has a long conjugated chain of carbon atoms that typically rests in a particular *cis-trans* isomer geometry. Upon photoexcitation, retinal isomerizes to the ground state to a

different stereoisomer. The change in nuclear configuration drives a structural change in the protein, which then activates a biological function. In animal rhodopsin, the photoisomerization initiates a response pathway that is responsible for the phenomenon of vision[22]. In bacteriorhodopsin, a proton is pumped across the cell membrane, which then activates ATP synthase to generate energy for the cell[21]. In both of these cases, rhodopsin has evolved to steer the isomerization dynamics with extreme efficiency. In the solution phase, all-*trans* retinal isomerization occurs on a picosecond timescale, with multiple *cis* photoproducts forming with equal branching ratios (approximately 15% each)[14]. However, in the protein environment, the reaction rate, efficiency, and product specificity are significantly increased. The isomerization in bacteriorhodopsin occurs in 300-500 fs, with the 13-*cis* photoproduct selected for with a 65% efficiency[14]. In animal rhodopsin, the 11-*cis* to all-*trans* isomerization occurs in less than 100 fs[18], with one study claiming that the reaction time is only limited by the vibrational torsional frequency[20]. The protein environment clearly influences the isomerization dynamics, but the exact mechanism has eluded spectroscopists for decades[22]. Two potential mechanisms for this control are 1) steric confinement of the possible product configurations and 2) electrostatic forces to shape the potential energy surfaces and direct the isomerization.

Retinal isomerization is thought to proceed through a conical intersection (CI). Conical intersections are formed in molecules when two adiabatic electronic states become degenerate. This degeneracy depends on two nuclear coordinates defined by the molecule, which span the molecular branching space. It has been speculated that CI's are ubiquitous in molecules[23, 24] and thus have long-ranging impacts on molecular behavior. While they may exist in most molecules, one important question is whether conical intersections are dynamically accessible from the Franck-Condon region of the excited state. Whether the excited state molecule can relax to the nuclear configuration of the conical intersection region is an important factor in understanding the CI's influence on the reactivity.

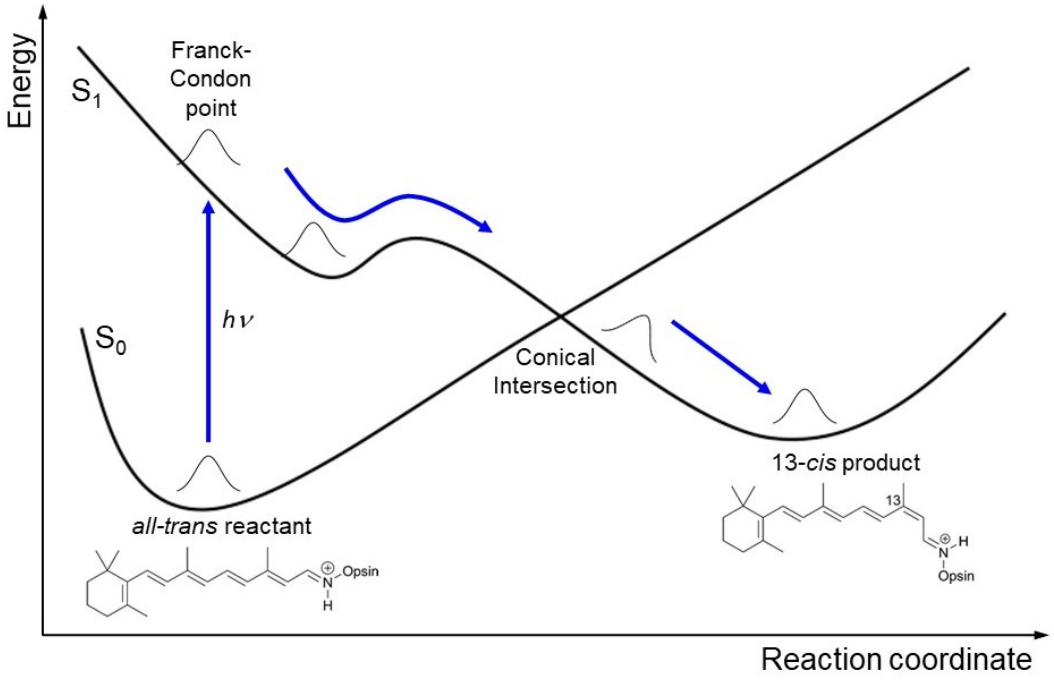

Figure 6.2: Photoisomerization of the retinal chromophore in rhodopsin proteins is thought to proceed through a conical intersection, where the ground and excited electronic states become degenerate. In bacteriorhodopsin, the isomerization occurs from the all-*trans* state to the 13-*cis* configuration[21]. In this reaction, the wavepacket originally in the S_0 reactant well is promoted to the Franck-Condon point on S_1. The nuclear configuration changes as the wavepacket moves along the reaction coordinate. Near the conical intersection, nonadiabatic coupling between the ground and excited electronic surfaces occurs. This coupling determines whether the wavepacket moves to the product well or back to the reactant well. The transitions from the two wells to the excited state surface are resolvable, meaning their dynamics can be studied separately in a two-dimensional spectroscopy experiment.

Near a CI, the Born-Oppenheimer approximation breaks down because nuclear velocity is on the same order as electronic motion and because electronic energy gaps approach rotational/vibrational energy gaps. This breakdown is described by the nonadiabatic coupling vector:

$$h_{ij} = (E_j - E_i)^{-1} \langle \psi_i | \frac{\partial H_{el}}{\partial R} | \psi_j \rangle \tag{6.1}$$

Here, E_i and E_j are the energies of the two adiabatic electronic states, and R is a nuclear coordinate. This term is derived from the molecular Hamiltonian and is typically neglected in a Born-Oppenheimer picture[23, 25]. It is represented here in the basis of adiabatic electronic states. It dictates that two adiabatic states become coupled as they approach degeneracy and/or when the nuclear momentum in the branching space increases. In this sense, nuclear motion can drive nonadiabatic coupling and thus determine whether a reacting wavepacket is sent back to the reactant well or whether it continues along the same path to the product well (or, as described in previous Landau-Zener theories, the wavepacket continues along a diabatic surface[26]).

In rhodopsin proteins, it is generally thought that retinal has a dynamically accessible conical intersection connecting the first excited state with the ground state *cis*- and *trans*-product wells (Figure 6.2)[18, 22]. The conical intersection introduces a third possible mechanism for rhodopsin's control of the isomerization: 3) the role of dynamical coupling. In this case, the wavepacket couples to nuclear motion in the bath to drive both the magnitude and direction of the nuclear momentum. The amino acids in rhodopsin proteins may have evolved so that their vibrational motion could couple to the branching space and nonadiabatically drive the isomerization.

These dynamical couplings have been studied in the nonlinear spectra of rhodopsin proteins. Of particular focus has been the observation of vibrational coherences and how they relate to the isomerization dynamics. Many vibrational coherences in the transient ab-

sorption spectra of animal rhodopsins were observed following the ballistic photoinduced isomerization[19]. These vibrations were thought to dynamically drive the wavepacket isomerization through the conical intersection. Similar observations of vibrational coherence have been made in bacteriorhodopsin[14]. Another study of animal rhodopsin found that the initial phase of the vibrational torsional coordinate largely determined whether the wavepacket trajectory would be reactive or would end back in the reactant well[17]. This study demonstrated that the initial direction of nuclear motion in the Franck-Condon region dictates the branching ratio and hence the nonadiabatic couplings through the conical intersection.

We can extend these studies using two-dimensional electronic spectroscopy because the technique can resolve the excitation axis, which allows access to subensemble dynamics. In an inhomogeneously broadened lineshape such as retinal in bacteriorhodopsin, different excitation energies correspond to different initial geometries in the Franck-Condon region, which may impact the kinetics, couplings, and branching ratios of the reaction. For example, a fluctuating wavepacket that absorbs light when at the left side the reactant well shown in Figure 6.2 will be blue shifted within the lineshape. Though the bath couplings and vibrational phase may be only slightly shifted relative to other states in the ensemble, the studies described above demonstrate that the outcome of the reaction is acutely sensitive to these initial parameters. We can use decay associated spectra[27] and beat maps to observe these differences in the two-dimensional spectra. Decay associated spectra map the kinetic time constants onto the two-dimensional spectrum, simplifying the comparison of reaction rate with different pump and probe energies. Beat maps, which we used in Chapter 5, allow the same mapping but with coherences. The relative strengths and frequencies of coherences within a lineshape should allow us to see both the modes that are activated in the isomerization and their coupling strengths to the system and bath. These data can be correlated with the branching ratios between the all-*trans* and 13-*cis* photoproducts. In

bacteriorhodopsin, the 13-*cis* product is redshifted relative to the all-*trans* reactant, so its formation will correspond to a below-diagonal cross peak in our spectra. We can monitor the kinetics and overall signal strength of this peak alongside the decay of the diagonal peak to serve as a proxy for the relative branching ratios within the ensemble.

6.3 Further Insights into Reactive Steering using Bacteriorhodopsin Mutants

The studies conducted on wild-type bacteriorhodopsin should provide evidence for which couplings drive the isomerization, but mutant studies will give insight into the evolutionary principles that enable this process. This study has been suggested elsewhere[28], but it is briefly expanded here to include experimental implementations and difficulties encountered in recent years. The binding pocket of bacteriorhodopsin is shown in Figure 6.3. Retinal, shown in magenta, is caged by several surrounding amino acid side chains, such as Trp86, Tyr185, and Trp182[29]. They likely constrain the nuclear motion of retinal as it isomerizes. There are several polar amino acids nearby (e.g. Asp85, Asp212, and Thr89) that likely exert electrostatic forces on the chromophore. A few of these residues, such as Asp85, are involved in the proton pumping activity[21]. By mutating a few key residues, one could discern whether steric or electronic effects play a larger role in controlling the isomerization, and how each of these effects interfaces with the dynamical couplings described above. Mutations such as Trp86Ala would reduce the steric hindrance, and mutants like Asp212Val should alter the electric field environment of the binding pocket. Other mutants, such as Tyr185Val, will alter both the steric and electronic effects. The same analysis methods described in the previous section can be used to probe the influence on reaction rate, bath couplings, and branching ratios.

Expressing and isolating mutated bacteriorhodopsin proteins is a fairly involved process and requires its own set of expertise. The wild-type protein is expressed at very high levels in

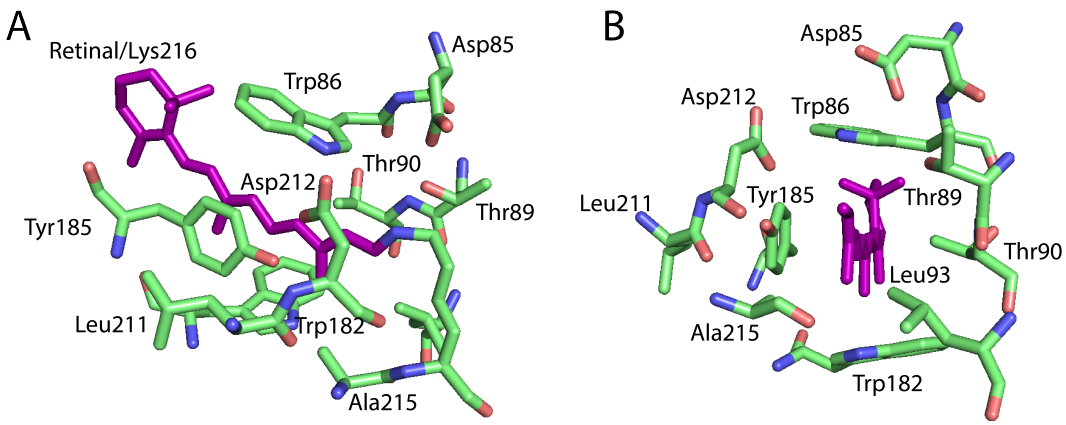

Figure 6.3: Binding pocket of the retinal chromophore in bacteriorhodopsin[29]. Shown are two views (A,B) of the amino acid scaffold. The isomerizing bond is surrounded by several bulky amino acids which may sterically hinder the nuclear motion. There are also multiple polar residues which may alter the electronic structure of the chromophore, which would in turn shape the potential energy surface of the branching space. The covalently bound lysine residue is removed in panel B for clarity.

the native organism *H. salinarum* and can thus be isolated in workable concentrations from a few liters of cell culture. The isolation procedure is well established in the literature[30] and protocols written in our lab. The mutant proteins, however, should be expressed in *E. coli* and isolated via immobilized metal affinity chromatography followed by size exclusion chromatography. Plasmids containing the mutated bacteriorhodopsin gene can be custom ordered from GenScript or other gene synthesis companies and transformed into competent *E. coli* cells. After over inducing the gene expression, the cells are homogenized. This mixture is pushed through a nickel column. The expressed protein is His-tagged, meaning it has six to twelve histidine residues at the C-terminus that adhere strongly to the nickel and can be eluted separately from the rest of the mixture. The protein can be further separated from cellular debris and concentrated using size exclusion chromatography. Future studies should isolate the wild-type protein as a control and several mutated proteins for the experiment. This general procedure is well established for expression and isolation of many different proteins, but it is especially difficult for *E. coli* to express transmembrane proteins. Surprisingly,

this procedure was only fully optimized in 2014 for bacteriorhodopsin. Interested persons should consult the Ph.D. thesis in Ref. [31] and read the detailed procedures for this particular isolation. Other studies have further incorporated bacteriorhodopsin proteins into lipid nanodiscs for ultrafast measurements[15]. This procedure should be consulted as necessary if the signal-to-noise in our ultrafast measurements remains an issue.

6.4 Extension of Double-sided Feynman Pathway Analysis Method

The analysis method described in Chapter 3 and implemented in Chapter 4 was used to isolate the energy transfer time constants in two-dimensional spectra. In this section, I will describe how the method can in principle be extended to study other dynamics such as subsensemble energy transfer and spectral diffusion.

The analysis method extracts the ensemble-averaged rate constants for energy transfer. It would be useful to extend this capability to isolate different time constant distributions across the ensemble. This can in principle be achieved because 2D spectroscopy resolves the excitation axis. Figure 6.4 shows kinetic maps for each of the eight FMO samples studied in Chapter 4, adapted from Ref. [32]. Each map was generated by first convolving the 2D spectrum with a 70 cm^{-1} radius Gaussian window in the ω_1-ω_3 domain. This step blurs adjacent points in the spectrum and effectively averages out slower bath dynamics, as described using circular windows in Chapter 3. The time traces of each point on and below the diagonal were then normalized. Each below diagonal trace was then subtracted from the diagonal trace corresponding to the same excitation energy and then fit to a monoexponential decay. The time constant was plotted onto the original cross peak point, and its saturation was weighted by the goodness of the R-squared fit such that only good fits are saturated. The three markers are plotted to indicate the peak positions of excitons 1, 2, and 4 for each FMO sample.

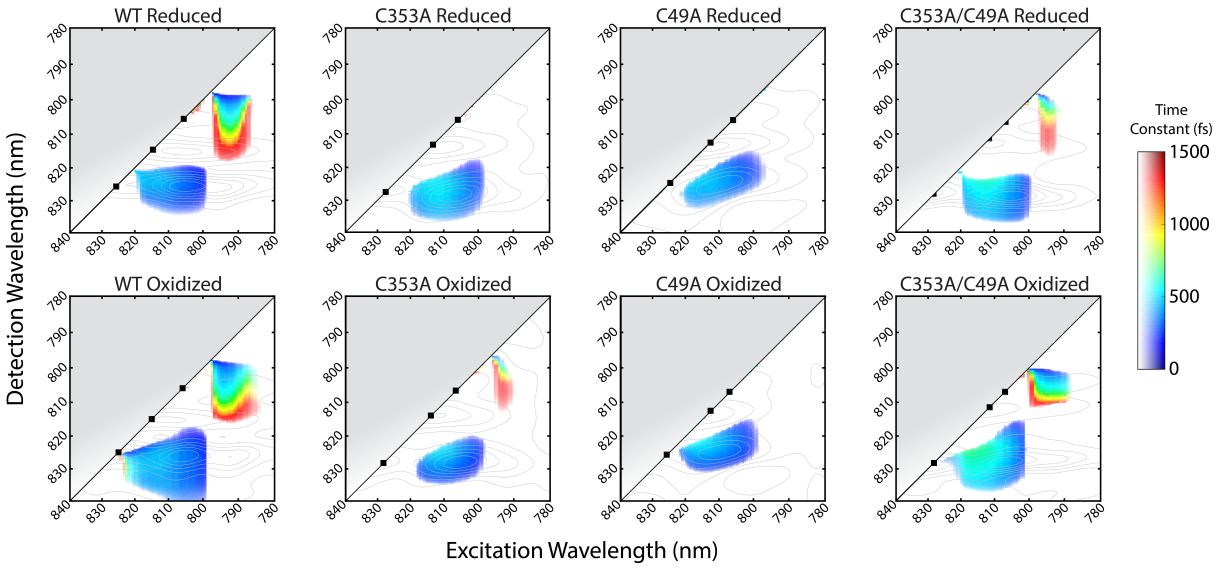

Figure 6.4: Kinetic maps for the wild-type, singly mutated, and doubly mutated FMO spectra under reducing and oxidizing conditions. The 2D spectra are convolved with a 70 cm^{-1} Gaussian window, and each point is normalized and subtracted from its corresponding upper diagonal trace and fit to a monoexponential decay. The time constant, representing the subtracted stimulated emission signals, is plotted on the corresponding cross peak feature. The saturation is weighted by the goodness of fit to the subtracted time constant. Shown as gray contours are the corresponding 2D spectra at t_2=2000 fs. The spectra show inhomogeneity in time constants across spectral features. Figure adapted from Ref. [32] with permission.

As before, the spectral averaging, trace normalization, and subtraction steps remove dynamical contributions to the signal that are unrelated to energy transfer. As such, the time constants plotted on the kinetic map can be used to calculate energy transfer time constants. The values vary across each below diagonal peak, indicating inhomogeneous energy transfer times within the ensemble. The energy transfer times for each peak can in principle be calculated using the same steps shown previously, by numerically simulating the energy transfer and using the constants that best fit the subtracted signal. But care must be taken to ensure that the fitting is carried out properly. For example, there is ambiguity along the detection axis of the kinetic map features because each cross peak trace for a given excitation energy is subtracted from the same diagonal point. Perhaps it would be better to subtract points from the same region of each diagonal and cross peak lineshape. But this assumes that energy transfer occurs between the same regions within two different lineshapes, which is not rigorously true. Perhaps one should average across the detection axis of each lineshape and simply calculate the energy transfer for each excitation energy. This procedure trades the resolution capabilities of 2D spectroscopy but involves less assumptions, and it still allows one to look at statistical distributions of time constants. These steps are unclear and should be developed carefully. Further, sensitivity analyses should be developed to show that steps such as the Gaussian convolution are done without introducing arbitrary errors into the analysis. For example, one could calculate the distribution of energy transfer time constants for several different Gaussian windows. If the distribution is significantly dependent on the window size, then the method should be altered to correct this error.

The time evolution in a 2D spectrum results from the sum of all dynamical subensembles initiated by the laser pulses, including electronic and vibrational motion. We extract the electronic dynamics by first averaging over a region to remove the nuclear dynamics. With the energy transfer dynamics in hand, it may be possible to subsequently obtain information about dynamics such as spectral diffusion. This could be accomplished by mapping out the

nuclear Feynman pathways in more detail than presented in Chapters 3 and 4 and using them along with the known electronic dynamics to simulate the diagonal trace kinetics. Nuclear time constants can be fit to best reproduce the kinetics of segmented regions within a diagonal lineshape. In doing so, we can extract the motion of individual components of the ensemble as they diffuse through the lineshape. These measurements can be compared alongside other metrics like the centerline slope (see above) to glean deeper information about the system-bath dynamics.

6.5 Modeling Vibronic Structure in Pigment-Protein Complexes

The work in this thesis shows that the vibronic structure of FMO plays a central role in regulating energy transfer. In photosynthetic proteins with large numbers of spectrally overlapping pigments, the vibronic structure can difficult to attain. One avenue is beatmap patterns for different waiting time frequencies. Beatmaps allow us to compare the relative strengths of waiting time coherences in different regions of the spectrum. The patterns result from couplings on the ground and excited states and reflect a complex combination of double-sided Feynman pathways that generate a particular beating signal.

We generated beatmaps from room temperature data of light harvesting complex 1 (LH1) from purple bacteria. A population analysis from this data has previously been published[33]. Beatmaps were generated from both rephasing and nonrephasing spectra, each of which has positive and negative waiting time frequencies. Thus, for every frequency, we have four spectral patterns we can use to deduce the underlying vibrational, electronic, or vibronic structure. Several of these maps have cross peak beating patterns that are offset from the diagonal at a frequency different than the beating frequency. Take, for example, the beating patterns at 563 cm^{-1} in Figure 6.5. The lines adjacent to the diagonal indicate the 563 cm^{-1} offset. The positive-valued nonrephasing beat map has a prominent feature offset by approximately 300 cm^{-1} above the diagonal. This discrepancy between frequencies is

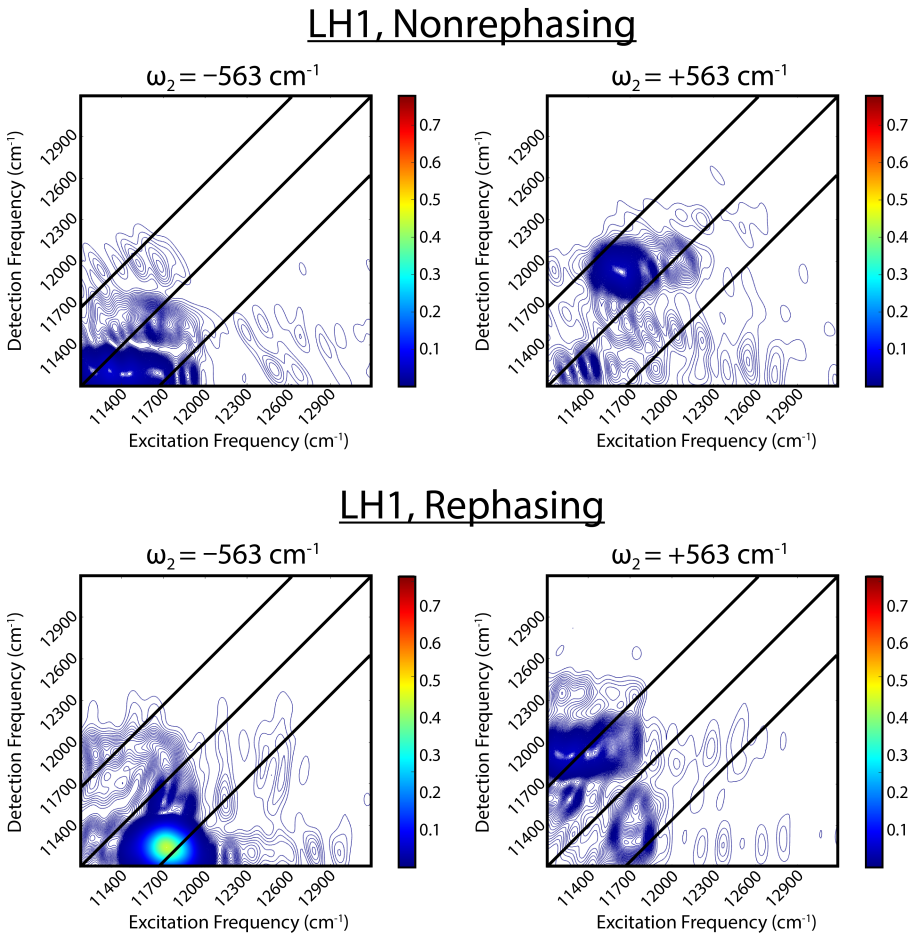

Figure 6.5: Representative beatmaps produced from two-dimensional spectra of light harvesting complex 1 from purple bacteria. The positive and negative beating frequencies of the 563 cm^{-1} oscillation is plotted for the nonrephasing and rephasing spectra. The relative displacement of the patterns with respect to the frequency of the beat is evidence for a complex vibronic structure, as described in the text. We are building a model that aims to reproduce these beating patterns with a vibronic Hamiltonian.

indicative of vibronic coupling in the first excited state manifold[34].

We developed a toy model to elucidate how vibronic couplings could give rise to these odd beating spectra. The model inputs a Hamiltonian containing excitonic energies, vibrational frequencies, and vibronic coupling strengths. The model diagonalizes the Hamiltonian to the vibronic basis and runs through all combinations of Feynman pathways that have a waiting time coherence. The beatmaps of selected frequencies can be plotted according to 1) type of Feynman pathway (stimulated emission, excited state absorption, or ground state bleach), 2) rephasing or nonrephasing spectrum, and 3) positive or negative-valued waiting time frequency. By varying the couplings to reproduce known beatmaps, we can explain the microscopic origins of the observed coherence signals. An undergraduate student, Malachi Elue, has began using the model to account for beating patterns at several different frequencies. For example, the general patterns of two beatmaps shown in Figure 6.6 can be reproduced using a two exciton system with a nearly resonant vibrational mode at 550 cm^{-1} with a Huang-Rhys factor of 0.25. The -299 cm^{-1} rephasing beatmap and relative beating amplitudes are reproduced by stimulated emission Feynman pathways (top). The coherence here is between the two vibronically coupled states. Using the same Hamiltonian, the general square-like beating pattern for the +563 cm^{-1} rephasing map is reproduced with ground state bleach pathways (bottom). While these data are preliminary, they show the vibronic toy model can be used to deduce the precise vibronic structure that may give rise to the observed beating maps.

Several developments should be made so that the toy model can more rigorously extract the vibronic structure of LH1 and other dense arrays of pigments. First, regression and constraints should be added to reproduce all four beat maps for a given waiting time frequency (that is, the rephasing and nonrephasing spectra at positive and negative beating frequencies). For the algorithm, the vibrational frequencies and vibronic coupling strengths could be varied, and the values that best fit to the four beatmaps should be selected. Second, this

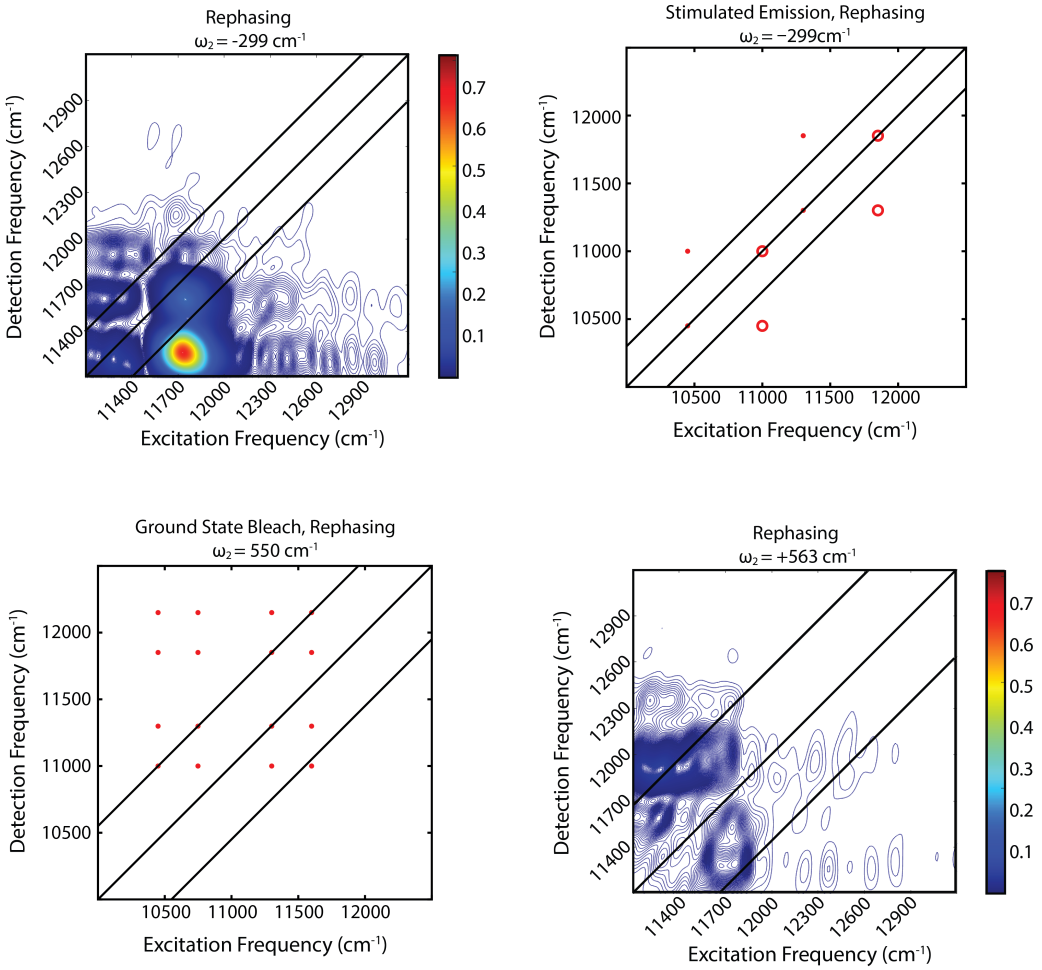

Figure 6.6: A vibronic model is used to reproduce general patterns in beatmaps of LH1. This Hamiltonian uses a two excited state exciton system with a nearly resonant 550 cm^{-1} vibrational mode. The vibronic coupling strength scales with the Huang-Rhys factor, which in this Hamiltonian is 0.25.

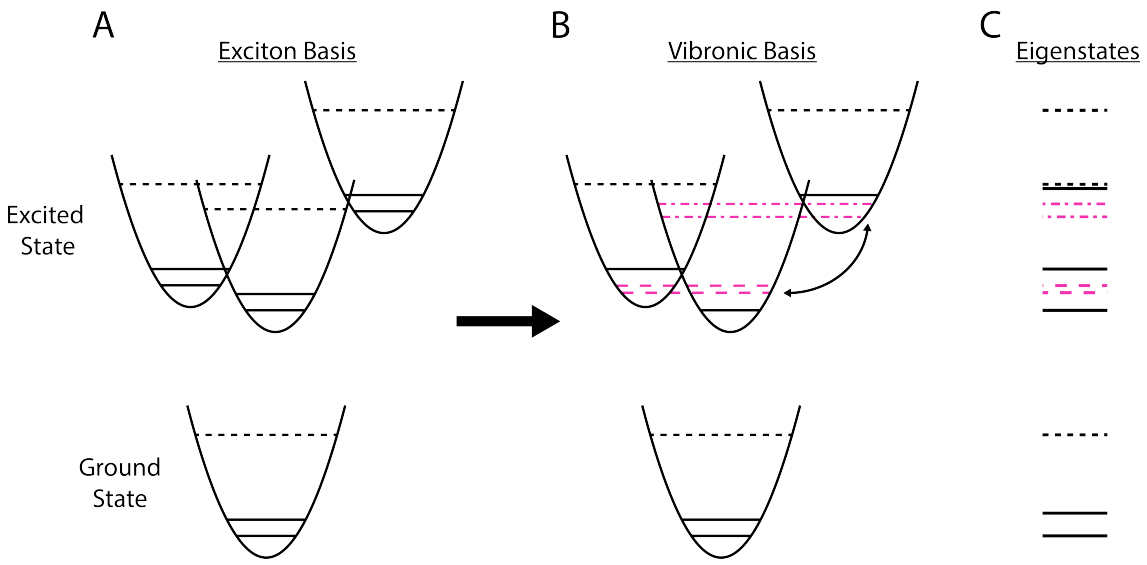

Figure 6.7: Energy levels produced from a system with vibronic coupling to multiple vibrational modes. Shown first is A) the exciton basis, where vibrational modes are resonant with excitonic energy gaps. When allowed to couple, a B) vibronic basis is formed. Two sets of vibronic states are shown in pink. The coherences that generate the beating patterns in Fig. 6.5 could arise from any vibronic state or between the two sets, shown as the double-sided arrow. C) Depending on the energies of the vibrational modes that couple with the excitons, the eigenstates may form different 'bands' in the excited state, giving rise to a new design principle for vibronic steering, described in the text.

model could be integrated with existing stick model calculations to further constrain the electronic energies. The solved Hamiltonian should simultaneously fit the stick spectra and beating maps to obtain accurate coupling parameters. These constraints are necessary to avoid cherry picked solutions and to prevent overfitting the data with too many parameters.

At this point, preliminary evidence in the literature suggests that there are multiple vibrational modes involved in the excited state vibronic structure of these complexes[34, 35]. This phenomenon is depicted in Figure 6.7. The figure shows three excitonic states who each have two vibrational modes added to the Hamiltonian, represented by solid and dashed black lines. The excited vibrational modes can resonantly couple with the ν=0 mode of the other excitons, producing a complex basis of vibronic states, shown in pink. Depending on the energies involved and their coupling strengths, this may result in an eigenbasis with

energetic groupings of different states, shown to the right. This example illustrates a potential design principle for photosynthetic energy transfer: ground state access to different vibronic manifolds. At room temperature, there exists a larger distribution of vibrational modes occupied by the ground state density matrix. The initially occupied mode may have different overlap with these vibronic 'bands,' which may result in different energy transfer dynamics. Thus, the vibronic structure may be crafted to produce a specified branching ratio based on the accessible ground state spectrum. This effect is accessible with our room temperature spectra and may have been obscured in previous 77 K measurements. At this point, this design principle is mostly speculative, as there is only weak evidence for these multi-mode states in LH1 and other complexes. Future studies should validate the possibility of this vibronic structure with the (appropriately constrained) model and link these results with the energy transfer dynamics of the complex.

REFERENCES

[1] Robert E. Blankenship. *Molecular Mechanisms of Photosynthesis*. Wiley/Blackwell, Chichester, West Sussex, 2nd edition, 2014.

[2] Gregory S. Orf, Rafael G. Saer, Dariusz M. Niedzwiedzki, Hao Zhang, Chelsea L. McIntosh, Jason W. Schultz, Liviu M. Mirica, and Robert E. Blankenship. Evidence for a cysteine-mediated mechanism of excitation energy regulation in a photosynthetic antenna complex. *Proceedings of the National Academy of Sciences*, 113(31):E4486–E4493, 2016.

[3] Hui Li, Sara Jubelirer, Amaya M. Garcia Costas, Niels-Ulrik Frigaard, and Donald A. Bryant. Multiple antioxidant proteins protect chlorobaculum tepidum against oxygen and reactive oxygen species. *Archives of Microbiology*, 191(11):853, 2009.

[4] Hui Li, Niels-Ulrik Frigaard, and Donald A. Bryant. [2fe-2s] proteins in chlorosomes: Csmi and csmj participate in light-dependent control of energy transfer in chlorosomes of chlorobaculum tepidum. *Biochemistry*, 52(8):1321–1330, 2013.

[5] Hui-Yuan S. Chen, Michelle Liberton, Himadri B. Pakrasi, and Dariusz M. Niedzwiedzki. Reevaluating the mechanism of excitation energy regulation in iron-starved cyanobacteria. *Biochimica et Biophysica Acta (BBA) - Bioenergetics*, 1858(3):249–258, 2017.

[6] Xuepeng Wei, Xiaodong Su, Peng Cao, Xiuying Liu, Wenrui Chang, Mei Li, Xinzheng Zhang, and Zhenfeng Liu. Structure of spinach photosystem ii–lhcii supercomplex at 3.2Å resolution. *Nature*, 534(7605):69–74, 2016.

[7] Marco A. Allodi, John P. Otto, Sara H. Sohail, Rafael G. Saer, Ryan E. Wood, Brian S. Rolczynski, Sara C. Massey, Po-Chieh Ting, Robert E. Blankenship, and Gregory S. Engel. Redox conditions affect ultrafast exciton transport in photosynthetic

pigment–protein complexes. *The Journal of Physical Chemistry Letters*, 9(1):89–95, 2018.

[8] Sean T. Roberts, Joseph J. Loparo, and Andrei Tokmakoff. Characterization of spectral diffusion from two-dimensional line shapes. *The Journal of Chemical Physics*, 125(8):084502, 2006.

[9] Kyungwon Kwak, Sungnam Park, Ilya J. Finkelstein, and M. D. Fayer. Frequency-frequency correlation functions and apodization in two-dimensional infrared vibrational echo spectroscopy: A new approach. *The Journal of Chemical Physics*, 127(12):124503, 2007.

[10] Emily E. Fenn and M. D. Fayer. Extracting 2d ir frequency-frequency correlation functions from two component systems. *The Journal of Chemical Physics*, 135(7):074502, 2011.

[11] P. Hamm and M. T. Zanni. *Concepts and methods of 2D Infrared Spectroscopy*. Cambridge UP, 2011.

[12] Amir Wand, Itay Gdor, Jingyi Zhu, Mordechai Sheves, and Sanford Ruhman. Shedding new light on retinal protein photochemistry. *Annual Review of Physical Chemistry*, 64(1):437–458, 2013. PMID: 23331307.

[13] Samer Gozem, Philip J. M. Johnson, Alexei Halpin, Hoi Ling Luk, Takefumi Morizumi, Valentyn I. Prokhorenko, Oliver P. Ernst, Massimo Olivucci, and R. J. Dwayne Miller. Excited-state vibronic dynamics of bacteriorhodopsin from two-dimensional electronic photon echo spectroscopy and multiconfigurational quantum chemistry. *The Journal of Physical Chemistry Letters*, 11(10):3889–3896, 2020. PMID: 32330041.

[14] M. Liebel, C. Schnedermann, G. Bassolino, G. Taylor, A. Watts, and P. Kukura. Direct

observation of the coherent nuclear response after the absorption of a photon. *Physical Review Letters*, 112(23):238301, 2014.

[15] Philip J. M. Johnson, Alexei Halpin, Takefumi Morizumi, Leonid S. Brown, Valentyn I. Prokhorenko, Oliver P. Ernst, and R. J. Dwayne Miller. The photocycle and ultrafast vibrational dynamics of bacteriorhodopsin in lipid nanodiscs. *Phys. Chem. Chem. Phys.*, 16:21310–21320, 2014.

[16] Atsushi Yabushita, Takayoshi Kobayashi, and Motoyuki Tsuda. Time-resolved spectroscopy of ultrafast photoisomerization of octopus rhodopsin under photoexcitation. *The Journal of Physical Chemistry B*, 116(6):1920–1926, 2012. PMID: 22251430.

[17] C. Schnedermann, X. Yang, M. Liebel, K. M. Spillane, J. Lugtenburg, I. Fernández, A. Valentini, I. Schapiro, M. Olivucci, P. Kukura, and R. A. Mathies. Evidence for a vibrational phase-dependent isotope effect on the photochemistry of vision. *Nature Chemistry*, 10(4):449–455, 2018.

[18] Dario Polli, Piero Altoè, Oliver Weingart, Katelyn M. Spillane, Cristian Manzoni, Daniele Brida, Gaia Tomasello, Giorgio Orlandi, Philipp Kukura, Richard A. Mathies, Marco Garavelli, and Giulio Cerullo. Conical intersection dynamics of the primary photoisomerization event in vision. *Nature*, 467(7314):440–443, 2010.

[19] P. J. Johnson, A. Halpin, T. Morizumi, V. I. Prokhorenko, O. P. Ernst, and R. J. Miller. Local vibrational coherences drive the primary photochemistry of vision. *Nat Chem*, 7(12):980–6, 2015.

[20] Philip J. M. Johnson, Marwa H. Farag, Alexei Halpin, Takefumi Morizumi, Valentyn I. Prokhorenko, Jasper Knoester, Thomas L. C. Jansen, Oliver P. Ernst, and R. J. Dwayne Miller. The primary photochemistry of vision occurs at the molecular speed limit. *The Journal of Physical Chemistry B*, 121(16):4040–4047, 2017.

[21] Rob Phillips, Jane Kondev, and Julie Theriot. *Physical Biology of the Cell*. Garland Science, Taylor & Francis Group, New York, 2013.

[22] Oliver P. Ernst, David T. Lodowski, Marcus Elstner, Peter Hegemann, Leonid S. Brown, and Hideki Kandori. Microbial and animal rhodopsins: Structures, functions, and molecular mechanisms. *Chemical Reviews*, 114(1):126–163, 2014. PMID: 24364740.

[23] Benjamin G. Levine and Todd J. Martínez. Isomerization through conical intersections. *Annual Review of Physical Chemistry*, 58(1):613–634, 2007.

[24] Markus Kowalewski, Benjamin P. Fingerhut, Konstantin E. Dorfman, Kochise Bennett, and Shaul Mukamel. Simulating coherent multidimensional spectroscopy of nonadiabatic molecular processes: From the infrared to the x-ray regime. *Chemical Reviews*, 117(19):12165–12226, 2017. PMID: 28949133.

[25] João Pedro Malhado, Michael J. Bearpark, and James T. Hynes. Non-adiabatic dynamics close to conical intersections and the surface hopping perspective. *Frontiers in Chemistry*, 2(97), 2014.

[26] Wolfgang Domcke, David R Yarkony, and Horst Köppel. *Conical Intersections: Electronic Structure, Dynamics Spectroscopy*. World Scientific, 1st edition, 2004.

[27] Cheng Wang, Moira L Flanagan, Ryan D McGillicuddy, Haibin Zheng, Alan Ruvim Ginzburg, Xiaojing Yang, Keith Moffat, and Gregory S Engel. Bacteriophytochrome photoisomerization proceeds homogeneously despite heterogeneity in ground state. *Biophysical Journal*, 111(10):2125–2134, 2016.

[28] Moira Lynn Flanagan. *From energy transfer to isomerization: Local protein structure dictates outcome of photobiological excited state dynamics*. Thesis, 2016.

[29] Kazuki Takeda, Yasuhiro Matsui, Nobuo Kamiya, Shin ichi Adachi, Hideo Okumura, and Tsutomu Kouyama. Crystal structure of the m intermediate of bacteriorhodopsin:

Allosteric structural changes mediated by sliding movement of a transmembrane helix. *Journal of Molecular Biology*, 341(4):1023–1037, 2004.

[30] Dieter Oesterhelt and Walther Stoeckenius. [69] isolation of the cell membrane of halobacterium halobium and its fractionation into red and purple membrane. In *Biomembranes Part A*, volume 31 of *Methods in Enzymology*, pages 667–678. Academic Press, 1974.

[31] Dmitry Bratanov. *Expression, purification, and crystallization of bacteriorhodopsin and its derivatives*. Dissertation, Aachen, Techn. Hochsch., Aachen, 2014.

[32] Jacob S. Higgins, Lawson T. Lloyd, Sara H. Sohail, Marco A. Allodi, John P. Otto, Rafael G. Saer, Ryan E. Wood, Sara C. Massey, Po-Chieh Ting, Robert E. Blankenship, and Gregory S. Engel. Photosynthesis tunes quantum mechanical mixing of electronic and vibrational states to steer exciton energy transfer. *Proceedings of the National Academy of Sciences*, 2021.

[33] Peter D. Dahlberg, Po-Chieh Ting, Sara C. Massey, Elizabeth C. Martin, C. Neil Hunter, and Gregory S. Engel. Electronic structure and dynamics of higher-lying excited states in light harvesting complex 1 from rhodobacter sphaeroides. *The Journal of Physical Chemistry A*, 120(24):4124–4130, 2016. PMID: 27232937.

[34] S. Irgen-Gioro, K. Gururangan, A. P. Spencer, and E. Harel. Non-uniform excited state electronic-vibrational coupling of pigment-protein complexes. *J Phys Chem Lett*, pages 10388–10395, 2020.

[35] Po-Chieh Ting. *Excited-State Structures and Dynamics of Light Harvesting Complexes in Photosynthetic Bacteria: How Novel Spectroscopy Unveils Design Principles in Photosynthesis*. Thesis.

CHAPTER 7

CONCLUDING REMARKS: VIBRONIC COUPLING AND EVOLUTION

In summary, I have shown how vibronic states are used for efficient, tunable energy transport in photosynthetic proteins and the role that vibronic coupling plays in conserving coherence in energy transfer. In Chapter 3, I formulated a new analysis method for two-dimensional spectroscopic signals that maps out the dynamical responses of the system using double-sided Feynman pathways. The method leverages symmetries between diagonal and cross peak pathways to isolate signals related to energy transfer, which can be fit to using regression methods. The method works between two limiting cases, when biexciton coupling is weak and when the coupling runs to infinity. In Chapter 4, I used the method to study differences in energy transfer rates between wild-type and cysteine deficient samples of the Fenna-Matthews-Olson complex under oxidizing and reducing conditions. The time constants revealed that energy is steered through a direct, efficient energy transfer pathway in reducing conditions, but is steered through an indirect pathway in oxidizing conditions, where it is more likely to be quenched. Redfield modeling showed that the mechanism responsible for this effect is redox-dependent tuning of the vibronic coupling between excitonic states. Vibronic resonance is maintained in reducing conditions to promote efficient energy transfer and detuned in oxidizing conditions to direct excitations through the quenching pathway. In Chapter 5, I linked this phenomenon with coherent beating signatures observed in FMO. There are many long-lived coherences only present in reducing conditions that are located in cross peak regions associated with downhill energy transfer. These beats were assigned to excited state vibrations that maintain coherence through the energy transfer. This mechanism has many implications for the nature of vibronically-mediated energy transfer. In particular, vibronic energy transfer is a coherent process, and the phase evolution would be maintained regardless of the excitation source. In Chapter 6, I proposed several future

directions that spawn from these studies, including the role of the redox environment in other photosynthetic complexes, nonadiabatic couplings in rhodopsin proteins, extensions of the Feynman analysis method, and a model that can be used to solve the vibronic structure in more convoluted spectra. It is my hope that the work presented here can provide a launchpad for vibronic studies in more complex environments.

In recent years, several experimental studies along with those described here have emerged confirming the importance of resonant vibrations and vibronic states in photosynthetic energy transfer[1, 2]. Additionally, theoretical models have shown how explicitly including resonant vibrations is necessary for directing and enhancing energy transfer in many systems[3, 4]. The mechanism of vibronic energy transfer prompts many microscopic questions that should be investigated in more theoretical detail. For example, the vibronic energy transfer spawns two particles: an exciton and a vibron. It would be worthwhile to understand how they interact and how their dynamics intersect with energy transfer properties. It would also be important to investigate which bath motions cause the energy transfer to be coherent and how bath environments between sites could become correlated. As the field shifts toward a more vibronic picture of photosynthesis, many of the theories that exploded from the initial observation of long-lived coherences[5, 6, 7, 8, 9, 10, 11], which assumed purely electronic coherences, could be recast into this new vibronic framework.

This work is the first to show that biology can actively modulate quantum couplings to protect itself from environmental damage. From the perspective of evolution, nature is agnostic to whether a new adaptation is quantum or classical. It simply uses the capabilities acquired by natural selection to better fit into its environmental niche. That quantum parameters are within reach of these simple bacteria prompts many questions regarding the use of quantum mechanics in other organisms. The vibronic tuning mechanism discovered here is straightforward to achieve. The cysteine residues simply tune the exciton energy gap to fall in and out of resonance with an intrinsic bacteriochlorophyll vibration. The simplicity

of this process coupled with the fact that green sulfur bacteria is a relatively rudimentary photosynthetic organism suggests that the mechanism could exist in other photosynthetic complexes. It is possible that tuning of vibronic and other types of quantum couplings is common across the evolutionary landscape and paired with many different functions in biology.

REFERENCES

[1] E. A. Arsenault, Y. Yoneda, M. Iwai, K. K. Niyogi, and G. R. Fleming. Vibronic mixing enables ultrafast energy flow in light-harvesting complex ii. *Nat Commun*, 11(1):1460, 2020.

[2] A.; Willow R.; Laible P.; Bocian D.; Kirmaier C; Holten D.; Mančal T.; Ogilvie J. Policht, V.; Niedringhaus. Hidden vibronic and excitonic structure and vibronic coherence transfer in the bacterial reaction center. *arXiv*, 2021.

[3] A. Kolli, E. J. O'Reilly, G. D. Scholes, and A. Olaya-Castro. The fundamental role of quantized vibrations in coherent light harvesting by cryptophyte algae. *J Chem Phys*, 137(17):174109, 2012.

[4] Pallavi Bhattacharyya and Graham R. Fleming. The role of resonant nuclear modes in vibrationally assisted energy transport: The lhcii complex. *The Journal of Chemical Physics*, 153(4):044119, 2020.

[5] Patrick Rebentrost, Masoud Mohseni, and Alán Aspuru-Guzik. Role of quantum coherence and environmental fluctuations in chromophoric energy transport. *The Journal of Physical Chemistry B*, 113(29):9942–9947, 2009. PMID: 19603843.

[6] Francesca Fassioli, Ahsan Nazir, and Alexandra Olaya-Castro. Quantum state tuning of energy transfer in a correlated environment. *The Journal of Physical Chemistry Letters*, 1(14):2139–2143, 2010.

[7] Alexandra Olaya-Castro and Gregory D. Scholes. Energy transfer from förster–dexter theory to quantum coherent light-harvesting. *International Reviews in Physical Chemistry*, 30(1):49–77, 2011.

[8] P. Rebentrost and A. Aspuru-Guzik. Communication: Exciton-phonon information flow in the energy transfer process of photosynthetic complexes. *J Chem Phys*, 134(10):101103, 2011.

[9] A. Rivas, S. F. Huelga, and M. B. Plenio. Quantum non-markovianity: characterization, quantification and detection. *Rep Prog Phys*, 77(9):094001, 2014.

[10] F. Caruso, A. W. Chin, A. Datta, S. F. Huelga, and M. B. Plenio. Highly efficient energy excitation transfer in light-harvesting complexes: The fundamental role of noise-assisted transport. *The Journal of Chemical Physics*, 131(10):105106, 2009.

[11] M. Mohseni, A. Shabani, S. Lloyd, and H. Rabitz. Energy-scales convergence for optimal and robust quantum transport in photosynthetic complexes. *The Journal of Chemical Physics*, 140(3):035102, 2014.